HOKKAIDO UNIVERSITY

Title	Multi-stage fatigue analysis of an orthotropic steel bridge deck reinforced with UHPFRC overlay considering crack bridging and interfacial bond stiffness degradations
Author(s)	MA, Chi Hieu
Citation	. ( ) 14880
Issue Date	2022-03-24
DOI	10.14943/doctoral.k14880
Doc URL	http://hdl.handle.net/2115/85327
Type	theses (doctoral)
File Information	Chi_Hieu_MA.pdf

Instructions for use

MULTI-STAGE FATIGUE ANALYSIS OF AN ORTHOTROPIC STEEL BRIDGE DECK REINFORCED WITH UHPFRC OVERLAY CONSIDERING CRACK BRIDGING AND INTERFACIAL BOND STIFFNESS DEGRADATIONS

架橋応力と界面付着の劣化を考慮した UHPFRC 合成直交異方性鋼床版の多段階疲労解析

Chi Hieu Ma

Laboratory of Bridge and Structural Design Engineering

Division of Engineering and Policy for Sustainable Environment

Graduate School of Engineering

Hokkaido University

March 2022

MULTI-STAGE FATIGUE ANALYSIS OF AN ORTHOTROPIC STEEL BRIDGE DECK REINFORCED WITH UHPFRC OVERLAY CONSIDERING CRACK BRIDGING AND INTERFACIAL BOND STIFFNESS DEGRADATIONS

架橋応力と界面付着の劣化を考慮した UHPFRC 合成直交異方性鋼床版の多段階疲労解析

Chi Hieu Ma

A DISSERTATION SUMMITED IN PARTIAL FULFILLMENT

OF THE REQUIREMENT FOR THE DEGREE OF DOCTOR OF PHILOSOPHY

IN ENGINEERING

Examination Committee:

Prof. Takashi MATSUMOTO

Prof. Shunji KANIE

Prof. Takafumi SUGIYAMA

Assoc. Prof. Akira FURUKAWA

Laboratory of Bridge and Structural Design Engineering

Division of Engineering and Policy for Sustainable Environment

Graduate School of Engineering

Hokkaido University

ACKNOWLEDGEMENTS

ABSTRACT

Over the past few decades, orthotropic steel decks (OSDs) have been widely used in long-span bridge structures due to their advantages compared with reinforced concrete bridge decks. However, due to the rapid increase in traffic volumes, premature damages caused by the repetitive loadings at some fatigue sensitive locations of OSDs have been reported in recent years.

On the other hand, with the outstanding properties such as high strengths under both tension and compression as well as a tensile strain-hardening behavior, Ultra-High Performance Fiber Reinforced Concrete (UHPFRC) has been demonstrated to be effective in improving the fatigue durability of OSD structures. Many studies have been conducted to investigate the fatigue performances of OSDs reinforced with UHPFRC overlay, which are primarily based on experimental approach.

However, despite the necessary information about the fatigue performances of composite bridge decks can be assessed by experiments, this experimental approach is still time- and cost- consuming. Moreover, since the comprehensive consideration of fatigue failure mechanisms is insufficient along with the lack of theoretical support from the limited cases of experimental investigations, this approach is not practical for predicting the fatigue performances of existing structures with different geometries and boundary conditions.

Therefore, this leads to the necessity to develop a reliable analytical model that can be rationally and insightfully applied to understand the fatigue behaviors of UHPFRC-OSD composite structure with arbitrary geometries and boundary conditions.

To investigate the beneficial effects of UHPFRC overlay in terms of improving the fatigue durability of OSD, a full-scale UHPFRC-steel composite bridge deck was experimentally tested in Civil Engineering Research Institute (CERI) for Cold Region, Hokkaido, under multi-stages of moving loadings (i.e., with rubber tire wheel or steel wheel) and environmental (i.e., dry or surface water) conditions. Especially, the fatigue behaviors of the composite bridge deck were then evaluated for the stage in which high mechanical wheel loading combined with severe environmental condition (i.e., surface water) were considered, since this case has been demonstrated to reduce the structural performances and the service life of the bridge decks from previous studies.

In this thesis, a numerical model developed with a finite element method was proposed to predict the fatigue performances of an orthotropic steel bridge deck (OSD) strengthened with UHPFRC overlay under multi-stages of wheel loadings and environmental conditions which accorded to the stages from the above fatigue test. The analytical results were then validated using the experimental data.

In stage 1, the composite bridge deck subjected to a moving wheel loading with rubber tire under dry condition was investigated in the fatigue analysis. The 100-year equivalent design traffic load was applied to evaluate the strengthening effect of UHPFRC overlay in fatigue durability enhancement on the OSD. For the analysis in this stage, the primary degradation mechanisms, i.e., the fatigue degradation of bridging stress in cracked UHPFRC caused by local transverse bending and the deterioration in the bond stiffness at UHPFRC/steel interface, were considered and examined in the analytical model. It was found that the effect of the latter deterioration from interface, which was often neglected from the previous analytical studies, on steel stain results was predominant in comparison to that of the former degradation in cracked UHPFRC. In this stage, the current analytical model can provide an acceptable agreement with the strain range results in steel deck plate by the experiment, validating the reliability of the proposed method.

In stage 2, the composite deck was tested under surface water condition to examine the negative impact of stagnant water on the fatigue behaviors of the UHPFRC overlay. Two phases of the material model considering the self-healing behavior and the more severe bridging stress degradation for cracked UHPFRC were assumed in the analysis. In phase 1, under the only environmental condition of surface water, the mechanical recoveries in term of reloading stiffness and tensile strength caused by the autogenous self-healing behavior were applied to the material model of cracked UHPFRC. Thereafter, in phase 2 under the combined action of moving wheel loading and surface water conditions, the more severe bridging stress degradation of cracked UHPFRC were considered by applying its higher speed with the presence of water. It was found that the analytical strain range results of steel deck plate exhibited an acceptable agreement in tendency in comparison to those from the experiment. Therefore, it can be stated that the considered scenarios for UHPFRC cracks mentioned as two phases could have happened in stage 2 of the experiment.

In stage 3, the fatigue analysis of the UHPFRC-steel composite bridge deck was carried out under a furthermore severe condition of mechanical loading, i.e., a moving steel wheel load which was equivalent to 118-year design traffic load. Fatigue damage of the composite deck in this stage was primarily caused by the propagation of UHPFRC cracks and the continuous degradation at the UHPFRC/steel interface. It was found that the speed of bridging stress degradation in cracked UHPFRC, which is dependent on the maximum tensile strain level, was considerably accelerated in this stage, leading to the significant development of cracked regions in UHPFRC overlay. For UHPFRC/steel interface, the gradual expansions in both transverse and longitudinal directions of the debonded area were assumed to govern the fatigue deterioration of the interfacial bond layer in the analysis. It was indicated that, by considering different speeds of expansion from interfacial delamination area, the strain range results in steel deck plate obtained from the analytical model in this stage also acceptably agreed with those from the experiment. At the end of this stage, the fatigue crack was not found in the steel deck plate from the fatigue test. UHPFRC overlay, therefore, still maintained the high fatigue resistance of the composite deck even when a part of the overlay delaminated from the OSD.

In this study, the fatigue degradation in bond stiffness at the UHPFRC/steel interface was comprehensively investigated through the assumed scenarios for each considered stage. It is known that this kind of deterioration which may always occur right under the wheel loading contact region had a dominant effect on the strain evolution results in steel deck plate compared to bridging stress degradation of UHPFRC cracks, owing to the high fatigue durability of UHPFRC material. However, the interfacial deterioration caused by fatigue moving loadings is often neglected from the previous studies of OSD structure. This may lead to the unexpected shorten of fatigue lifetime estimated from the design of UHPFRC-steel composite deck, caused by the inaccurate prediction of stress (strain) ranges at the critical locations in the steel members of OSD. Generally, the understandings about the interfacial bond stiffness degradation which was revealed from the analysis have not been clearly indicated by only experimental measurement and observations at limited locations, that not only demonstrated the advantage of the current analytical model, but also provided a reference for the future investigations of the OSD reinforced with UHPFRC overlay under moving wheel loadings.

TABLE OF CONTENTS

LIST OF TABLES

LIST OF FIGURES

xiii

CHAPTER 1 INTRODUCTION

1.1 Background and motivation

Over the past few decades, the using of the orthotropic steel decks (OSDs) becomes more popular in many long-span bridge structures due to their outstanding features such as light weight, high load capacities and convenience in construction process. However, owing to the relatively small thickness of the deck plates from the early state design and the rapid increase in traffic volumes, the orthotropic steel deck structures under repetitive loading have been suffering the premature damage at the high-stress locations, i.e., fatigue cracks formed and developed at the welded connection joints or edge of cut-out details [1-3]. This kind of deterioration may significantly reduce the structural performance and shorten the expected service life of the steel bridge decks. Therefore, the need to develop the rehabilitation methods that can effectively extend the fatigue durability of the existing bridges using OSD structure as well as ensure the cost-effectiveness is essential nowadays.

One promising technique that is appropriate for both the new and existing bridges, is to overlay the reinforced high-performance materials, i.e., Steel Fiber Reinforced Concrete (SFRC), Engineered Cementitious Composites (ECC) and Ultra-High Performance Concrete (UHPC) on top surface of OSDs to improve the fatigue-resistance capability of these structures [4-6]. It has been demonstrated that the stiffnesses of steel bridge decks are enhanced via the significantly reduction in fatigue stress ranges at the critical locations, and thus the fatigue life of the deteriorated OSDs can be extended.

Ultra-high Performance Fiber Reinforced Concrete (UHPFRC), a recently developed cementitious composite, has also been found to exhibit excellent performance as an overlaid strengthening layer on steel bridge decks [7-10]. Owing to the outstanding properties such as high strengths under both tension and compression as well as a strain-hardening behavior [11], the UHPFRC overlay can effectively reduce the fatigue stress levels by improving the overall stiffness of the OSD even with a 25 mm of small thickness [9,12]. Moreover, a highly dense matrix of UHPFRC provides the material an extremely low permeability, which means the UHPFRC overlay can work as a corrosion protection

Figure 1.1 Fatigue test of full-scale OSD reinforced with UHPFRC overlay [9]

layer to the severe environmental factors, e.g., water and chloride ion [13]. For those reasons, UHPFRC is trustworthy to be used as the strengthening and rehabilitation material for the OSD structure.

Although many studies have reported the fatigue behaviors of the OSD structure strengthened by UHPFRC overlay through the experimental investigations, this approach, however, is time and cost- consuming. Moreover, since the comprehensive consideration of fatigue failure mechanisms is insufficient along with the lack of theoretical support from the limited cases of experimental investigations, this approach is not practical for predicting the fatigue performances of existing structures with different geometries and boundary conditions. Therefore, it is necessary to develop a reliably analytical procedure that can be rationally and insightfully applied to understand the fatigue performances of the UHPFRC-OSD composite structure with the arbitrarily geometric and boundary conditions.

1.2 Brief review of previous studies

To construct a reliable fatigue model of the composite deck, it is significant to refer to the widely recognized methods of reproducing the fatigue mechanisms of the components of the composite structures, e.g., the UHPFRC reinforced overlay and the steel/UHPFRC interface.

In terms of the fatigue of cement-based materials, a vast number of studies about the fatigue characteristics of the normal concrete and fiber reinforced concrete have revealed that the primary cause of the fatigue crack propagation in the materials is a bridging stress degradation under repetitive loading [14-19]. For ECC material under tensile fatigue, the bridging stress degradation characterized by a reduction of the stress transferred between crack surfaces is mainly attributed to the deteriorations such as fiber fatigue rupture and gradual fiber pullout due to interfacial decay [19]. Similar observations were also reported for UHPFRC specimens under repetitive tensile load [11]. Applying the bridging stress degradation concept, the fatigue responses from the RC and fiber reinforced concrete structures were successfully reproduced in the analytical models [20-23]. Particularly, the composite structure of OSD and ECC reinforced overlay under moving wheel load has been already examined in an FE analysis applying the above concept in [20]. From this study, the fatigue behaviors of the structure were well predicted by the analytical tool, which demonstrates the applicability of the bridging stress degradation concept in the numerical investigation of steel bridge deck strengthened with UHPFRC.

As for the bonding technique at the interface between the OSD and the overlaid reinforcement, the method with the shear studs welded on the top surface of steel plate has been used in many researches [6, 7]. However, the welded studs may produce more fatigue susceptible details in the composite structure. One possible method without using the welding connections is gluing the reinforced overlay to the OSD by only the epoxy resin adhesive [9, 24]. As a common technique used to adhere the reinforced overlay to the steel deck, the performance of the epoxy-based bond layer used in OSD with surfacing concrete are typically evaluated by the static tests specified by the standard design, e.g., the direct pull-off test or static flexural test of composite specimens. For the bond technique used in the UHPFRC-steel composite deck in [9], a static 3-point bending test of a small-scale UHPFRC-steel plate has been carried out to determine the failure mode of composite specimen under bending, as reported by Mi [25]. It is found that the UHPFRC layer failed under tensile cracking at the midspan of specimen, followed by the yielding of steel plate without the debonding of the adhesive layer. This demonstrates the high performance of the developed bond technique under static loading. Nevertheless, the repetition of interfacial shear stress at the vicinity of wheel moving load may cause the

fatigue bond failure between the thin thickness concrete surface and steel deck plate. From previous studies [26-28], under a repetitive cyclic loading, the progressive degradation of the interfacial bond stiffness along with the increase in the bond slip displacement has been reported from the shear bond tests of the FRP-concrete lap joint specimens. It was indicated that the interfacial bond stiffness degradation is dependent on the bond stress range-to-failure stress ratio and the number of load cycles. However, this kind of fatigue degradation is often neglected from the analysis of previous studies of OSD structure.

1.3 Objectives and scopes of study

This study presents a numerical model developed in a finite element method to simulate the fatigue behaviors of an orthotropic steel bridge deck (OSD) strengthened with UHPFRC overlay under the multi-stages of moving loading (i.e., with rubber tire or steel wheel) and environmental (i.e., surface water) conditions. The proposed analytical model will be validated with the experimental data of the full-scale UHPFRC-steel composite bridge deck tested in Civil Engineering Research Institute (CERI) for Cold Region [9].

The fatigue degradations in bridging stress of cracked UHPFRC in both dry and surface water conditions, and the deterioration in the bond stiffness at UHPFRC/steel interface are considered as the primary degradation mechanisms in the proposed analytical model of the composite bridge deck under the wheel moving loadings. Based on the experimental observations, the fatigue degradation scenarios corresponding to each stage of the fatigue test are assumed in the analysis. The structural performances of the composite bridge deck for each assumed degradation scenario from each stage are then examined and assessed numerically.

Moreover, the self-healing behavior of cracked UHPFRC in terms of mechanical recoveries is also considered in the fatigue analysis of the stage under surface water condition.

1.4 Organization of the thesis

This thesis is organized into seven chapters. The specific objectives of each chapter are as follows:

Chapter 1 provides the general introduction of the research background, motivation, literature review, objectives and scopes of the study.

Chapter 2 presents the description of the numerical model used for fatigue analysis. The material models for steel and UHPFRC materials used in this study are interpreted in this chapter. The bridging stress degradation relations of cracked UHPFRC under both dry and surface water conditions are introduced in the analytical model. Fatigue degradation model of the UHPFRC/steel interface applied in the analysis are presented. The self-healing behavior of cracked UHPFRC under surface water condition is considered and introduced in this chapter as well.

In **Chapter 3**, a non-linear 3D FEM model is performed to investigate the static behaviors of the UHPFRC-steel composite bridge deck under a wheel loading with rubber tire. The appropriate model which can ensure the accurate estimation as well as the computational-cost saving is chosen in this analysis, that is employed in the next chapters for fatigue investigations of the composite bridge deck under moving wheel loadings.

Chapter 4 presents the fatigue analysis of the composite bridge deck subjected to a moving wheel loading with rubber tire under dry condition (stage 1). The effects of the interfacial bond stiffness degradation and the bridging stress degradation of cracked UHPFRC on the fatigue behaviors of the composite bridge deck are focused on. The scenarios for fatigue degradations at UHPFRC/steel interface are assumed in the fatigue analysis of this stage. The obtained results are discussed and compared with those from experiment.

In the following stage, the current composite deck was subsequently tested under surface water condition (stage 2). In **Chapter 5**, the fatigue analysis of the composite bridge deck under this condition is carried out. Two phases of the material model considering self-healing behavior and reduction of fatigue life for cracked UHPFRC are assumed in the analysis for the second stage of fatigue analysis. The assumed scenarios for the material model of cracked UHPFRC are then assessed by examining the strain

behaviors in steel deck plate and UHPFRC crack propagation throughout the analysis of stage 2.

Chapter 6 presents the fatigue analysis of the composite bridge deck from the final stage (stage 3) is conducted, in which the loading condition is switched from the rubber tire wheel to steel wheel with higher loading levels. Two sub-stages corresponding to the applied wheel load levels are considered in this stage. The fatigue behaviors from each sub-stage are then investigated numerically by the analytical model.

In **Chapter 7**, conclusions of all chapters and recommendations for further studies are shown.

CHAPTER 2   MATERIAL MODEL FOR FATIGUE ANALYSIS OF THE UHPFRC-STEEL COMPOSITE BRIDGE DECK

2.1 Introduction

In this chapter, the description of the proposed numerical model is presented. The material models for steel and UHPFRC materials used in this study are interpreted. The bridging stress degradation relations of cracked UHPFRC under both dry and surface water conditions were applied in the analytical model to reproduce the fatigue deteriorations caused by moving wheel loadings. The cracking behaviors of UHPFRC based on the multi-fixed smeared crack model [29], the self-healing behavior of cracked UHPFRC under surface water condition, and the fatigue degradation model of the UHPFRC/steel interface which is often neglected from the analysis of previous studies of OSD structure are presented in this chapter as well.

2.2 Steel material

The constitutive law of steel is represented by a bilinear isotropic hardening material as shown in Figure 2.1. The yield criterion in the model is following to von Mises criterion. The Poisson's ratio and Young's modulus, E_s, are chosen as 0.3 and 200 GPa, respectively, in this study.
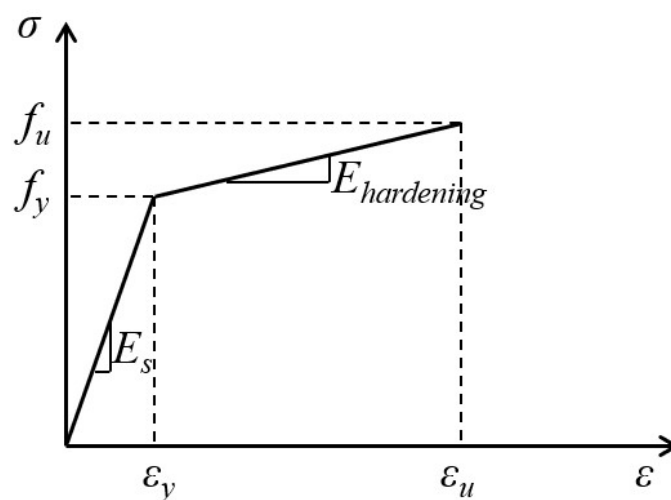
Figure 2.1 Stress-strain relation of steel material

Normally, for a steel structure like OSD, it is designed to ensure that the stress under vehicles is under the fatigue endurance rate, which means that the fatigue life is infinite. For the current experiment of the composite deck, as calculated by Mi [25], the fatigue lives at the critical locations in the steel members are much longer (i.e., nearly double at the critical hotspot) than the design fatigue lifetime of the steel bridge deck (100 years). Besides, no fatigue cracks of steel components were observed in the fatigue experiment of the orthotropic steel deck reinforced by UHPFRC overlay. Therefore, the fatigue of steel members in the composite deck is considered as an insignificant factor and not included in the current analysis.

2.3 UHPFRC material

The constitutive relations and cracking behaviors of UHPFRC are defined in a material user subroutine coded using programming language FORTRAN.

2.3.1 Nonlinear constitutive laws for UHPFRC

Following the Recommendations for Design and Construction of High-Performance Fiber Reinforced Cement Composites with Multiple Fine Cracks (HPFRCC) [30], the uniaxial stress-strain law of UHPFRC under both compression and tension are chosen as shown in Figure 2.2. The total strain of a cracked body of UHPFRC is decomposed into the cracked and non-cracked components. For the non-cracked component of UHPFRC, a linear elastic isotropic relation is defined as represented in Figure 2.2(a) and expressed by

$$\sigma(\varepsilon) = E_u \varepsilon \qquad (\varepsilon \le \varepsilon_{cr}) \tag{2.1}$$

where E_u is Young's modulus, ε_{cr} is the tensile cracking strain of UHPFRC.

As illustrated in Figure 2.2(b), the constitutive law of the cracked component is defined by a bilinear relationship under tension including the strain hardening and strain softening domains. The stress-strain law for cracked component under compression is presented by a parabolic relationship. After reaching the compressive strength point, a linear relation,

i.e., strain softening domain, is applied for the cracked component of UHPFRC under compression.
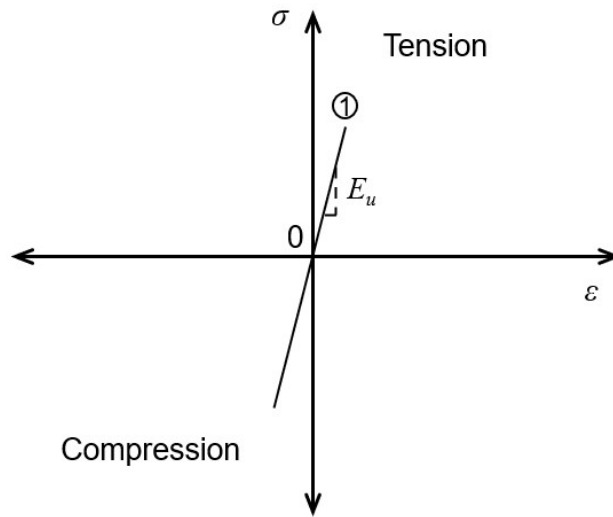
(a) Non-cracked component
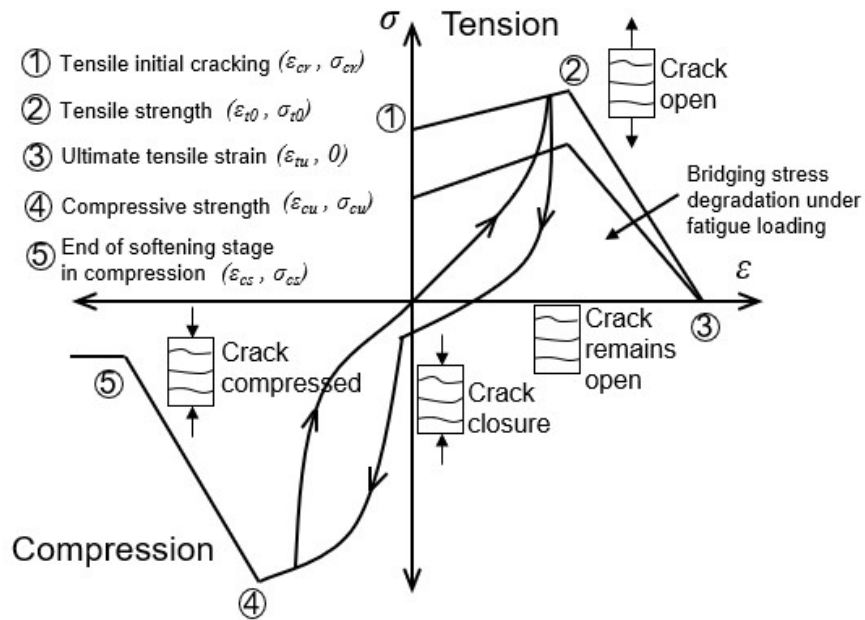
(b) Cracked component

Figure 2.2 Stress-strain relation of UHPFRC material: (a) non-cracked component and (b) cracked component

The expressions of the tensile stress-strain relationship of UHPFRC are as follows

$$\sigma_{ten}(\varepsilon) = \begin{cases} \sigma_{t0} + (\sigma_{t0} - \sigma_{cr})\left(\dfrac{\varepsilon - \varepsilon_{cr}}{\varepsilon_{t0} - \varepsilon_{cr}}\right) & (\varepsilon_{cr} < \varepsilon \le \varepsilon_{t0}) \qquad (2.2) \\[4mm] \sigma_{t0}\left(\dfrac{\varepsilon - \varepsilon_{tu}}{\varepsilon_{t0} - \varepsilon_{tu}}\right) & (\varepsilon_{t0} < \varepsilon \le \varepsilon_{tu}) \qquad (2.3) \end{cases}$$

where σ_{cr} and σ_{t0} represent the cracking stress and peak tensile stress of UHPFRC, respectively; ε_{cr} and ε_{t0} are the strains corresponding to σ_{cr} and σ_{t0}, respectively; and ε_{tu} is the ultimate tensile strain.

The compressive stress-strain relationship of UHPFRC is represented by

$$\sigma_{com}(\varepsilon) = \begin{cases} \sigma_{cu}\dfrac{\varepsilon}{\varepsilon_{cu}}\left(2 - \dfrac{\varepsilon}{\varepsilon_{cu}}\right) & (0 \ge \varepsilon \ge \varepsilon_{cu}) \qquad (2.4) \\[4mm] \sigma_{cu} + 1.6\sigma_{cu}\left(\dfrac{\varepsilon - \varepsilon_{cu}}{\varepsilon_{cu}}\right) & (\varepsilon_{cu} > \varepsilon \ge 1.5\varepsilon_{cu}) \qquad (2.5) \\[4mm] 0.2\sigma_{cu} & (\varepsilon < 1.5\varepsilon_{cu}) \qquad (2.6) \end{cases}$$

in which ε_{cr} is the compressive strain at peak stress σ_{cu}.

2.3.2 Unloading behaviors of cracked UHPFRC

Due to the resistance of the pulled-out fibers that are pushed back into the matrix or buckled between crack surfaces as showed in Figure 2.3, the totally crack closure cannot be attained at the zero-stress level referring to the observation of cracks under tensile unloading in fiber composite specimens [32]. Therefore, the unloading behavior for the stress-strain of the cracked component is further defined in the user material subroutine, as shown in Figure 2.2(b).

In current study, the tensile residual strain ε_{r0} of the hysteresis curve at the peak stress σ_{t0} is chosen as half of the strain at tensile strength point, ε_{t0}, as reported in the experimental investigation of UHPFRC with straight steel fibers [33] (see Figure 2.4)

$$\varepsilon_{r0} = 0.5\varepsilon_{t0} \qquad (2.7)$$
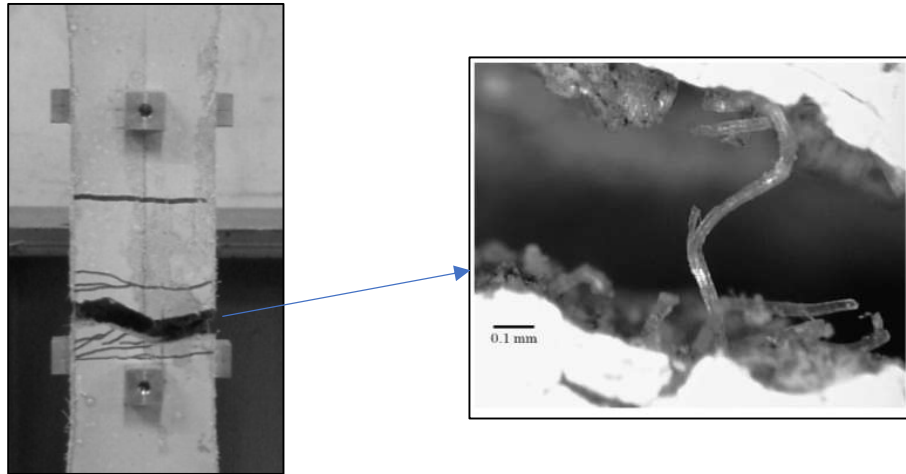
Figure 2.3 Buckling of a fiber between the crack surfaces [32]
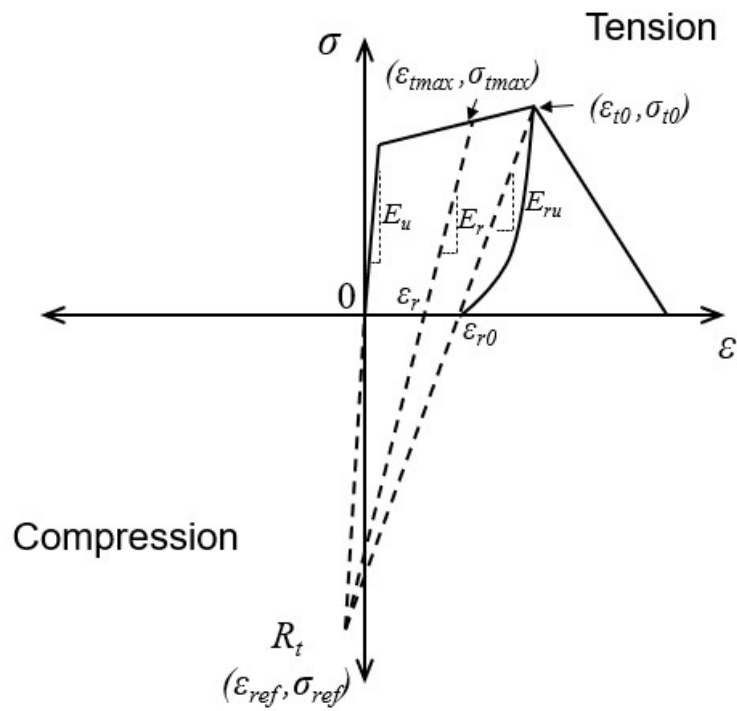
Figure 2.4 Stress-strain relation of UHPFRC under tensile unloading

Subsequently, the method proposed by Yassin [34] using the reference point R_t is used to represent the progressive gap closure of UHPFRC crack under tensile unloading. With the using of the reference point, for the continuous increase in the maximum tensile strain after initial cracking, the degradations of unloading and reloading stiffnesses as well as

the plasticity accumulation are taken into account in the analysis. As shown in Figure 2.4, the reference point R_t is determined by the intersection point between the initial elastic stiffness and unloading stiffness corresponding to the peak stress σ_{t0}. In this method, a fixed point R_t which is preset in the stress-strain space can retain the computational efficiency in determining the unloading stiffnesses of UHPFRC under different loading histories throughout the moving process of wheel load in the composite deck.

The coordinate values of reference point R_t in Figure 2.4 are calculated by following equations

$$\varepsilon_{ref} = \frac{(\sigma_{t0} / E_u) - (E_{ru} / E_u)\varepsilon_{t0}}{1 - (E_{ru} / E_u)} \tag{2.8}$$

$$\sigma_{ref} = E_u \varepsilon_{ref} \tag{2.9}$$

$$E_{ru} = \frac{\sigma_{t0} - \sigma_{ref}}{\varepsilon_{t0} - \varepsilon_{ref}} \tag{2.10}$$

$$E_r = \frac{\sigma_{t\max} - \sigma_{ref}}{\varepsilon_{t\max} - \varepsilon_{ref}} \tag{2.11}$$

where ε_{ref} and σ_{ref} are the strain and stress values at reference point R_t

E_r and E_{ru} are the unloading stiffness corresponding to σ_{max} and σ_{t0}, respectively.

The unloading mechanism of UHPFRC in compression in this study is specified in Figure 2.2(b). The second-order relations are assumed for the unloading curves of UHPFRC under both tension and compression following the equations (2.12) and (2.13) as follows

In tension: $\sigma = \sigma_{t\max} \left(\dfrac{\varepsilon - \varepsilon_r}{\varepsilon_{t\max} - \varepsilon_r} \right)^2$ $\tag{2.12}$

In compression: $\sigma = \sigma_{c\max} \left(\dfrac{\varepsilon}{\varepsilon_{c\max}} \right)^2$ $\tag{2.13}$

where ε_{cmax} is the historic maximum level of compressive strain corresponding to σ_{cmax}.

2.3.3 Shear transfer in cracked UHPFRC

Considering the post-cracking response of UHPFRC, it is found that the shear stresses can be transferred through the crack surface due to the existence of the pull-out fibers and the aggregate interlocking, as illustrated in Figure 2.5. The shear modulus is normally reduced with the increase of tensile strain, which represents a reduction of the shear stiffness due to crack opening. Hence, in the current study, a shear retention factor λ, which is a parameter quantifying the shear force transfer in cracked UHPFRC, is introduced and expressed as a function depending on maximum tensile strain ε_{tmax} as follows

$$\lambda = \frac{1}{1 + \beta \varepsilon_{t\max}} \tag{2.14}$$

where coefficient $\beta = 4447$ is chosen referring to study of Fairbairn et al. [35].
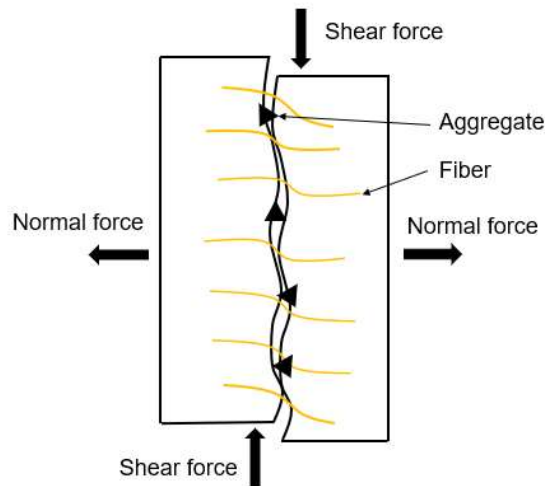
Figure 2.5 Shear transfer in cracked UHPFRC

2.3.4 Multi-fixed smeared crack model for UHPFRC

In finite element method, the cracking of concrete material is primarily represented by the discrete crack (or fictitious crack) model and the smeared crack (or crack band) model. The discrete crack model represents a crack as a discontinuous body where the mesh is

separated with the unlinking nodes, while the smeared crack model assumes a cracked element as a continuum in which the crack band is smeared over the element width, as illustrated in Figure 2.6. Despite the closely reflection of the actual crack with the element discontinuity in the discrete crack approach, it is more convenient to apply the smeared crack model in which the topology of the original mesh is preserved by switching the initial isotropic constitutive law to an orthotropic relation with the axes of orthotropy after crack formation determined by the cracking criteria.

In the current study, the 3D eight-node smeared crack elements which are developed based on a multiple fixed crack model [29] are used to represent the cracking behaviors, i.e., crack formation and propagation, of UHPFRC material.

(a) (b)
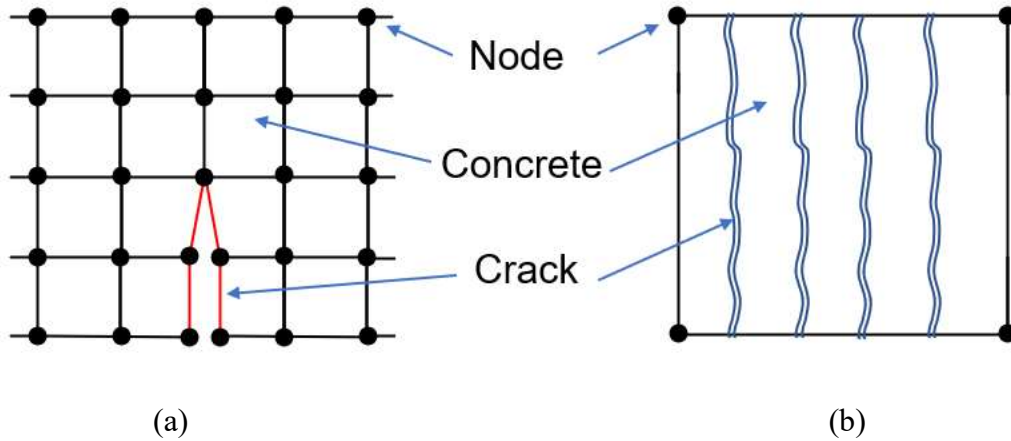
Figure 2.6 Cracking model: (a) Discrete crack, (b) Smeared crack

In the fixed smeared crack model applied for concrete material, the total cracking strain in global coordinate system of a cracked body are decomposed into non-cracked and cracked components elastic strain ε^{co} and crack strain ε^{cr} as follows

$$\varepsilon = \varepsilon^{co} + \varepsilon^{cr} \tag{2.15}$$

where ε^{co} and crack strain ε^{cr} are the strain component vectors of non-cracked and cracked concrete, respectively.

For non-cracked component of UHPFRC, the global stress-strain relationship of an elastic isotropic material with the modulus E and Poisson's ratio v is applied and expressed by

$$\sigma^{co} = D^{co}\varepsilon^{co}$$

$$
\begin{Bmatrix}
\sigma_{xx} \\
\sigma_{yy} \\
\sigma_{zz} \\
\tau_{xy} \\
\tau_{yz} \\
\tau_{zx}
\end{Bmatrix}
=
\frac{E}{(1-2\nu)(1+\nu)}
\begin{bmatrix}
1-\nu & \nu & \nu & 0 & 0 & 0 \\
\nu & 1-\nu & \nu & 0 & 0 & 0 \\
\nu & \nu & 1-\nu & 0 & 0 & 0 \\
0 & 0 & 0 & \dfrac{1-2\nu}{2} & 0 & 0 \\
0 & 0 & 0 & 0 & \dfrac{1-2\nu}{2} & 0 \\
0 & 0 & 0 & 0 & 0 & \dfrac{1-2\nu}{2}
\end{bmatrix}
\begin{Bmatrix}
\varepsilon_{xx} \\
\varepsilon_{yy} \\
\varepsilon_{zz} \\
\gamma_{xy} \\
\gamma_{yz} \\
\gamma_{zx}
\end{Bmatrix}
\quad (2.16)
$$

where D^{co} is the elastic stiffness matrix of non-cracked concrete

σ^{co} and ε^{co} are the stress and strain vectors of non-cracked UHPFRC in global coordinate system showed in Figure 2.7(a), respectively.

(a)   (b)
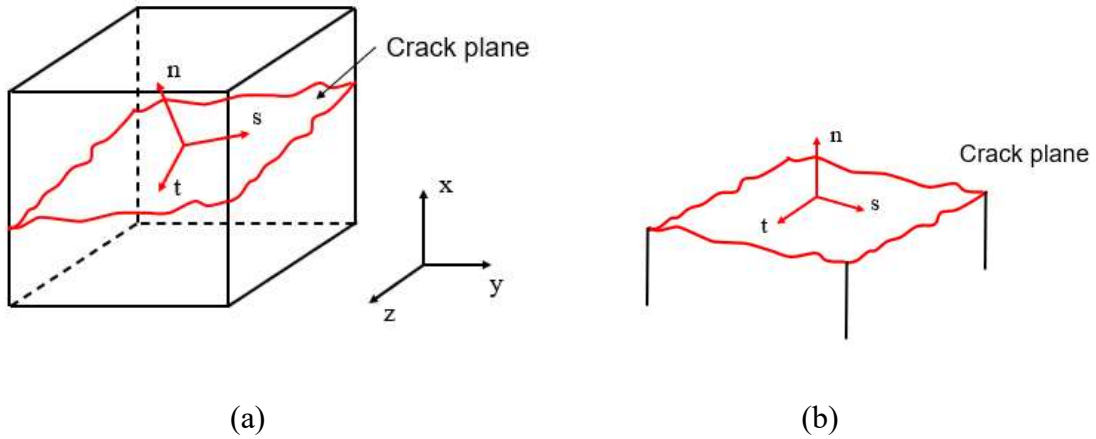
Figure 2.7 Crack formation in 8-node smeared crack element: (a) Global coordinate, (b) Local coordinate at crack plane

For cracked component of UHPFRC, with the assumption that there is no dilatancy between normal and shear terms, the stress-strain relation with respect to the local coordinate system at crack plane (as illustrated in Figure 2.7(b)) can be represented by

$$\sigma^{cr} = D^{cr} e^{cr}$$

$$
\begin{Bmatrix} \sigma_{nn} \\ \sigma_{ss} \\ \sigma_{tt} \\ \tau_{ns} \\ \tau_{st} \\ \tau_{tn} \end{Bmatrix} =
\begin{bmatrix}
d_n^{cr} & 0 & 0 & 0 & 0 & 0 \\
0 & d_s^{cr} & 0 & 0 & 0 & 0 \\
0 & 0 & d_t^{cr} & 0 & 0 & 0 \\
0 & 0 & 0 & \lambda G & 0 & 0 \\
0 & 0 & 0 & 0 & G & 0 \\
0 & 0 & 0 & 0 & 0 & \lambda G
\end{bmatrix}
\begin{Bmatrix} \varepsilon_{nn} \\ \varepsilon_{ss} \\ \varepsilon_{tt} \\ \gamma_{ns} \\ \gamma_{st} \\ \gamma_{tn} \end{Bmatrix}
\tag{2.17}
$$

where σ^{cr} and ε^{cr} are the local crack stress and strain vectors, respectively

D^{cr} is the stiffness matrix of an UHPFRC crack

d_n^{cr}, d_s^{cr} and d_t^{cr} are the normal stiffness of cracked UHPFRC in local n, s and t axes

G is shear modulus, $G = \dfrac{E}{2(1-\nu)}$

λ is shear retention factor, as represented in section 2.3.3.

Eventually, the overall stress-strain relationship consisting of the elastic and cracked stiffness matrices of UHPFRC in the global coordinate system can be obtained following the procedure proposed by Rots and Blaauwendraad [29] as expressed by

$$\sigma = D^{cocr} \varepsilon$$

$$\sigma = \left[D^{co} - D^{co} N (D^{cr} + N^T D^{co} N)^{-1} N^T D^{co} \right] \varepsilon \tag{2.18}$$

where N is transformation matrix corresponding to the crack orientation as follows

$$
N = \begin{bmatrix}
n_{11}^2 & n_{11}n_{12} & n_{13}n_{11} \\
n_{21}^2 & n_{12}n_{22} & n_{23}n_{12} \\
n_{31}^2 & n_{13}n_{32} & n_{33}n_{13} \\
2n_{11}n_{21} & n_{11}n_{22}+n_{12}n_{21} & n_{11}n_{32}+n_{12}n_{31} \\
2n_{21}n_{31} & n_{12}n_{23}+n_{13}n_{22} & n_{12}n_{33}+n_{13}n_{32} \\
2n_{31}n_{11} & n_{13}n_{21}+n_{11}n_{23} & n_{13}n_{31}+n_{11}n_{33}
\end{bmatrix}
\tag{2.19}
$$

The components n_{i1}, n_{i2} and n_{i3} form the vectors which indicate the direction of the global coordinate and the local n, s and t axes, respectively.

2.3.5 Bridging stress degradation of UHPFRC subjected to fatigue loading under dry and surface water conditions

In this study, a bridging stress degradation characteristic is introduced for UHPFRC material to reproduce the fatigue behaviors of the composite deck. Under repetitive loading, the bridging stress degradation which was proposed by Li and Matsumoto [14] is considered as a primary degradation mechanism inducing the propagation of fatigue crack in normal concrete and fiber reinforced concrete [14-19]. For UHPFRC, the progressive degradation of the bridging stress in the fracture process zone under tensile fatigue is mainly attributed to the deteriorations of the fiber component, i.e., fiber fatigue rupture and gradual fiber pullout due to interfacial bond decay [11]. The propagation process of the existing cracks in UHPFRC is thus promoted by these deteriorations. As stated by Li and Matsumoto [14], the bridging stress degradation can be simply assumed by a function of two parameters, i.e., maximum tensile strain ε_{tmax} and number of cycle N. Correspondingly, the reduction relation of bridging stress applied for UHPFRC material in this study can be expressed by

$$\frac{\sigma_N}{\sigma_1} = f(\varepsilon_{t\max}, N) \leq 1$$

$$\frac{\sigma_N}{\sigma_1} = 1 - (a_0 + a_1 \varepsilon_{t\max}) \log(N)$$

(2.20)

where σ_N/σ_1 is bridging stress degradation ratio between the N_{th} and the first cycles.

a_0 and a_1 are the coefficients depending on the material and testing conditions (e.g., dry or water conditions).

2.3.5.1 Bridging stress degradation of UHPFRC subjected to fatigue loading under dry condition

As reported by Khan et al. [36], the four point bending test of the UHPFRC beams has been conducted subjected to the load-controlled fatigue flexure under dry condition, as shown in Figure 2.8. Under the flexural loading, a microcrack formed in the strain hardening domain UHPFRC occurs at the midspan of the testing beam. When only micro-portion of this crack at the midspan of flexural beam is examined, this part can be

considered as a fine crack under uniaxial fatigue loading, as illustrated in Figure 2.9. Accordingly, the obtained bridging stress degradation relation represents the degradation rate of transferred stress across the multiple fine cracks formed in strain-hardening domain of UHPFRC. Due to the high cracking and tensile strengths of UHPFRC, this kind of multiple fine cracks formed dominantly in the OSD-UHPFRC composite deck in comparison to the localized cracks. In the current composite deck, no localized macrocrack formed in strain-softening domain of UHPFRC is found in overlay throughout the fatigue test. Therefore, the bridging stress degradation relation of cracked UHPFRC under load-controlled flexural fatigue is considered adequate to be applied to the analytical model for reproducing the fatigue behaviors of the composite deck under moving wheel loading.

The S-N relationships of UHPFRC material under dry condition is then obtained by this research, as plotted in Figure 2.10. It is found that a much slower speed of fatigue degradation with a higher endurance limit of UHPFRC is obtained, in comparison to the other conventional fiber reinforced cementitious composite materials such as Fiber Reinforced Concrete (FRC) or Engineered Cementitious Composite (ECC).

Subsequently, based on the S-N relationships obtained in [36], the bridging stress degradation model of UHPFRC is derived by Jimi et al. [37] in the analysis by the trials of the coefficients a_0 and a_1 represented in Equation (2.20) until the FEM results fit with the experimental data. As shown in Figure 2.10, the chosen of the coefficients a_0 and a_1 as 0.015 and 5 can give a well-fitting between analysis and experiments. For the normal concrete and PVA-ECC, it was reported that the values of coefficients $a_0 - a_1$ are $0.08 - 4$ and $0.025 - 15$, respectively [18]. Hence, the fatigue durability of UHPFRC is clearly higher than the other cementitious materials [37].

In the current model of the UHPFRC/steel composite bridge deck under dry condition, the coefficients a_0 and a_1 of 0.015 and 5 are chosen for the fatigue bridging stress degradation model of UHPFRC, following the mentioned studies.
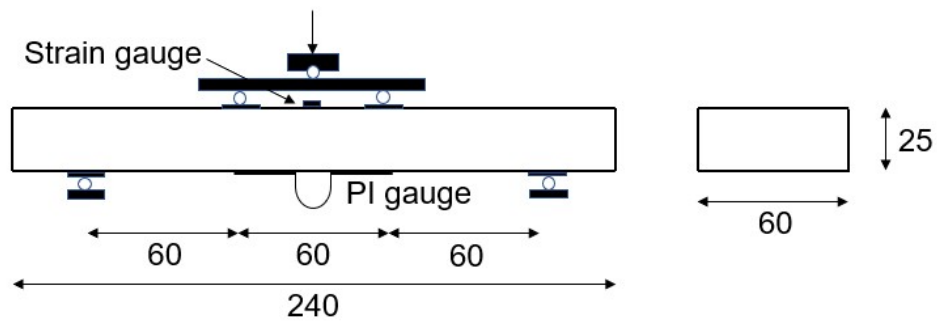
Figure 2.8 Fatigue flexural test of UHPFRC beam [36] (all dimensions are in mm)
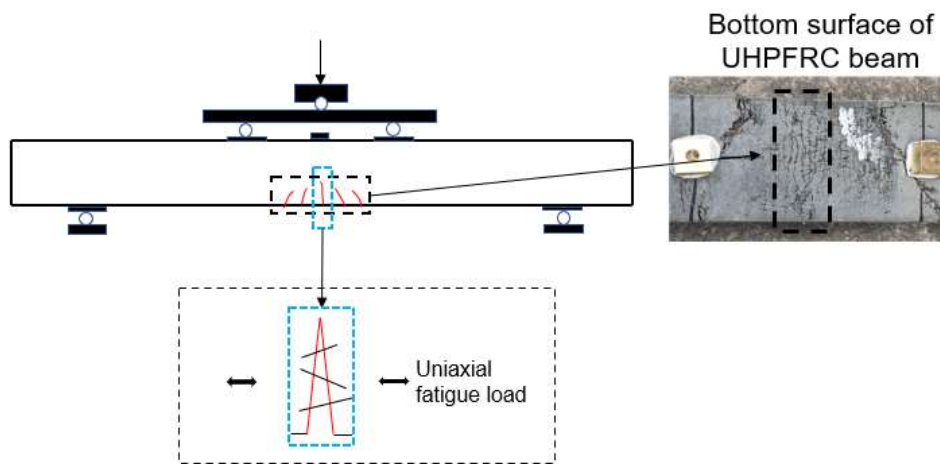
Figure 2.9 Micro portion of the middle crack under fatigue loading [36]
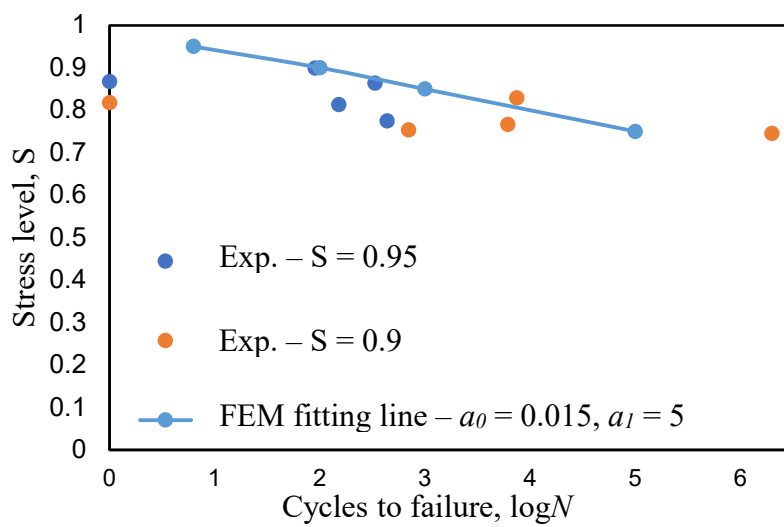
Figure 2.10 Stress-life (S-N) relationships of UHPFRC [37]

2.3.5.2 Bridging stress degradation of UHPFRC subjected to fatigue loading under surface water condition

For the UHPFRC-steel composite bridge deck, stagnant water caused by rainfalls may pool over the UHPFRC overlay and penetrate into the microcracks on the top surface of this reinforcing layer, which may lead to more severe fatigue deteriorations on the composite deck under moving wheel loading. The influence of stagnant water on the structural performance of the reinforced concrete (RC) bridge decks has been examined by Matsui [41,42]. It was found that the stagnant water on the top surface of RC bridge decks from rainfall considerably degraded the fatigue performance of bridge slabs, and the reduction in fatigue life of the RC bridge decks under surface water condition was about 1/200 of that from the RC slabs tested in dry condition [42].

Several experimental studies on the fatigue performance of concrete have been conducted under water condition, and it was also reported that water had a negative impact on the fatigue performance of concrete material [43-45]. Under the rapid deformation of concrete cracks, i.e., closing-opening process under fatigue loading, the sharp rise or fall of the pore water pressure could be obtained due to the hard dispersion of condensed water inside the cracks [44]. This might lead to the acceleration of the damage of concrete material since the pore pressure was transmitted to the capillary pores, which are mostly located around the aggregate/matrix interface [46]. Following the studies of Matsushita [45, 47], the S-N relation equations for concrete under dry and water conditions were presented as follows

- Under dry condition: $\log N = 17.5\left(1 - \dfrac{S_r}{1 - S_{min}}\right) = 17.5\left(\dfrac{1 - S_{max}}{1 - S_{min}}\right)$ (2.21)

- Under water condition: $\log N = 11.7\left(1 - \dfrac{S_r}{1 - S_{min}}\right)$ (2.22)

where $S_{max} = \sigma_{max}/\sigma_{ult}$ is the applied maximum stress ratio

      $S_{min} = \sigma_{min}/\sigma_{ult}$ is the applied minimum stress ratio

$S_r = S_{max} - S_{min}$ is the applied stress range ratio

From Equations (2.21) and (2.22), for the case of the applied minimum stress equal to zero ($S_{min} = 0$), it was found that the fatigue stress range ratio at 2 million cycles for concrete in water condition is about 70% of that in dry condition. In the current study of the UHPFRC-steel composite bridge deck, by applying this reduction percentage from the fatigue life of concrete material to that of UHFPRC (as shown in Figure 2.11), the corresponding coefficients a_0 and a_1 from the bridging stress degradation relation of UHPFRC under surface water condition are then calculated as 0.058 and 3.5, respectively.
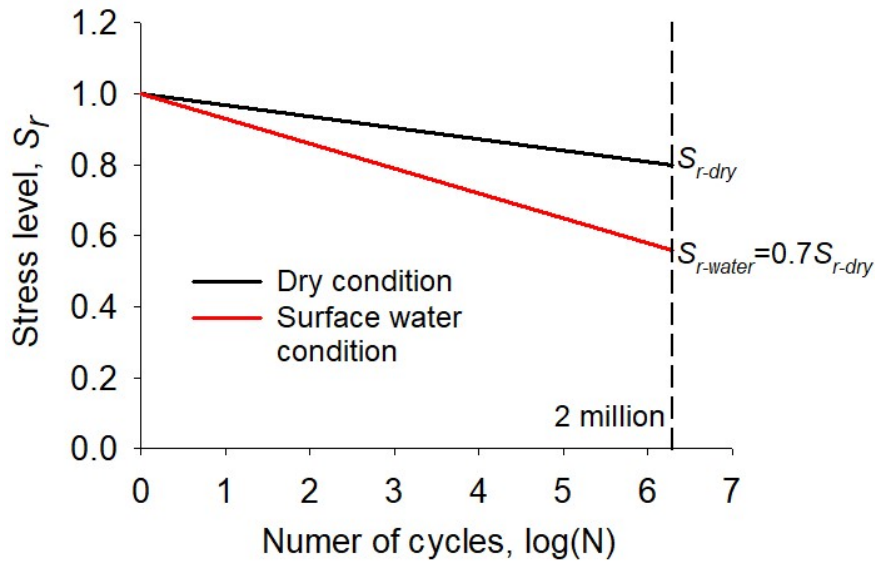
Figure 2.11 S-N relations for UHPFRC under dry and surface water condition

2.3.6 Self-healing behavior of UHPFRC under surface water condition

Under the condition of water exposure without considering the fatigue action of applied loading, the autogenous self-healing capacity of High Performance Fiber Reinforced Cement Composites (HPFRCC) in terms of the crack closure and the mechanical recoveries has been investigated in many studies [48-55]. Following the study of Okuizumi et al. [48], under water condition, UHPFRC exhibited the high self-healing ability represented by the high percentage of crack closure observed from the bottom of the flexural UHPFRC beams, as illustrated in Figure 2.12. After only one day of water exposure, the closure percentage of UHPFRC fine cracks with the maximum width of

0.014 mm in the specimens could reach over 77%. Herbert and Li [49, 50] have examined the self-healing behavior of Engineered Cementitious Composite (ECC) in the natural environment. It is found that, accompanied with the closure of cracks caused by the continued hydration of un-hydrated cement grains, there were the mechanical recoveries of reloading stiffness and first cracking strength in the ECC specimens after crack healing in water condition. Under the wet-dry cycles, the self-healing characteristic of high tensile ductility ECC materials has been investigated by Kan and Shi [53]. It was also reported that both the ultimate tensile strength and the tensile strain capacity of the ECC specimens at reloaded stage were higher than those from the control specimens without undergoing the wet-dry healing cycles.
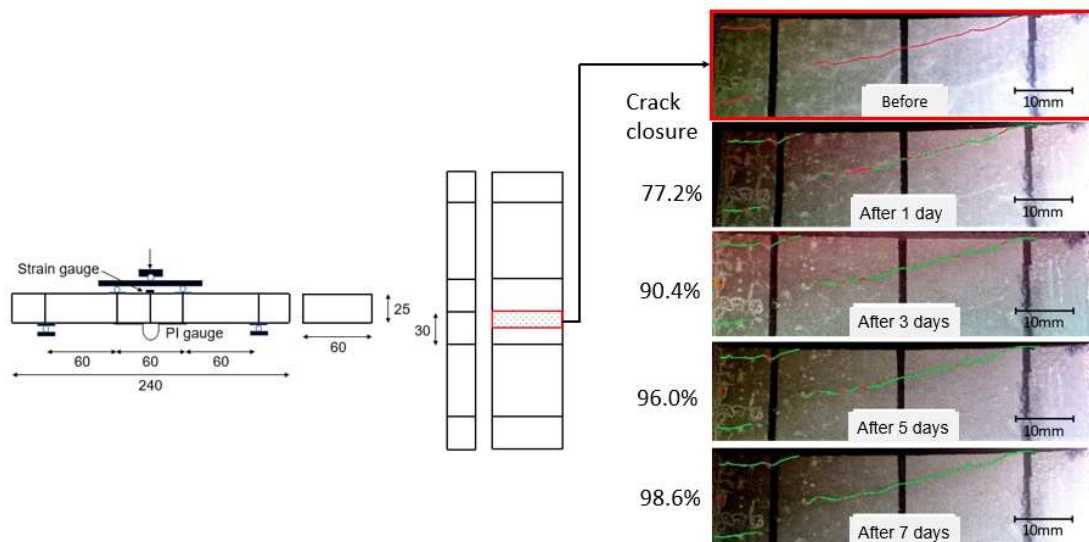
Figure 2.12 Crack closure percentages versus exposed time in water under bottom of the flexural UHPFRC beams [48]

From the fatigue test of the UHPFRC/steel composite bridge deck, after the first stage with 1,100,000 cycles under moving wheel loading with rubber tire under dry condition, the composite deck was subsequently tested for 60,000 cycles under surface water condition in one day. A thin layer of water had been supplied on the top surface of UHPFRC overlay for one night before the fatigue test under surface water condition. Correspondingly, in the current analysis, the mechanical recoveries in term of reloading stiffness and tensile strength caused by the autogenous self-healing are applied to the

cracked UHPFRC from the end of dry condition (1,100,000th cycle) to the beginning of surface water condition (1,100,001st cycle), as shown in Figure 2.13. The recovery ratios for the reloading stiffness, κ, and the tensile strength, ξ, in the cracked UHPFRC are represented as follows

$$\kappa = \frac{K_{1,100,001} - K_{1,100,000}}{K_1 - K_{1,100,000}} \tag{2.23}$$

$$\xi = \frac{\sigma_{1,100,001} - \sigma_{1,100,000}}{\sigma_1 - \sigma_{1,100,000}} \tag{2.24}$$

where K_1 is the elastic stiffness at the first cycle

$K_{1,100,000}$ and $K_{1,100,001}$ are the reloading stiffnesses at the 1,100,000th and 1,100,001st cycles, respectively.

σ_1, $\sigma_{1,100,000}$ and $\sigma_{1,100,001}$ are the crack bridging stresses at the first, 1,100,000th and 1,100,001st cycles, respectively.
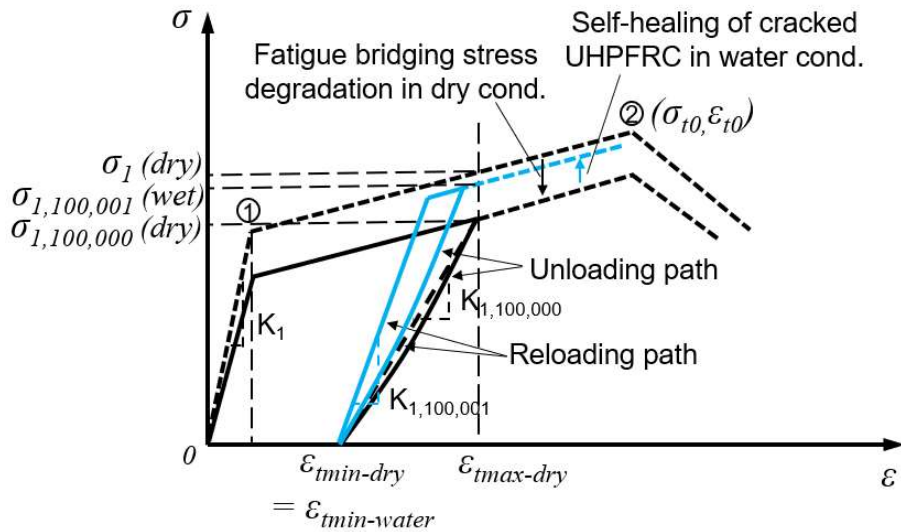
Figure 2.13 Tensile stress-strain relation of cracked UHPFRC under surface water condition

2.4 Fatigue bond stiffness degradation at the UHPFRC/steel interface

As significant as the fatigue behaviors of UHPFRC overlay, the bonding performance between the OSD and the overlaid reinforcement may considerably influence the

effectiveness of this rehabilitation technique. The method with the shear studs welded on the top surface of steel plate has been used in many researches [6, 7]. However, the welded studs may produce more fatigue susceptible details in the composite structure. One possible method without using the welding connections is gluing the reinforced overlay to the OSD by only the epoxy resin adhesive [24]. For the current UHPFRC-steel composite bridge deck, the bonding technique using epoxy resin combined with hard aggregates, i.e., synthetic ceramics, is applied as illustrated in Figure 2.14.
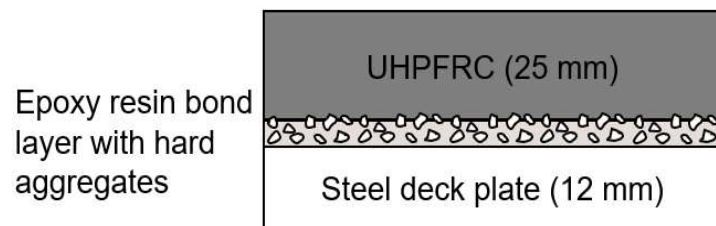
Figure 2.14 Bond surface between the UHPFRC overlay and steel deck plate

As a common technique used to adhere the reinforced overlay to the steel deck, the performance of the epoxy-based bond layer used in OSD with surfacing concrete are typically evaluated by the static tests specified by the standard design, e.g., the direct pull-off test or static flexural test of composite specimens. For the bond technique used in the current UHPFRC-steel composite deck, a pull-off tensile test of the UHPFRC-steel core specimens has been conducted by Mi [25]. It was found that the average tensile bond strength of the current bond technique was 2.91 MPa, and the failure of the core specimens did not occur at the bonding layer, as shown in Figure 2.15. Furthermore, a static 3-point bending test of a small-scale UHPFRC-steel plate (see Figure 2.16) has been carried out to determine the failure mode of composite specimen under bending, as reported by Mi [25]. It is found that the UHPFRC layer failed under tensile cracking at the midspan of specimen, followed by the yielding of steel plate without the debonding of the adhesive layer. The mentioned bond tests have demonstrated the high performance of the developed bond technique under static loading.
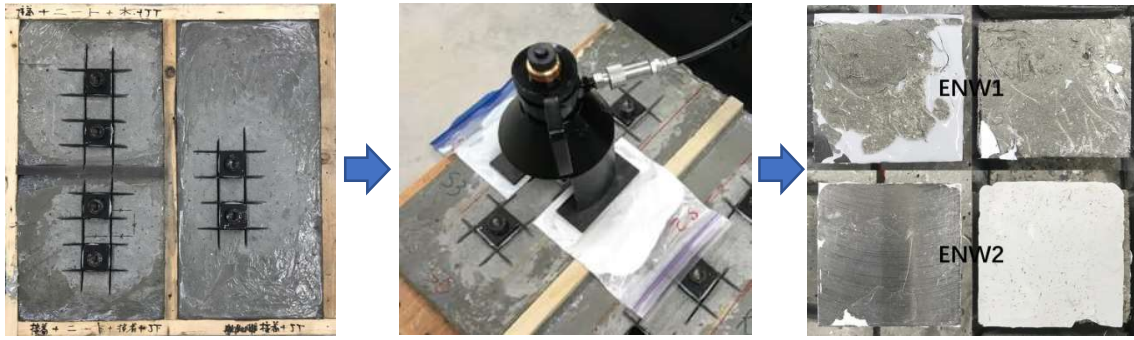
Figure 2.15 Pull-off tensile test of the UHPFRC-steel core specimens from Mi [25]

(a) Plane view of UHPFRC-steel composite plate
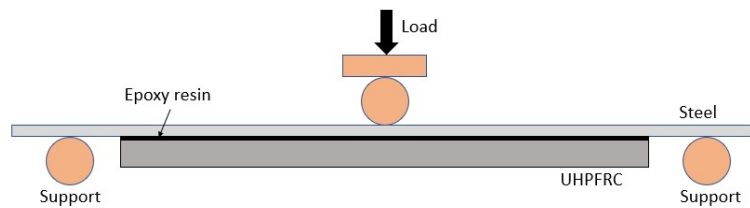
(b) 3-point bending test of UHPFRC-steel plate

(c) Crack localization under the bottom of UHPFRC layer at final failure

Figure 2.16 Static 3-point bending test of a small-scale UHPFRC-steel plate [25]

Nevertheless, under fatigue loading, the fatigue bond failure in shear direction between the thin thickness concrete surface and steel deck plate may happen. The issue of interfacial bond stiffness reduction under repetitive cyclic loading has been experimentally investigated from the shear bond tests of the FRP-concrete lap joint specimens by Dai et al. and Yun et al. [26, 27]. Under a repetitive cyclic loading, the progressive degradation of the interfacial bond stiffness along with the increase in the

bond slip displacement has been reported (see Figure 2.17). Based on those studies, the regression analysis of the available experimental data was carried out by Loo [28]. It was found that the interfacial bond stiffness degradation is dependent on the bond stress range-to-failure stress ratio and the number of load cycles. Figure 2.18 shows the fatigue degradation of the interfacial bond stiffness from the FRP-concrete lap joint specimens in a relationship between the bond shear stress τ and the bond slip displacement S. In Figure 2.18(a), S_1 and S_2 are the bond slip corresponding to bond shear strength τ_{max} and the ultimate bond slip displacement, respectively. The interfacial bond stiffness degradation relation represented by Figure 2.18(b) was obtained by Loo [28] as follows

$$K_{bN} = K_{b1}\left[1 - 190.3(\log N)^{0.99}.\left(\frac{\Delta\tau}{\tau_f}\right)^{8.797} \right] \qquad (2.25)$$

where K_{b1} and K_{bN} are the interfacial stiffness of the Nth and the first cycles, respectively

$\Delta\tau$ is the bond stress range

τ_f is the bond stress at failure
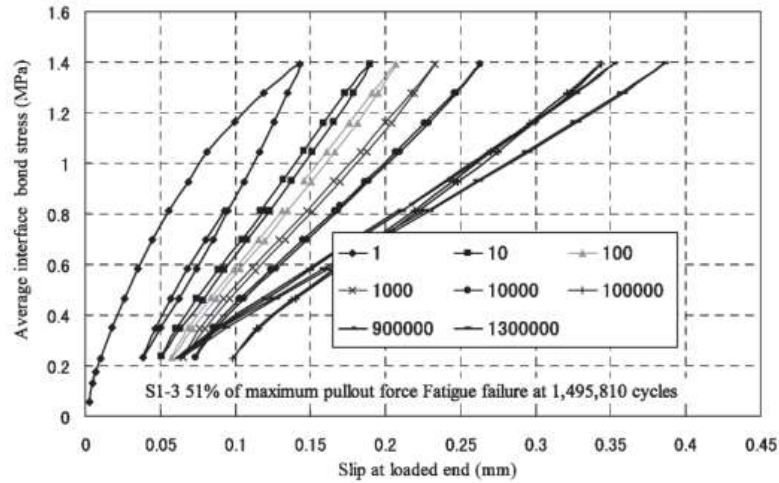
Figure 2.17 Bond-slip relationships under fatigue loading of CFRP/concrete joints from Dai et al. [26]

26
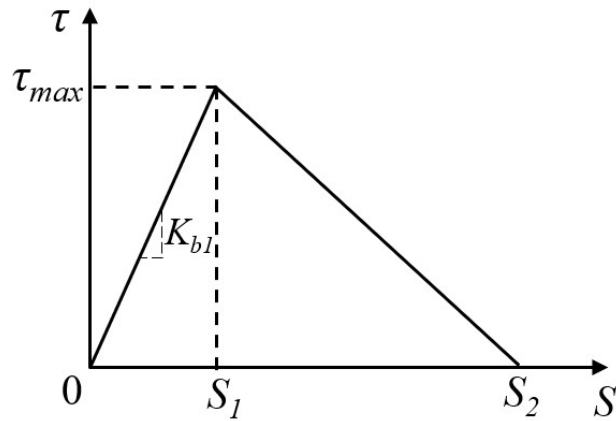
(a) Static bilinear bond-slip relationship at interface layer
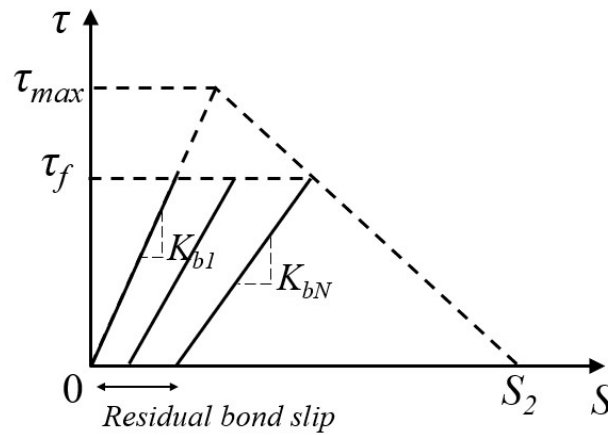
(b) Interfacial bond stiffness degradation under fatigue loading

Figure 2.18 Fatigue degradation of interfacial bond stiffness under fatigue cyclic loading [28]

Based on Equation (2.25), it is known that, corresponding to each constant value of the applied shear stress-to-bond strength ratio, the linear relationship between the bond stiffness degradation and the number of loading cycles N was obtained with the constant value of degradation slope. In the current study of the UHPFRC/steel composite bridge deck, due to the lack of data about the bond shear strength as well as the ultimate bond slip between steel plate and developed UHPFRC, the degradation in the shear component of the interfacial bond stiffness is simply assumed by a function of the number of cycles N in the analysis as follows

$$\frac{E_{bN}}{E_{b1}} = f(N) = 1 - b_0 \times \log N \qquad (2.26)$$

where E_{bN} and E_{b1} are the interfacial bond stiffness of the Nth and the first cycles, respectively.

b_0 is the slope of the bond stiffness degradation line.

The interfacial bond stiffness degradation under fatigue moving wheel load is illustrated in Figure 2.19, where τ and γ are the bond shear stress and the corresponding bond shear strain. Due to the insufficient data about the residual bond slip displacement under fatigue loading between UHPFRC and steel, the interfacial residual strain at the zero bond stress level is also neglected in the current analysis.
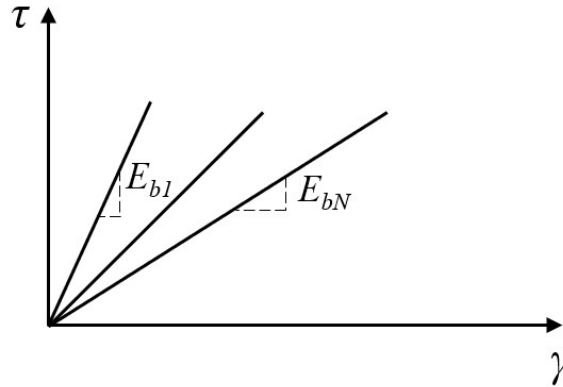
Figure 2.19 Interfacial bond stiffness degradation model under fatigue moving wheel loading

In this study, the simplified degradation equation of interfacial bond stiffness with one influential parameter, i.e., number of loading cycles, is used as shown in Equation (2.26), that roughly reproduces the fatigue degradation phenomenon reported from the previous studies when the number of loading cycles increases [26-28]. A semi-automatic method is then carried out. This method combines the Equation (2.26) in the analytical model with experimental observations, e.g., observed delamination area under UHPFRC, abnormal sound ranges from hammer test as well as the strain results in steel deck plate. Based on these observations, the interfacial region that is applied for the bond stiffness degradation in Equation (2.26) can be determined.

CHAPTER 3 STATIC ANALYSIS OF THE UHPFRC-STEEL COMPOSITE BRIGDE DECK UNDER A WHEEL LOADING WITH RUBBER TIRE

3.1 Introduction

In this chapter, a non-linear 3D FEM model was performed to investigate the static behaviors of the UHPFRC-steel composite bridge deck under a wheel loading with rubber tire. The analytical model of the UHPFRC-steel bridge deck under the static wheel loading with rubber tire is constructed based on the viewpoint of approaching the actual conditions of the experiment of the composite deck as well as ensuring the numerical effectiveness, i.e., accurate estimation and computational-cost saving. The appropriate model chosen in the static analysis can be a solid base for the fatigue investigation of the bridge deck in the next step.

The strengthening effect of the UHPFRC overlay on the static performances of the steel bridge deck is also examined numerically in this chapter.

3.2 Multi-stage testing conditions from the fatigue test of the UHPFRC-steel composite bridge deck

3.2.1 Geometric descriptions

To investigate the beneficial effects of the UHPFRC reinforced layer in terms of improving the fatigue durability of the orthotropic steel bridge deck, a full-scale UHPFRC-OSD composite structure was experimentally tested under both the static and fatigue conditions of the wheel-type load in Civil Engineering Research Institute (CERI) for Cold Region, Hokkaido, Japan [9]. For the research and construction of major bridge projects, the full-scale testing of the OSD (or orthotropic panel) under a moving wheel loading is often performed, in which the dimensions of the deck plate are relatively small but sufficient to capture the fatigue behaviors of a real bridge deck. The orthotropic panel (local) is considered as a structural modular component that can be rapidly fabricated and assembled into an overall bridge cross-section (global) in any design geometry. The geometry of the UHPFRC-steel orthotropic panel in the fatigue test is described in Figure 3.1. The strengthened OSD is composed of the UHPFRC overlay, steel deck plate, main

girders, cross beams and longitudinal open bulb ribs. The dimensions of the deck plate are 3300 and 2720 mm in longitudinal and transverse directions, respectively. The steel deck with a thickness of 12 mm is overlaid by a 25 mm layer of UHPFRC. The main girder has an average depth of 690 mm and a thickness of 14 mm. The steel deck plate is stiffened by seven longitudinal bulb ribs with a size of 230×11×30 mm and three cross beams with 9 mm web thickness.
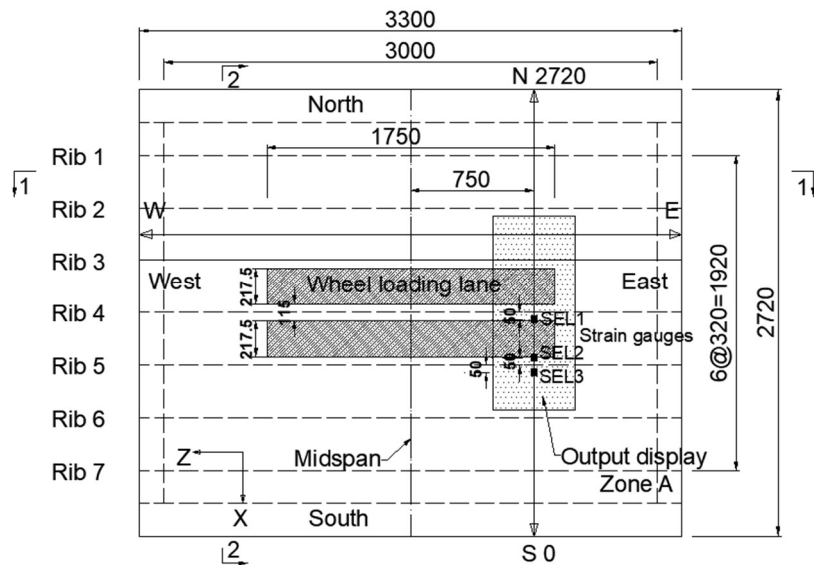
(a) Plan view of composite deck
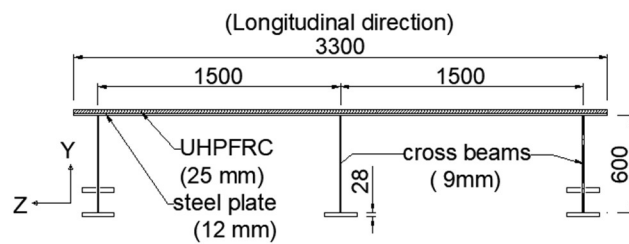
(b) Cross section 1-1 (side view)
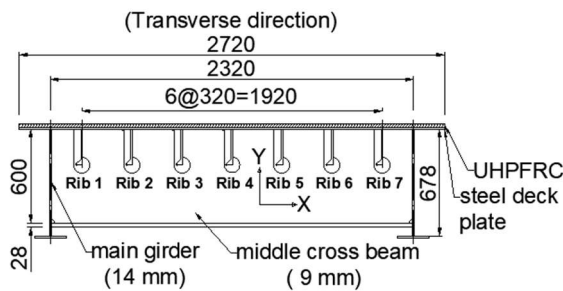
(c) Cross section 2-2 (front view)   (d) Details of longitudinal bulb rib
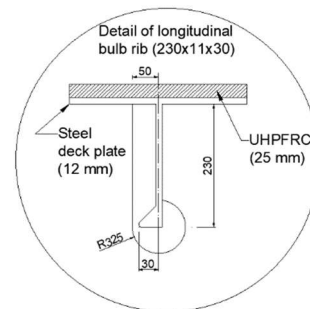
Figure 3.1 Description of composite deck geometry (all dimensions are in mm)

In this study, the fatigue life of the steel bridges is determined by the local stress ranges caused by the out-of-plane bending of the OSD components at the weld joint details, e.g., rib-to deck or rib-to-crossbeam details, etc., under the repetitive wheel load which typically fits within the distance between the longitudinal ribs. In the tested OSD, the loading system with the dual truck tire is used, where each tire is located within the rib's distance and symmetrically to each other about the middle longitudinal rib (Rib 4) to maximize the induced local transverse bending on the longitudinal ribs in the steel deck. Therefore, the local fatigue performances and serviceability of the steel members in the tested OSD structure subjected to the directly moving wheel load can be used as a representative for the global real bridge.

3.2.2 Multi-stage testing conditions from the fatigue test of the UHPFRC-steel composite bridge deck

A series of fatigue test has been conducted under multi stages of wheel loading and environmental conditions to examine the effectiveness of the UHPFRC overlay in improving the fatigue durability of the OSD. The testing conditions of the four main stages from the fatigue test are summarized in Table 3.1.

Table 3.1 Testing conditions of the four main stages from fatigue test

Stage		Load level (kN)	Number of cycles	Loading condition	Environmental condition
Stage 1	OSD reinforced by UHPFRC overlay	100	1,100,000	Rubber tire	Dry
Stage 2		100	60,000	Rubber tire	Surface water
Stage 3		150	10,000	Steel wheel	Dry
		200	160,000	Steel wheel	Dry
Stage 4	OSD only (tested until fatigue cracks at welding zone occur)	200	176,454	Steel wheel	Dry
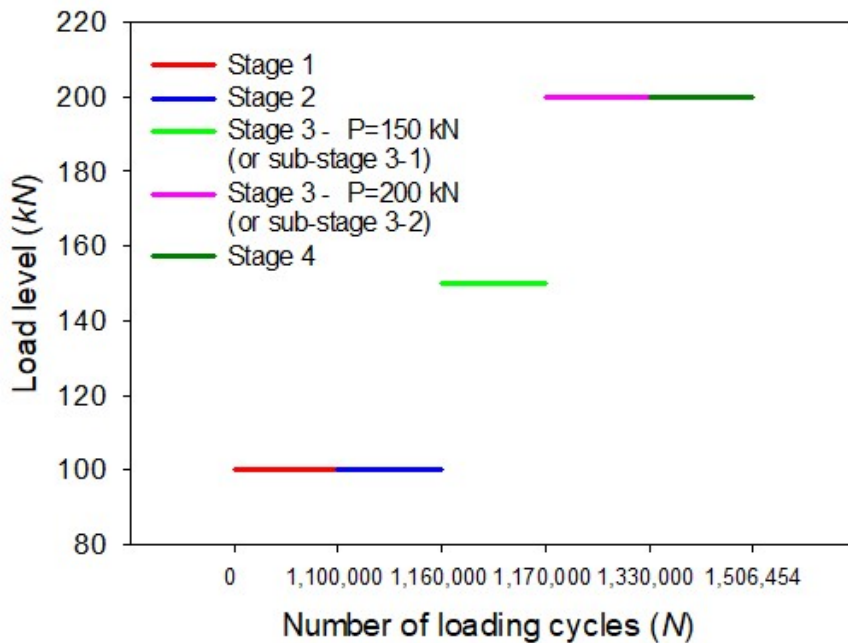
Figure 3.2 Loading program for the multi-stage fatigue test of the bridge deck

Loading program for the multi-stage fatigue test of the bridge deck is shown in Figure 3.2. It is noted that 1,000 cycles of a moving wheel loading with rubber tire have been applied to the OSD without UHPFRC reinforcing overlay before starting stage 1, to release the residual strain generated at the welding joints in the manufacturing process of the OSD. In the current study, the fatigue analysis is focusing on the structural performance of the OSD reinforced by UHPFRC overlay, i.e., stages 1 to 3 of the fatigue test.

3.3 Finite element modeling of the composite bridge deck under a wheel loading with rubber tire

The mesh pattern and boundary conditions of the UHPFRC-steel composite deck under a wheel loading with rubber tire are shown in Figure 3.3. The UHPFRC overlay is divided into three layers in the vertical direction with the fine mesh at the local regions above longitudinal ribs 3,4 and 5. According to Zhang et al. [6], except for the behaviors at some local positions, such as hotspot area and an area adjacent to the ribs, the overall structural behaviors of a steel deck with longitudinal bulb open rib can be well reproduced by both solid and shell elements in the FEM model. Therefore, to reduce the computational cost, the 4-node thick shell elements are used instead of the 8-node solid

element in the analysis for the steel members such as main girders, cross beams and 4 outer bulb ribs which are far away from the concerned and the critical middle parts under the two lanes of wheel load, as presented in Figure 3.3(b). Another analytical model of the composite deck that uses only 8-node solid elements is performed as well to confirm
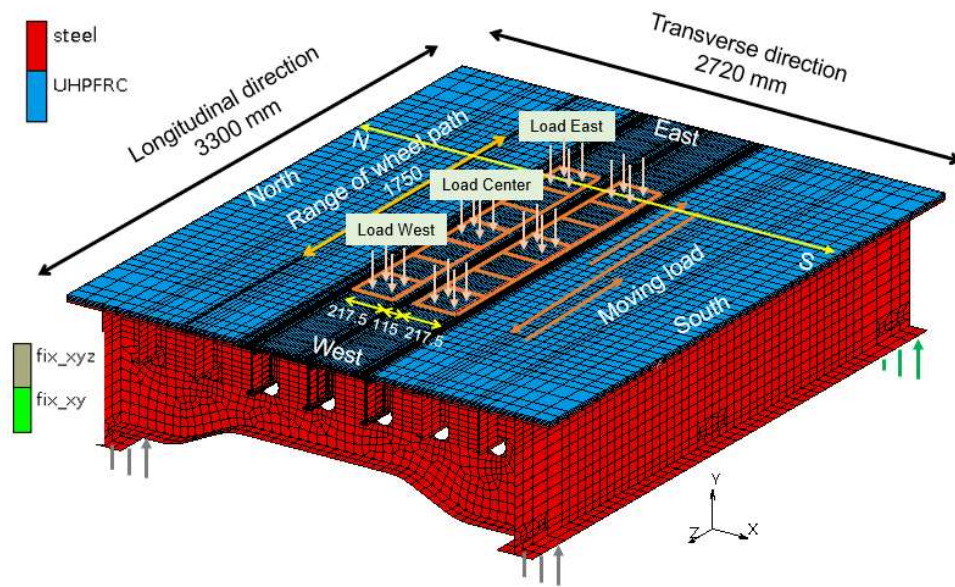
(a)
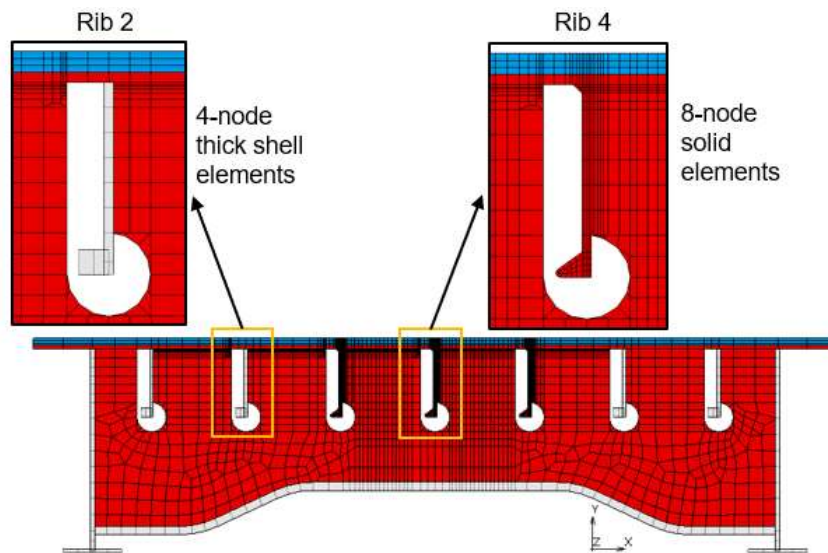
(b)

Figure 3.3 FEM model of UHPFRC-steel composite deck: (a) Boundary conditions of the OSD strengthened with UHPFRC overlay, (b) front view of the composite bridge deck.

the accuracy of the proposed model with the combined two types of elements. The number of elements from the proposed and latter models are 47390 and 62984, respectively. Despite the larger number of elements, the model with only 8-node solid elements does not give a significant improvement in the strain results in steel deck plate, due to the small impact of the 4 outer ribs on local regions above longitudinal ribs 3,4 and 5. It is found that the differences in maximum transverse strain level in steel plate at location of rib 4 between the two models are within 1%, while the analysis time of the latter model is about 40% longer than the proposed model. The considerable reduction in analysis time in the proposed model is meaningful, especially for the fatigue analysis with many load cases to reproduce the moving process of the wheel loadings in the next step.

Simple supports on a 3000-mm span are assigned at four outer edges under the flanges of two main girders. The pattern of the wheel loading lane is simulated as 2 paths along the longitudinal direction with a range of ± 875 mm from the midspan. The distance between two loading paths representing the gap between the two rubber tires is 115 mm at the middle of the transverse side. A load sequence consisting of seven load patches with a size of 2×217.5×250 mm, which is based on the experimental contact footprint of the rubber tire under static load at the Center location (see Figure 3.4(b)), is assigned along the loading lanes with a level of 100 *kN*. For convenience, the applied wheel load at Center and East (West) patches are named as load Center and load East (West) from now on, as shown in Figure 3.3(a).

The local performances of the orthotropic panel are governed by the wheel load, and the critical responses may be sensitive to the way that direct wheel loads are applied. The loading condition idealized by a uniformly distributed pressure of rectangular shape is commonly used to simulate the wheel tire load in bridge structures. However, for the case of the current experiment of OSD, the idealized model seems inadequate to reproduce the accurate strain responses in the steel deck, especially for the local region above Rib 4. Therefore, the model approaching the actual contact pressures produced by the rubber-tire loading is alternatively used in the current FEM model. Various studies on the truck tire-pavement contact stresses have indicated that the tire contact stresses are nonuniform

(All dimensions are in mm)

Transverse direction

217.5

47.15
7.7
30.8
7.7
30.8
7.7
30.8
7.7
47.15

250

Longitudinal direction
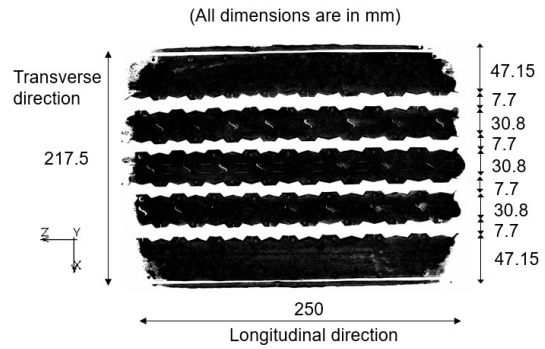
(a)   (b)

Figure 3.4 Rubber tire under static loading: (a) Static wheel load at Center location, (b) contact footprint of rubber tire [9]

224.5 mm

241 mm

Measured by the pressure-sensing pad (unit: kPa).
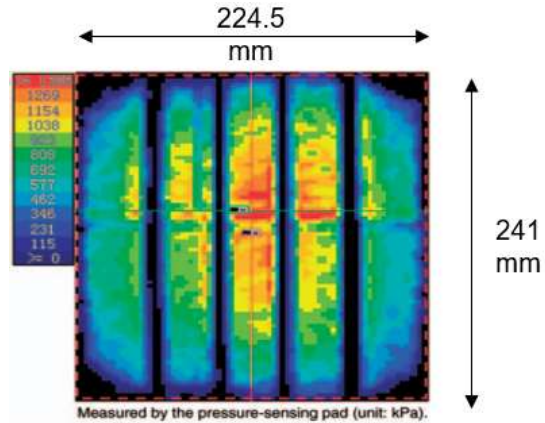
(a)   (b)

Figure 3.5 Rubber tire under static loading: (a) Static test with pressure-sensing pad, (b) contact normal pressure of rubber tire. [39]

along both the rolling and transverse directions of contact footprint [39, 40]. Wang et al. [39] have conducted the experiment using the pressure-sensing pad to measure the static normal pressure under a radial truck tire with four tire tread grooves. As can be seen in Figure 3.5, the obtained contact footprint with the measured area of 224.5×241 mm (transverse × longitudinal) is approximate to that from the experiment of the current composite deck. Besides, the wheel camber angle of zero is controlled by the testing machine in [39], which is similar to the wheel camber condition in the current research.

Therefore, the normal pressure distribution provided in [39] is used as a reference in this analysis.

From [39], along the transverse direction, there is a concentration of normal pressure at the middle of tire patch, that the stresses from two edges of contact patch are about 60 percent of the pressure at the centerline, as shown in Figure 3.6(a). Along the longitudinal or rolling direction, the isosceles trapezoidal distribution of contact stress is observed, where the top base of trapezoidal shape is about 0.6 of the patch longitudinal dimension (see Figure 3.6(b)). Based on these observations, the nonuniform distribution of the wheel loading with rubber tire is taken into account in the current analysis, as shown in Figure 3.7. For the transverse direction, the tire tread grooves with dimensions obtained from the experimental footprint are simulated (see Figure 3.7(a)). An isosceles trapezoidal distribution of contact stress is applied for the longitudinal side of load patch, and the vertical stress at the top base of the trapezoidal shape is calculated to be about 1.25 times of the uniformly distributed pressure, $\sigma_{uniform}$, as represented in Figure 3.7(b). In Figure 3.8, the normal pressure in the vertical direction on load patch from the current analytical model is plotted comparatively to the model applied uniform distribution of wheel load. It can be seen that the obtained distribution agrees with the actual measured-patch from Wang et al [39] rationally well.

(a)   (b)
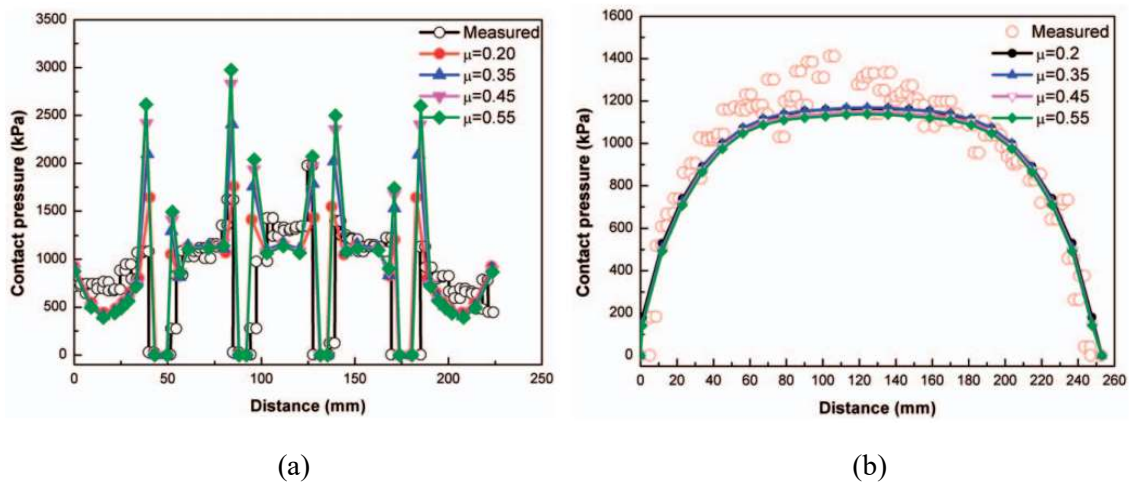
Figure 3.6 Measured data of the normal pressure distributions in the contact patch: (a) Along transverse centerline, (b) along longitudinal centerline. [39]
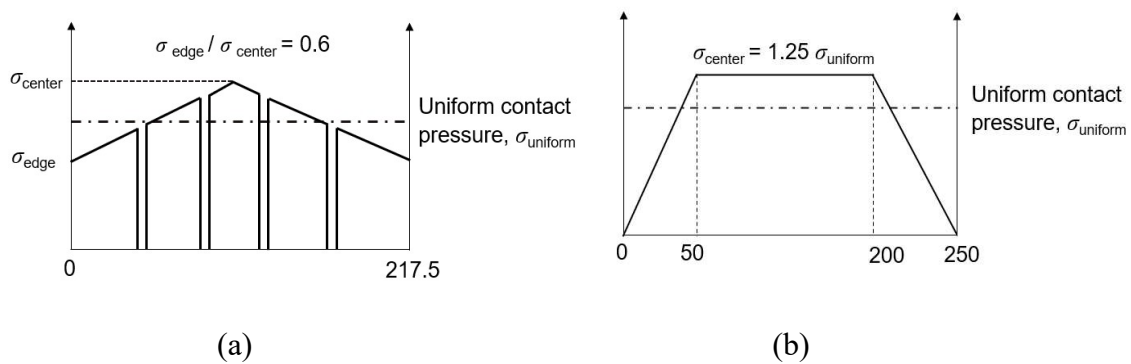
Figure 3.7 FEM model of contact pressure by rubber tire at each contact load patch: (a) Nonuniform distribution along transverse direction with tire tread grooves, (b) Trapezoidal distribution along longitudinal direction
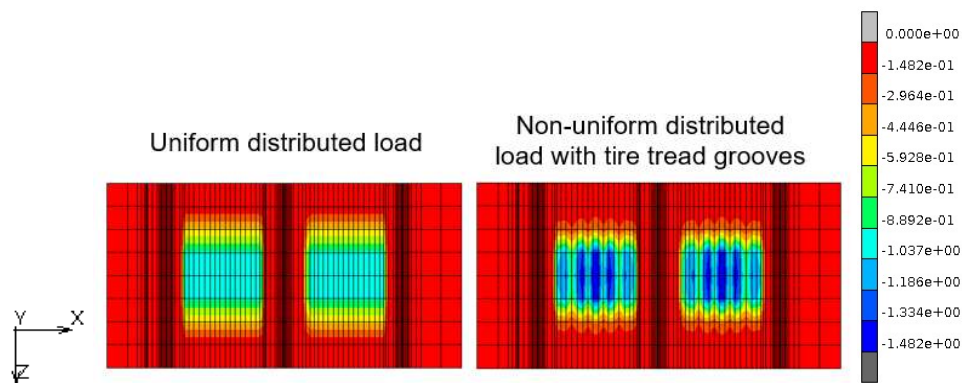
Figure 3.8 Normal pressure distributions in vertical direction on contact load patch

For FEM modeling of UHPFRC/steel interface, the contact GLUE condition in Marc program is applied to assembly the OSD structure and the reinforced overlay. The bottom layer of UHPFRC and the steel deck plate are defined as the deformable bodies in the contact analysis, as illustrated in Figure 3.9. The activation of GLUE condition is controlled by the CONTACT INTERACTION settings via the CONTACT TABLE option. Then, in the COHESIVE CONTACT of GLUE condition, the interfacial finite contact stiffnesses are specified with the elastic modulus, E_{b1}, of 2.66 GPa, following the material property of epoxy resin reported in [38]. At the same time, the mutual glue interaction without self-contact is also defined for the above two deformable bodies in the CONTACT TABLE. It is noted that, the SWEEP command, which is usually used to remove the coincident nodes, points, elements, etc., from the mesh, must be used in
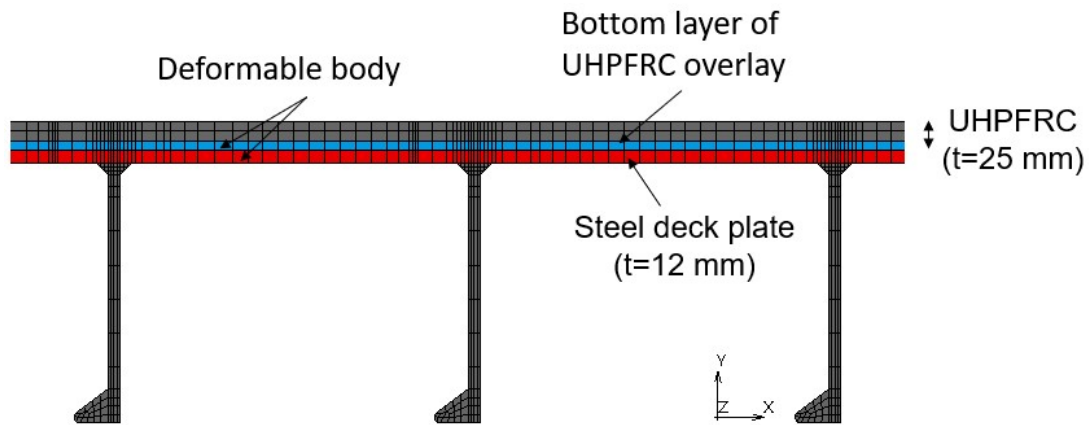
Figure 3.9 Deformable contact bodies in the modelling of UHPFRC/steel interface

separation for the UHPFRC layer and the steel members. If this step is neglected, the GLUE condition will be deactivated.

The main properties of steel material used in the analytical model, i.e., yield strength and maximum tensile strength, are listed in Table 3.2 for different members, following the CERI's experimental report. For UHPFRC, the Poisson's ratio and Young's modulus, E_u, of 0.22 and 31.3 GPa are used for the elastic state of UHPFRC in the analysis. The material properties of UHPFRC applied for material model in section 2.3.1 are listed in Table 3.3 according to the material pamphlet of J-THIFCOM (product name of UHPFRC) [31] and the in-site experiment of the cylinder specimens under uniaxial compression.

Table 3.2 Material properties of steel members

Member	Type	Yield strength, f_y (MPa)	Tensile strength, f_u (MPa)	Maximum tensile strain, ε_u
Steel deck plate	SM490YA	365	490	23%
Longitudinal bulb open rib	SM490YA	365	490	23%
Cross beam	SM400YA	245	400	22%

Table 3.3 Material properties of UHPFRC

Component	Point	Material properties		Values (unit)
Non-cracked component		Young's modulus	E_u	31300
		Poisson's ratio	v	0.22
Cracked component	1	Tensile initial cracking	σ_{cr}	6 (MPa)
			ε_{cr}	0.00019
	2	Tensile strength	σ_{t0}	9 (MPa)
			ε_{t0}	0.00175
	3	Ultimate tensile strain	ε_{tu}	0.01200
	4	Compressive strength	σ_{cu}	133 (MPa)
			ε_{cu}	0.0085
	5	End of softening stage in compression	$\sigma_{cs} = 0.2\sigma_{cu}$	
			$\varepsilon_{cs} = 1.5\ \varepsilon_{cu}$	

3.4 Static results and discussions

3.4.1 Displacement results

(a)   (b)
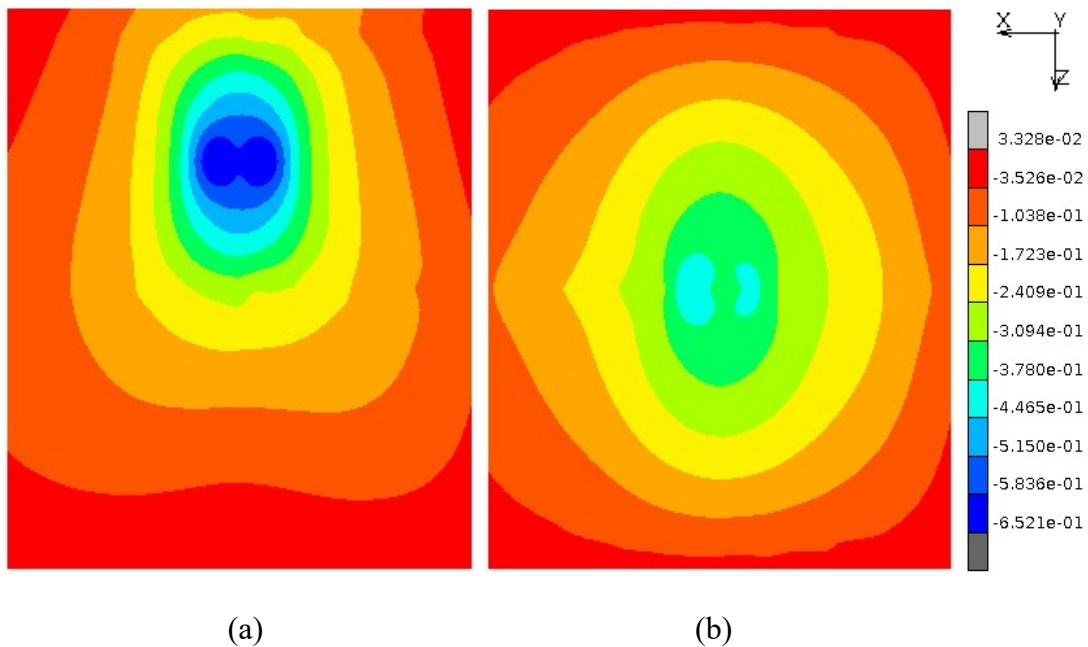
Figure 3.10 Vertical displacement distribution under bottom surface of steel deck plate from the model of composite bridge deck: (a) under Load East, (b) under Load Center.

Figure 3.10 shows the comparison between the vertical (or Y direction) displacement distributions under Load East and Load Center obtained under bottom surface of the steel deck plate from the model of the composite bridge deck. It is clearly seen that the values of vertical displacement obtained from the model under Load Center are much smaller than those from the one under Load East due to the stiffening effect of the middle crossbeam. The maximum deflection in steel deck plate occurs under Load East (or West) condition.

The vertical displacement distributions along paths WE and SN (see Figure 3.1(a)) under Load East are obtained from the static analysis comparatively to the experimental results, as represented in Figures 3.11 and 3.12, respectively. The analytical results from the model applying the uniformly distribution of wheel load [12] are also included for comparison. It is clearly observed that the displacement results from the current model show an improved agreement than those from the previous one in [12] for both the models
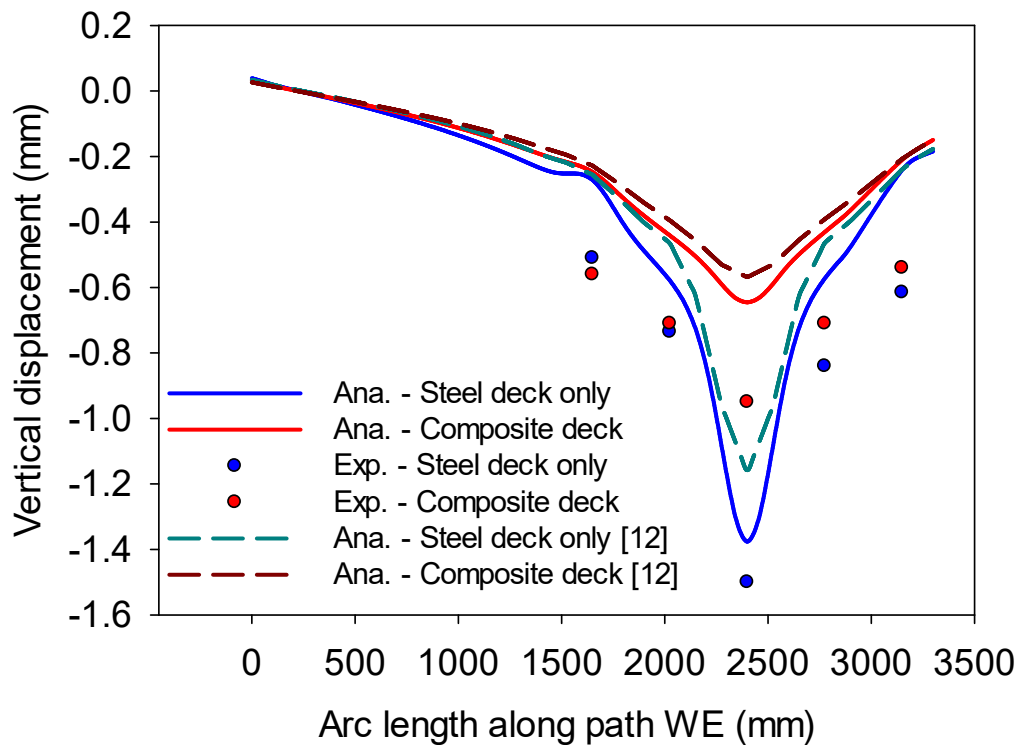
Figure 3.11 Vertical displacement distribution along path WE under Load East
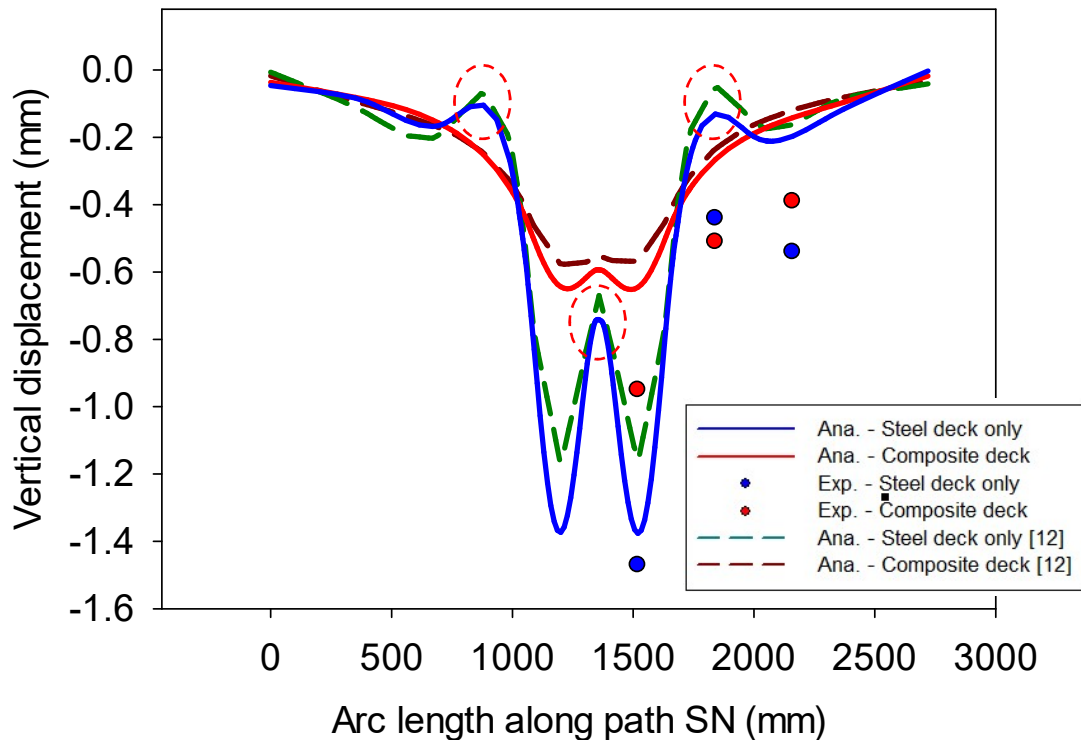
Figure 3.12 Vertical displacement distribution along path SN under Load East

with and without UHPFRC overlay. This can be attributed to the applying of non-uniformly distributed load for wheel truck tires. Due to the concentration of the contact pressure at the middle line of the tire patch in the transverse direction (see Figure 3.7(a)), more positive bending is obtained right under the tire contact region leading to the increases in vertical displacement. This improvement in reproducing the deflection results also demonstrates that the analysis has been getting closer to the actual condition of the deck slab after considering the non-uniformly distributed load for the truck tires.

In Figure 3.12, it is known that, under the applied wheel load at East load patch, the overall downward movement of the steel deck plate is obtained, which induces the positive bending at the tire contact region. On the other hand, due to the stiffening effect of the longitudinal rib 3,4 and 5 (see Figure 3.1(a)), the negative bending at these local regions is produced by the wheel load, as can be seen from the red dash cycled regions in Figure 3.12. It is obviously seen that, by applying the UHPFRC reinforcing overlay, both the global deformation under wheel load contact region and the local deformation above

the longitudinal ribs significantly decreased in comparison to the steel bridge deck without the strengthening layer.

From Figures 3.11 and 3.12, it can be seen that there are rather large differences between the analytical curves and the experimental data points. Because, in the experiment, the two main girders were supported by the other steel girders placed on the concrete floor, while the LVDT measurements under the steel deck plate are placed on the separate girder at the middle of two main girders, as illustrated in Figure 3.13. Due to force transferring from the bridge deck under static wheel load, the supporting steel beams under the main girders deformed in the vertical direction, along with the gap displacement decrease in the supporting apparatus. In contrast, the supporting girder under the LVDT sensors is not affected by the wheel load. This leads to the overestimation of the experimental displacement data in the steel deck plate.

From the current analysis, the stiffening effect of the UHPFRC overlay on the OSD structure is confirmed. It is found that, under Load East condition, the maximum value of deflection in the steel deck plate is considerably decreased from 1.37 mm to 0.64 mm (approximately 53%) after applying the UHPFRC reinforcing layer due to the increase in the overall stiffness of the orthotropic steel bridge deck.
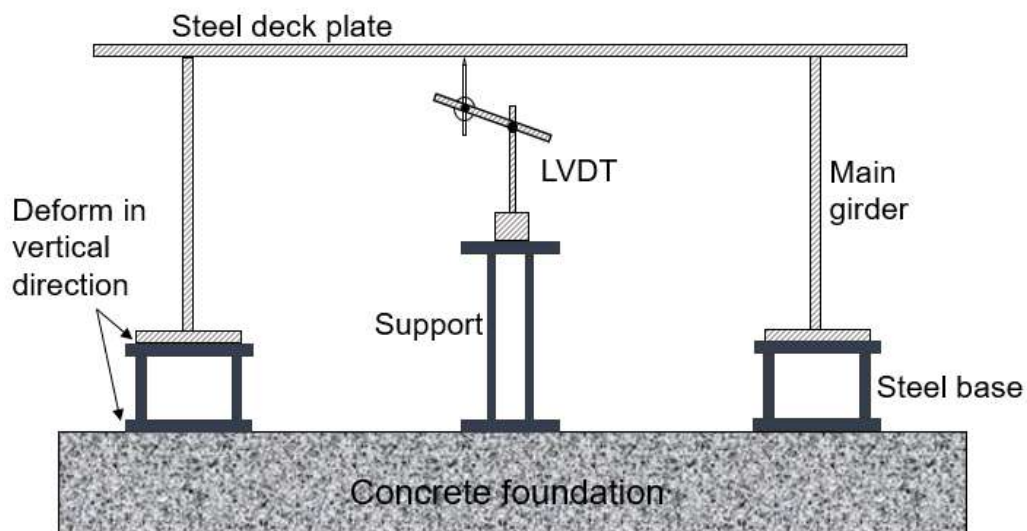
Figure 3.13 Setup of LVDT measurements under the steel deck plate in the experiments

3.4.2 Strain results in steel deck plate

The strain distributions in transverse and longitudinal directions under bottom surface of steel deck plate are shown in Figure 3.14 and 3.15, respectively, for the cases of the composite deck under Load Center and Load East. Similar to the displacement results,

| (a) | (b) |

Figure 3.14 Transverse strain distribution under bottom surface of steel deck plate from the model of composite bridge deck: (a) under Load East, (b) under Load Center.

Figure 3.15 Longitudinal strain distribution under bottom surface of steel deck plate from the model of composite bridge deck: (a) under Load East, (b) under Load Center.

the smaller values of analytical strain data are obtained from the model under Load Center due to the existence of the middle cross beam. Under Load East condition, the transverse strain levels are much higher than those in longitudinal direction. This is attributed to the stiffening effect of the longitudinal ribs distributed along the transverse side of the bridge deck, causing the constraints on the deformation of steel bridge deck in longitudinal direction. Therefore, the strain results in transverse direction obtained in the steel deck plate under Load East are focused on in this section.

Figure 3.16 shows the comparison of the experimental data and the analytical strain range distributions in the transverse direction along path SN under load East. The strain range levels that give a good agreement to experimental data points, are obtained in the present study for the region along path SN (as shown in Figure 3.1(a)) between the longitudinal Ribs 3 and 5. It is obvious that the strain ranges are significantly reduced after applying the UHPFRC overlay. The reduction percentage of maximum strain range levels is found to be about 83% (from -921.4μ to -160.9μ) from the current static analysis of OSD with the UHPFRC strengthening layer.
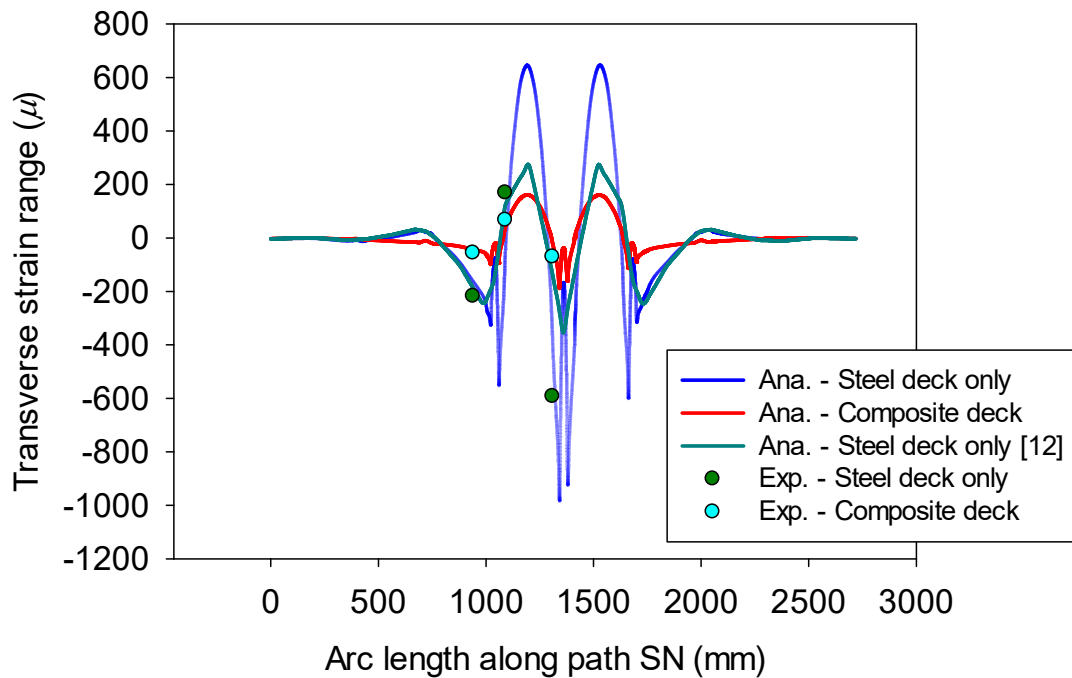
Figure 3.16 Distributions of transverse strain range along path SN under Load East

From the strain results in steel deck plate, it is also known that there are three factors for the enhancement of the numerical accuracy of the FEM model. The first is the using of the mesh refinement along regions above the Ribs 3, 4 and 5 (see Figure 3.3(a)). To capture the large negative bending generated at local regions of longitudinal stiffeners, it is worth mentioning that the fine mesh in the transverse direction is necessary. Therefore, the transversal mesh size of 2.5 mm is used at the vicinity of the middle axes of longitudinal ribs in the present FEM model. Moreover, in terms of the areas which are close to the ribs, as the local strains are highly sensitive to the rib's geometries, it is demonstrated by a group of analyses with or without modeling the weld areas as well as modeling the rib with 4-node thick shell elements or 8-node solid elements that the modeling of the actual geometry of the longitudinal stiffeners and the weld areas is an important factor for an accurate prediction and reproduction of the experimental steel strains of the gauge SEL1 near the middle point of path SN, even if a refined mesh is employed.
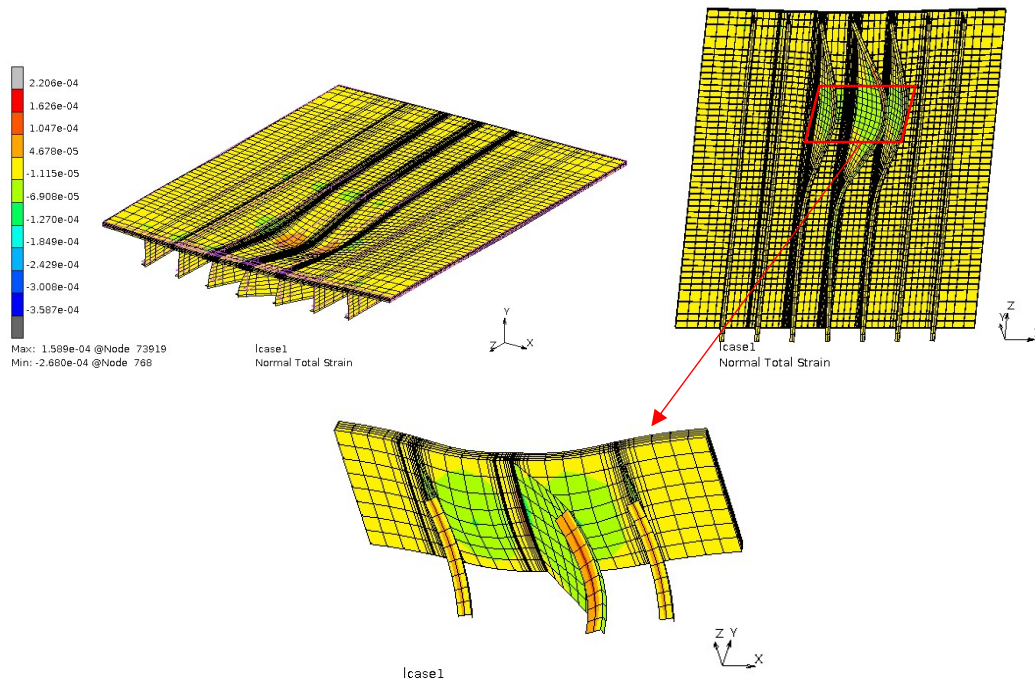
Figure 3.17 Vertical strain distribution and deformed shape of steel bridge deck under load West from the modeling of the ribs using 4-node thick shell elements (magnifying factor: 350)

45

Figure 3.17 shows the vertical strain distribution and deformed shape of the steel bridge deck under load West from the analysis using 4-node thick shell elements for modeling the ribs. Along with the global vertical deformation of steel bridge deck, the three middle ribs 3,4 and 5 are bent about the Y-axis at the opposite side of the bulb shapes in ribs. It can be seen that the perpendicular condition between the ribs and steel deck plate is not ensured. This may lead to the underestimation of strain results at the local region of longitudinal ribs, caused by the over-bending of the web of the ribs under wheel load. Hence, for OSD, it is recommended that the 8-node solid element should be used instead of 4-node thick shell element for modeling the longitudinal ribs under the critical region of applied wheel load, i.e., Ribs 3, 4 and 5.
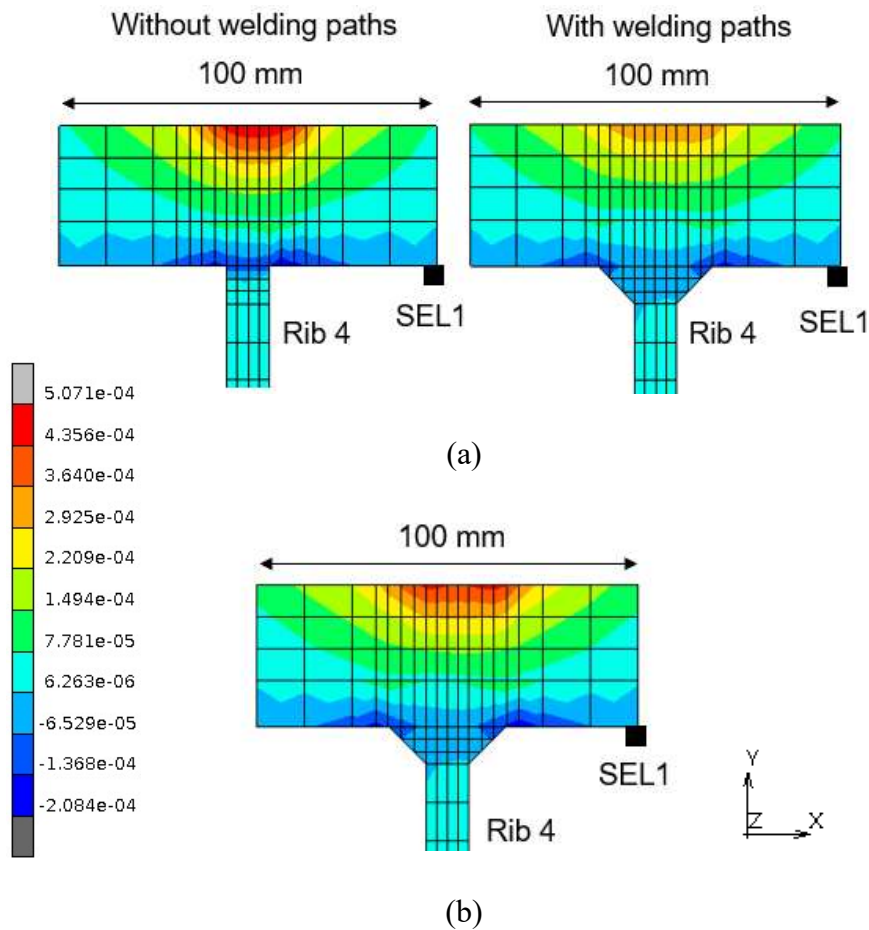
Figure 3.18 Transverse strain distributions above region of middle stiffener (Rib 4) at SN cross-section: (a) under uniformly distributed load, (b) under non-uniformly distributed load.

The transverse strain distributions for different geometric conditions are shown in Figure 3.18(a). It can be observed that the stiffness of the steel bridge deck is enhanced with the existence of weld paths, causing the decreases in strain levels in the steel plate and on the top surface of UHPFRC. The locations of peak values of strain level in the steel deck move toward the strain gauge positions from the edge of longitudinal ribs to the weld toes. This leads to the decrease in transverse strains at the nodes where the strain gauges are located.

The third factor which influences the strain results is the shape of the applied distributed load on the tire contact patch, either uniformly or non-uniformly. Following the non-uniformly distributed load in Figure 3.7(a) and due to a load concentrating to the centerline of tire contact patch in the transverse direction, the transverse strain levels increase for both steel plate and UHPFRC layer, as shown in Figure 3.18(b). As a result, a better accuracy from the FEM model is then achieved, especially at point SEL1, as the analytical strain data approach the experimental values. Therefore, for a better estimation of critical responses in steel plate, it is suggested that the non-uniformly distribution of the wheel load on contact patch applied from the automobile field should be used for both static and fatigue analyses of OSD instead of the idealized model using the uniformly-distributed wheel load which is specified by the standard design, since the contact stresses caused by wheel rubber tire in reality concentrates to the centerline of tire contact patch in both longitudinal and transverse directions.

3.4.3 Strain results in UHPFRC overlay

Figures 3.19 and 3.20 present the strain distributions in transverse and longitudinal directions, respectively, on the top surface of UHPFRC overlay in the composite deck under Load Center and Load East. It is found that the obtained strain behaviors are similar to those of vertical displacement and strain in steel deck place, in which the maximum strain levels occur at the path SN under Load East in transverse direction.

The maximum principal strain distributions on the top surface of UHPFRC are shown in Figure 3.21 in comparison between the cases under Load East and Load Center. The cracked regions in UHPFRC are represented by the gray color. Owing to the

strengthening effect of the longitudinal ribs, the negative bending is induced by the wheel load at the local regions above the ribs, especially at the Rib 4 (middle rib). Therefore,

(a)   (b)
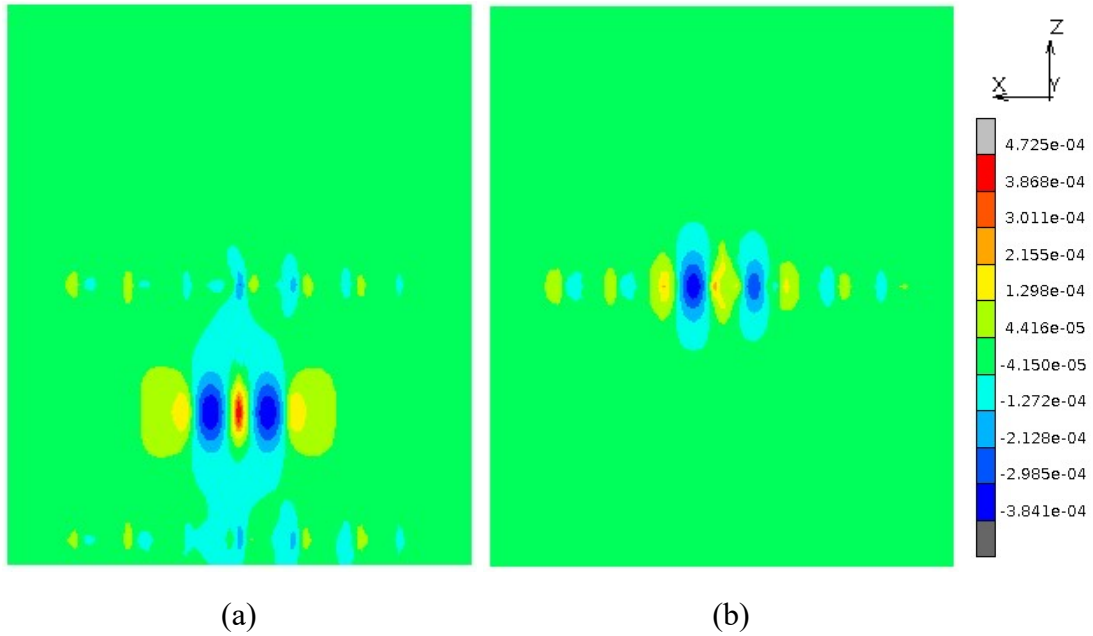
Figure 3.19 Transverse strain distribution on the top surface of UHPFRC from the model of the composite bridge deck: (a) under Load East, (b) under Load Center.

(a)   (b)

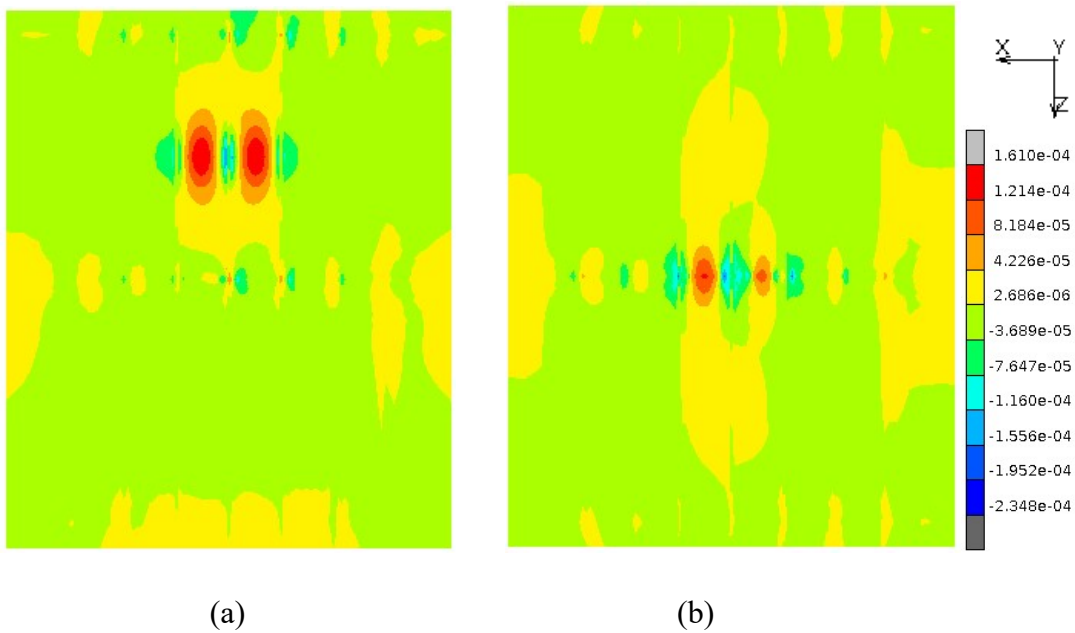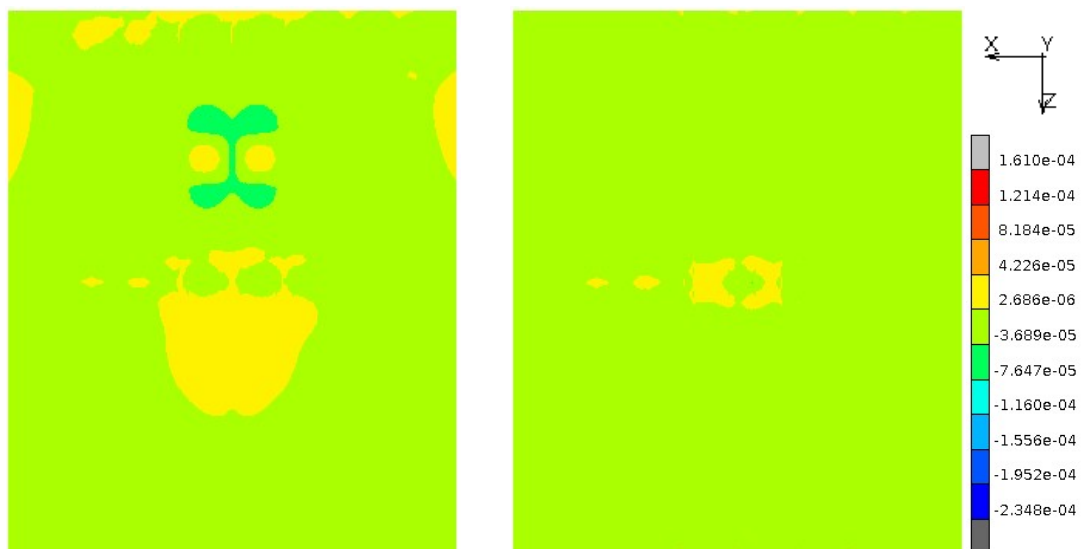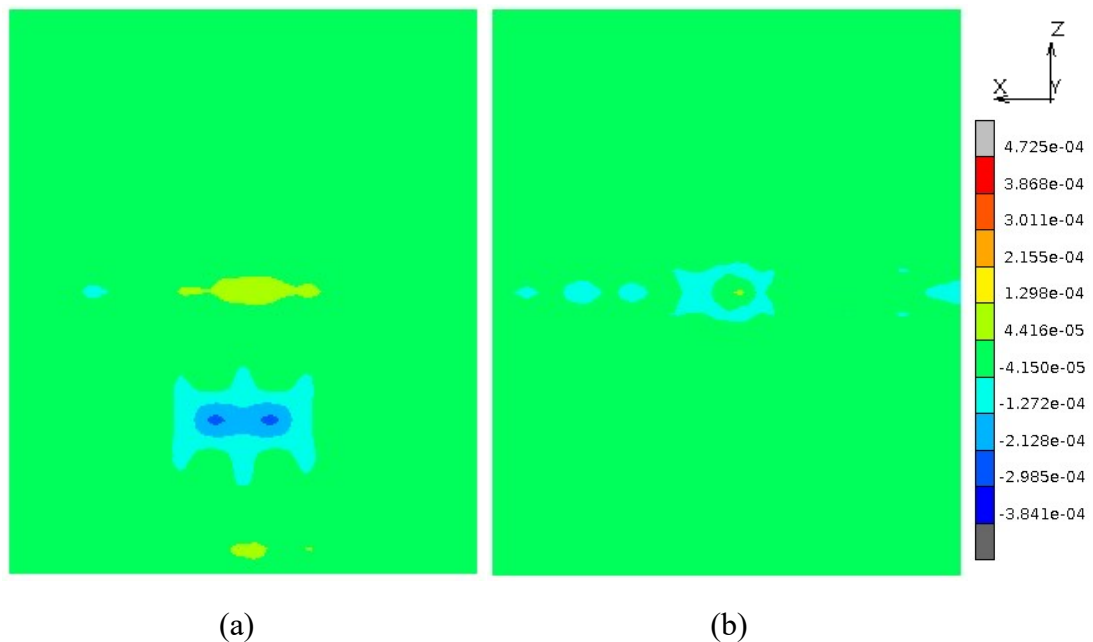Figure 3.20 Longitudinal strain distribution on the top surface of UHPFRC from the model of the composite bridge deck: (a) under Load East, (b) under Load Center.
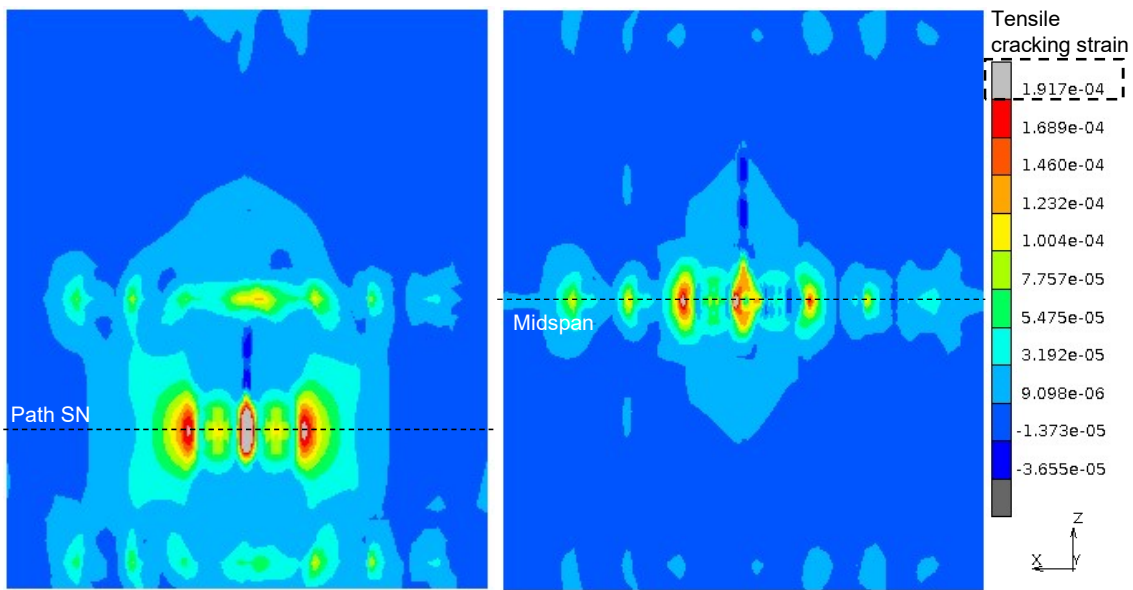
Figure 3.21 Maximum principal strain distribution on the top surface of UHPFRC from the model of the composite bridge deck: (a) under Load East, (b) under Load Center.
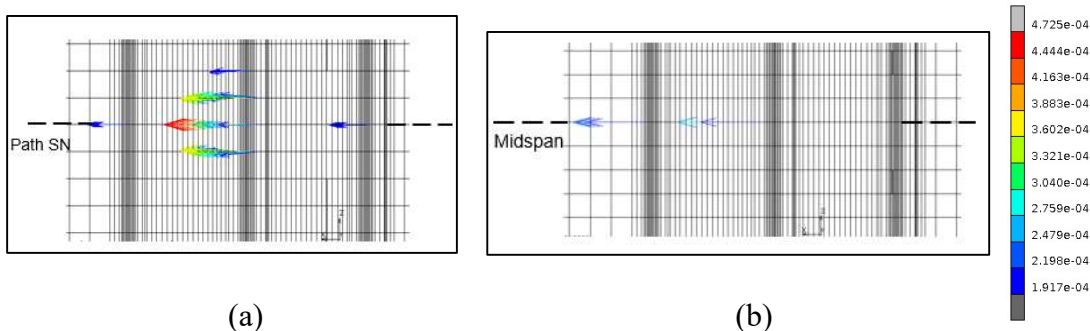
Figure 3.22 Direction of the maximum principal strain on the top surface of UHPFRC obtained from the cracked elements: (a) under Load East, (b) under Load Center.

under Load East, the tensile cracks occur at the local regions above the Ribs 3, 4 and 5, as shown in Figure 3.21(a). Under Load Center, the local transverse bending above the ribs is constrained by the existence of the middle cross beam, leading to the narrower cracked regions observed on the top surface of the UHPFRC layer. The directions of the maximum principal strain on the top surface of UHPFRC obtained from the cracked elements are represented in Figure 3.22. It is known that the directions of maximum principal strains from the cracked elements are mainly in transverse direction. This means that the UHPFRC cracks are distributed in longitudinal direction along the ribs.

Figure 3.23 present the cracked region obtained from the three layers of UHPFRC overlay from top to bottom under Load East condition. Since the maximum negative bending is obtained above the local region of middle rib (Rib 4), the largest cracked regions are found at this rib for the top and middle layer in UHPFRC overlay. Despite the positive bending is produced under contact regions of rubber tire lead by the overall deformation in vertical direction of the bridge deck, the tensile crack does not occur in the bottom layer of UHPFRC under the current wheel load level of 100 kN, thanks to the high cracking strength of this material.
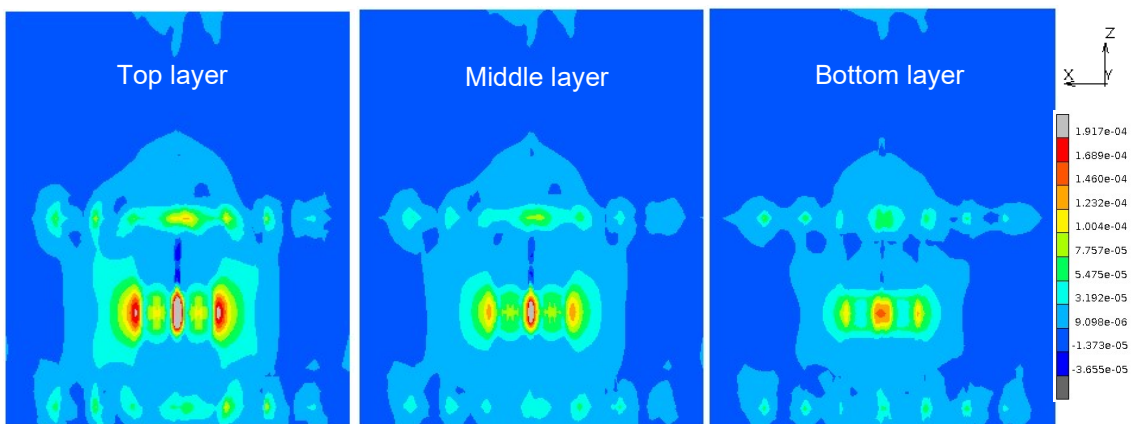
Figure 3.23 Maximum principal strain distribution under Load East for different layers of the UHPFRC overlay

3.5 Summary

In this chapter, a non-linear 3D FEM model was performed to investigate the static behaviors of the orthotropic steel bridge deck strengthened by the UHPFRC overlay under a wheel loading with rubber tire.

The stiffening effect of the UHPFRC overlay on the steel bridge deck was examined numerically. It was found that the maximum value of the deflection and the strain level in the steel deck plate were reduced approximately by 53% and 83%, respectively, after applying UHPFRC layer in the current model.

Strain behaviors in UHPFRC overlay were also investigated in the static analysis. It was indicated that the cracked elements were distributed in longitudinal direction on the

local regions above the longitudinal ribs, i.e., Ribs 3, 4, and 5, where the large negative bending moments are obtained.

A group of factors for getting closer to the real conditions of the composite deck, e.g., the actual geometry of the longitudinal ribs, the welding area, the non-uniformly distributed load, were investigated in a series of FE analyses under the static condition of the wheel-tire load. It was found that the accuracy of the numerical prediction was considerably improved after including those factors in the analytical model, especially for the strains of steel deck plate. Consequently, the FE calculation that was not only accurate but also efficient was obtained, and the chosen model in the static analysis is appropriate for proceeding to the fatigue analysis of the composite deck.

CHAPTER 4 FATIGUE ANALYSIS OF THE UHPFRC-STEEL COMPOSITE BRIGDE DECK SUBJECTED TO A MOVING WHEEL LOADING WITH RUBBER TIRE UNDER DRY CONDITION

4.1 Introduction

In this chapter, fatigue performances of the composite bridge deck in stage 1 (section 3.2.2) subjected to a moving wheel loading with rubber tire under dry condition (see Figure 4.1) are investigated and assessed by a fatigue analysis based on the appropriate model chosen from the static analysis. The mesh pattern and boundary conditions from FEM model of the composite bridge deck under a moving wheel tire loading in fatigue analysis are the same as those from static analysis, as shown in Figure 4.2. Continuing with the point of view of trying to approach the real conditions of the fatigue experiment of the UHPFRC-OSD composite structure, the numerical method considering the bridging stress degradation of cracked UHPFRC and the interfacial degradation scenarios with the different phases is proposed in the first stage of fatigue analysis. Throughout the analysis process, the assumed scenarios for the degradation at the UHPFRC/steel interface are evaluated by examining the fatigue behaviors, i.e., strain in steel deck plate and UHPFRC crack propagation, for each degradation phase.

Figure 4.1 Fatigue test of full-scale UHPFRC-steel composite bridge deck in stage 1 subjected to a moving wheel loading with rubber tire under dry condition. [9]
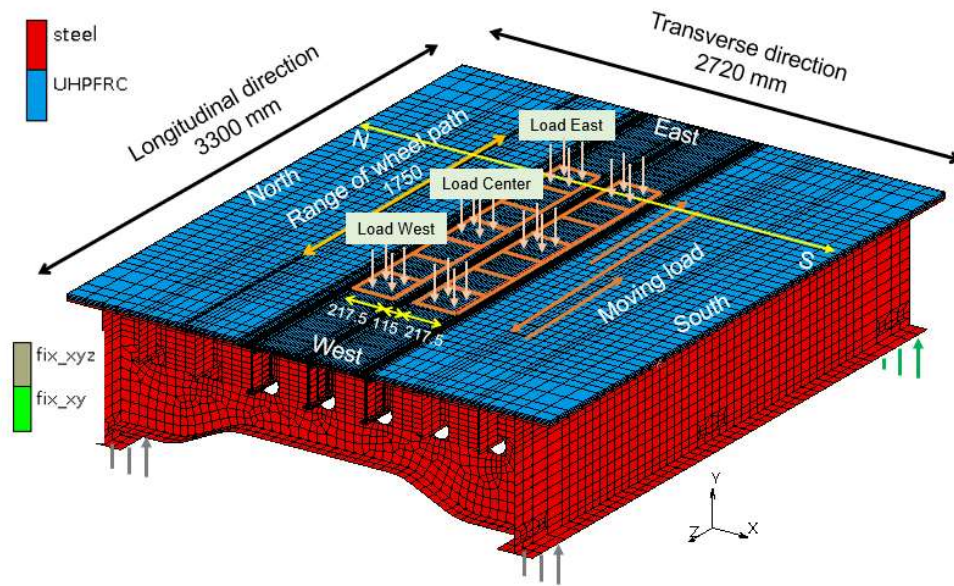
Figure 4.2 Boundary conditions from the FEM model of UHPFRC-steel composite deck under a moving wheel loading with rubber tire.

4.2 Procedure of fatigue analysis subjected to moving wheel loading with rubber tire

For one cycle of fatigue analysis, the wheel load with rubber tire is firstly applied at the center load patch (load case 1). Load case 1 from fatigue analysis is same as Load Center in static analysis. After reaching the peak of 100 kN from zero, these elements are unloaded at the same time with the starting of the loading process at the adjacent load patch (load case 2) with an equal augmented rate, as represented in Figure 4.3. The data of the maximum strain levels in both tension and compression, and the cracking state at each node of 3D smeared crack elements in UHPFRC reinforced overlay are updated and recorded along with the modification of the shear retention factor in Equation (2.14) during the loading process. Subsequently, for the unloading process at each load patch, the nodal strain history is read and applied to the hysteresis constitutive model of UHPFRC. Applying this procedure along the load sequence, one cycle of fatigue analysis including a total of 13 load cases is finally completed at the center patch position again.

For the following cycle of fatigue analysis, the historic maximum tensile strains are applied in the bridging stress degradation equation (Equation (2.20)) coded in the user subroutine. In stage 1, the bridging stress degradation relation under dry condition is applied in fatigue analysis as follows

$$\frac{\sigma_N}{\sigma_1} = 1 - (0.015 + 5\varepsilon_{t\max})\log(N)$$

(4.1)

$$\text{for } 1 \le N \le 1,100,000$$

where ε_{tmax} is maximum tensile strain

N is number of loading cycles

σ_N/σ_1 is bridging stress degradation ratio between the N_{th} and the first cycles.

The tensile strength of UHPFRC is then modified that causes the decrease in stiffness and appearance of new cracks in the strengthening overlay. Simultaneously, the UHPFRC/steel interfacial condition of fatigue analysis is modified based on the method in section 2.4. The procedure is continued until the number of cycles reaches 1,100,000 when the experiment of the composite bridge deck under moving wheel loading with rubber tire completes. For the first stage, the number of loading cycles used in the test is determined based on the design traffic volume of the reference route. The bridges on the reference route are expected to support the two-wheel legal axle load of 100 kN. The impact coefficient of 1.4 for floor system is then multiplied to the required load, giving a load of 70 kN for each wheel. For the bridge lifetime design of 100 years, the number of loading cycles is estimated to be 3,200,000 wheel loading cycles. However, based on the capability of the testing machine, the fatigue test is performed with a single-wheel load of 100 kN. For this wheel load level, the estimated number of 1,100,000 loading cycles can give a load that is equivalent to the 100-year design traffic load [9].
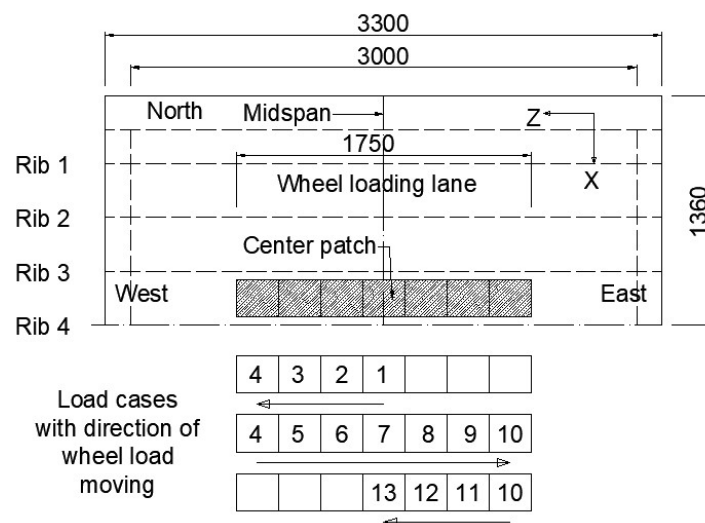
Figure 4.3 Load cases in accordance with the direction of the wheel load moving

4.3 Scenarios with the different phases of the interfacial bond degradation for the fatigue analysis

As mentioned in section 2.4, under fatigue loading, the degradation of bond behavior between UHPFRC and steel plate is assumed to be governed by the interfacial bond stiffness degradation. Based on the experimental observations of the composite deck, e.g., strain results in steel deck plate and abnormal noise range in deck plate from hammer tapping test, the interface delamination may occur from the 700,000th loading cycles under the moving wheel load region. Consequently, the degradation in shear component of the interfacial bond behavior between UHPFRC and steel deck is divided into two phases, as represented in the following sub-sections.

4.3.1 Phase of the interfacial bond stiffness degradation from the beginning to 700,000th cycles (phase 1)

The degradation in the shear component of the interfacial bond stiffness is simply assumed by a function of the number of cycles N in the analysis as follows

$$\frac{E_{bN}}{E_{b1}} = f(N)$$

$$\frac{E_{bN}}{E_{b1}} = 1 - 0.1707 \times \log N \tag{4.2}$$

where E_{bN} and E_{b1} are the interfacial bond stiffness of the Nth and the first cycles, respectively.

$b_0 = 0.1707$ is the slope of the bond stiffness degradation line.

The interfacial bond stiffness at each loading cycle is computed following Equation (4.2) with the constant value of degradation slope b_0 during phase 1 of the first stage in fatigue analysis, from the assumption that the bond stiffness approaches zero value at the 700,000th loading cycle representing the interface debonding. This assumption comes from the significant increases in experimental strain range levels at the strain gauges SEL1, SEL2 and SEL3 in the steel deck plate (see Figure 3.1(a)) for both transverse and longitudinal directions as well as the results of the non-destructive inspection throughout the experiment, i.e., hammer tapping test. As illustrated by the red line in the Figure 4.4(b), the abnormal noise region in the deck plate has taken place from the 760,000th loading

(a) Phase 1   (b) Phase 2
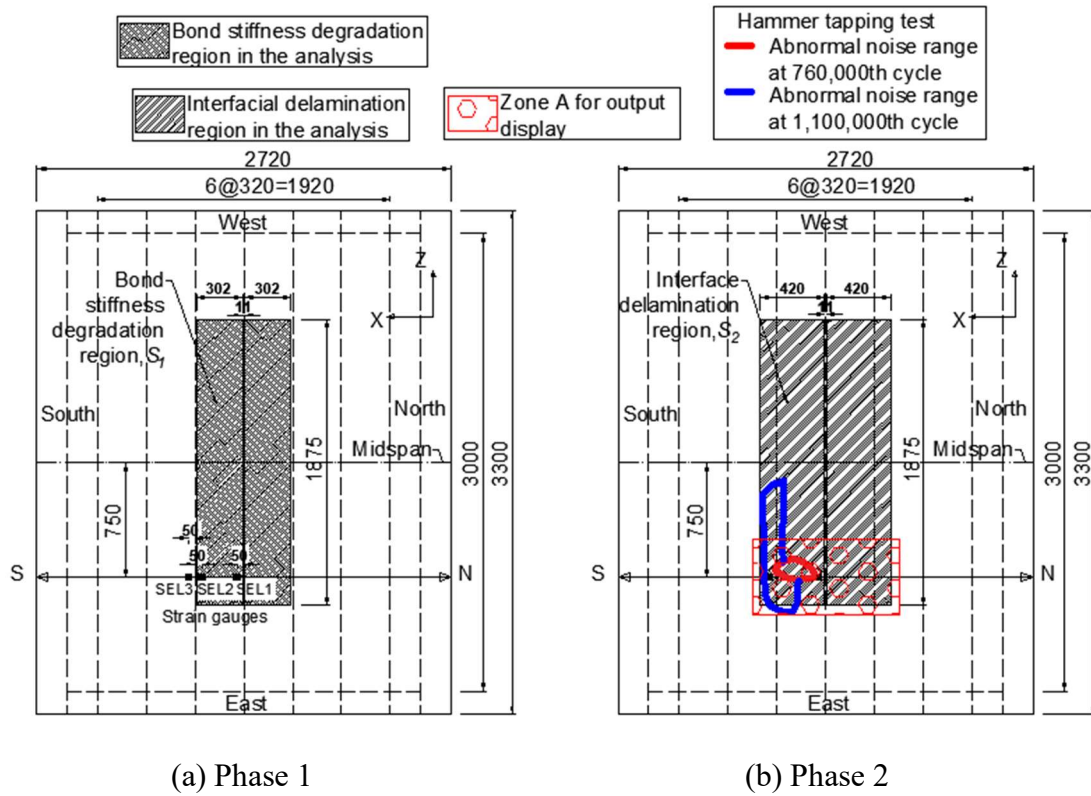
Figure 4.4 Scheme of degradation phases of the interface bond layer in the analysis

cycle. It is noted that the interfacial delamination could be typically detected by the acoustic hammer through the abnormal noise, i.e., the lower frequency sound, after the void between UHPFRC overlay and steel plate formed.

It is known in the analysis that due to the high contact shear stress induced by the wheel load (as illustrated in Figure 4.5), the region below the tire contact patch is susceptible to the fatigue action of the load moving, which may lead to the interfacial delamination at this region, i.e., the dark region under UHPFRC layer as seen in Figure 4.6. The picture of bottom surface of the removed UHPFRC overlay shown in Figure 4.6 is taken at the end of stage 3 from the fatigue test of the composite bridge deck. It is also noticed that the dark region in Figure 4.6 is composed of the iron oxide particles caused by the surface treatment process using shot-blasting before UHPFRC was overlaid on the steel plate.

In phase 1 of fatigue analysis for stage 1, as shown in Figure 4.4(a), the region of bond stiffness degradation applying Equation (4.2) which is slightly larger than the tire contact patch area, is adjusted and determined as S_1 = 2×302 (transverse) × 1875 mm

(longitudinal) for matching the experimental tendencies at strain gauges SEL1, SEL2 and SEL3 in steel deck plate. The middle gap of 11 mm is applied above longitudinal Rib 4 for the degradation area S_1. The reason is that the contact shear stresses are nearly zero in the region above the middle stiffener (Rib 4), as shown in Figure 4.5. The existence of the middle gap of the bond stiffness degradation can also be confirmed in Figure 4.6.
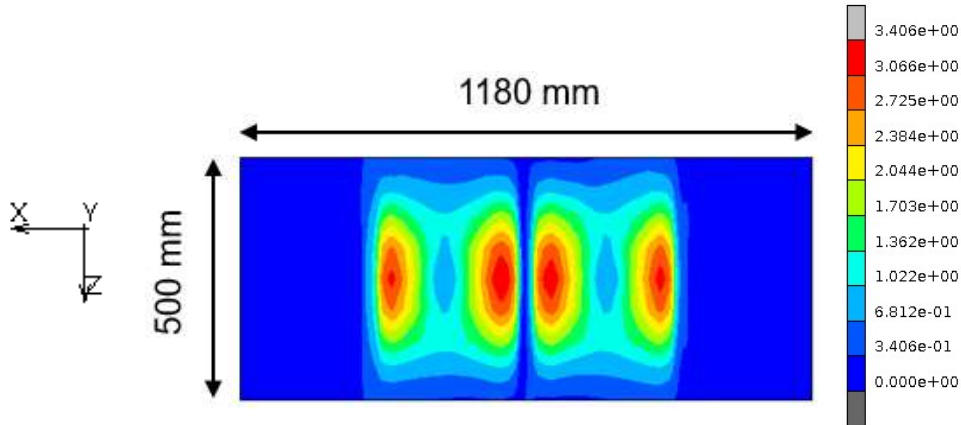
Figure 4.5 Contact shear stress at UHPFRC/steel interface from the first cycle
(displayed at zone A in Figure 4.4(b))

Figure 4.6 Interfacial bond layer under bottom surface of removed UHPFRC overlay at the end of stage 3 from fatigue test.

4.3.2 Phase of the expansion of interface delamination area from the 700,000th to 1,100,000th cycles (phase 2)

In phase 2 of stage 1 from fatigue analysis, a partial slip response applied to the UHPFRC/steel interface is transformed into a total slip regime representing the interfacial debonding. For this phase, the fatigue damage of the interface bond layer is simply governed by the expansion of the debonded area S_1. Also based on the results from hammer test and the strain behaviors in steel plate, the delamination area is gradually expanded in transverse direction from area S_1 (at the 700,000th cycle) to area S_2 (at the 1,100,000th cycle). For this phase, the progressive expansion of the interfacial delamination area is modeled in the analysis as follows

- From the 700,000th to 940,000th: the constant speed of 33.5 mm per 100,000 cycles is applied to the transverse expansion of debonding area.

- From the 940,000th to 1,100,000th: the slower speed of delamination area expansion is applied in the analysis, which is equal to 23.5 mm per 100,000 cycles.

The average speed of the progressive expansion in the transverse direction of the interfacial delamination area from 700,000th to 1,100,000th is then calculated as 29.5 mm per 100,000 load cycles. At the 1,100,000th cycle, the interfacial delamination area is S_2 = 2×420 (transverse)×1875 mm (longitudinal) in the current model. This expansion speed of the debonding area is relatively compatible with the results from the hammer tapping test, as shown in Figure 4.4. From the 760,000th to 1,100,000th cycle, the expansion in transverse direction of the abnormal noise range in the hammer test is about 100 mm (or 29.41 mm per 100,000 cycle).

4.4 Results and discussions

4.4.1 Displacement results

Figure 4.7 shows the vertical displacement distribution under bottom of steel deck plate obtained from load case 10 for different cycles from the stage 1 of fatigue analysis. Load case 10 from stage 1 of the fatigue analysis is same as Load East in static analysis under the wheel loading with rubber tire. It is clearly seen from the figure that the

magnitude of displacement in steel bridge deck increases with the increase of the number of loading cycles. For phase 1 of the analysis from the first cycle to the 700,000th cycle, the displacement levels gradually increase owing to the continuous reduction of the bond shear stiffness at the UHPFRC/steel interface under the applied load region. After that, in phase 2, the considerable growth in deformation is obtained in the analysis caused by the

(a) At the first cycle   (b) At the 700,000th cycle

(c) At the 1,100,000th cycle
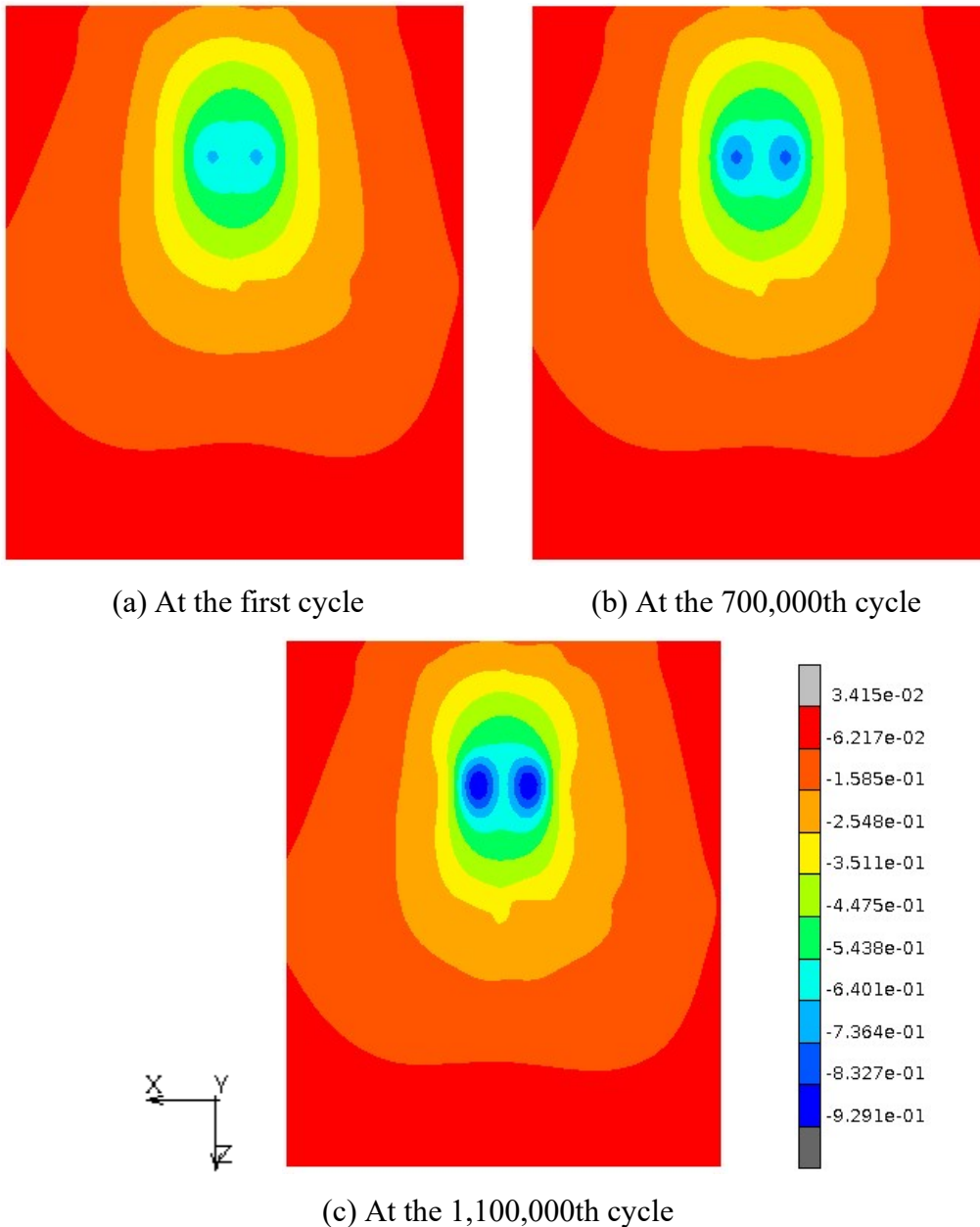
Figure 4.7 Vertical displacement distribution under bottom of the steel deck plate for different cycles from the stage 1 of fatigue analysis.
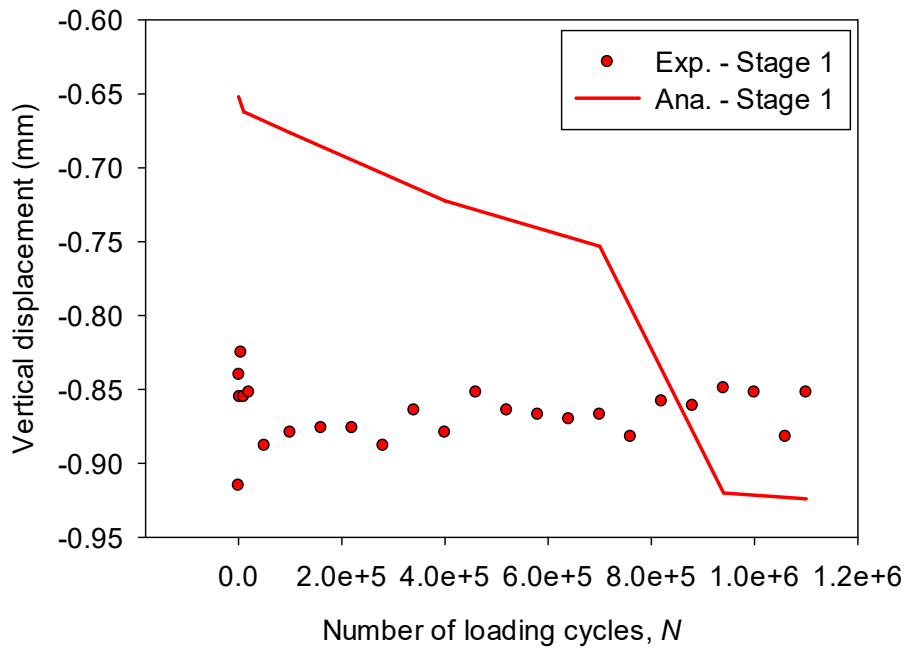
Figure 4.8 Maximum vertical displacement versus the number of loading cycles from stage 1 of fatigue analysis.

progressive loss in composite action between UHPFRC overlay and steel deck plate when the interfacial delamination region is expanded in transverse direction from area S_1 (see Figure 4.4). Figure 4.8 represents the relationships between the maximum magnitudes of vertical displacement obtained in the bridge deck under load case 10 in the analysis and the number of loading cycles. In Figure 4.8, the significant increase in analytical displacement results in phase 2 can be obviously seen after the gradual growth in phase 1. Since the movements between the supports under the LVDT measurement and the bridge deck are different as discussed in the previous chapter, the increase in vertical displacement caused by fatigue degradations in the composite bridge deck is not clearly observed from the experimental data.

4.4.2 Strain results in steel deck plate

The transverse strain distribution along the cross section SN of the steel plate and UHPFRC overlay are plotted versus the number of loading cycles in Figure 4.9. The compressive strain values are indicated by the band from the blue to red colors, while the tensile strain values are represented by only gray color. Due to the progressive reduction

in the shear component of interfacial bond stiffness on the region S_1, the transferred shear stress between two materials decreases with the number of cycles in phase 1. It is noted that the normal component of the bond layer also degrades along with the shear component due to the increase in bond slip displacement. For phase 2, along with the development of the interface delamination area, the capability of transferring shear force is totally lost on the region S_2 (see Figure 4.4) causing a significant increase in the

(a) At the first loading cycle

(b) At the 700,000th loading cycle

(c) At the 1,100,000th loading cycle
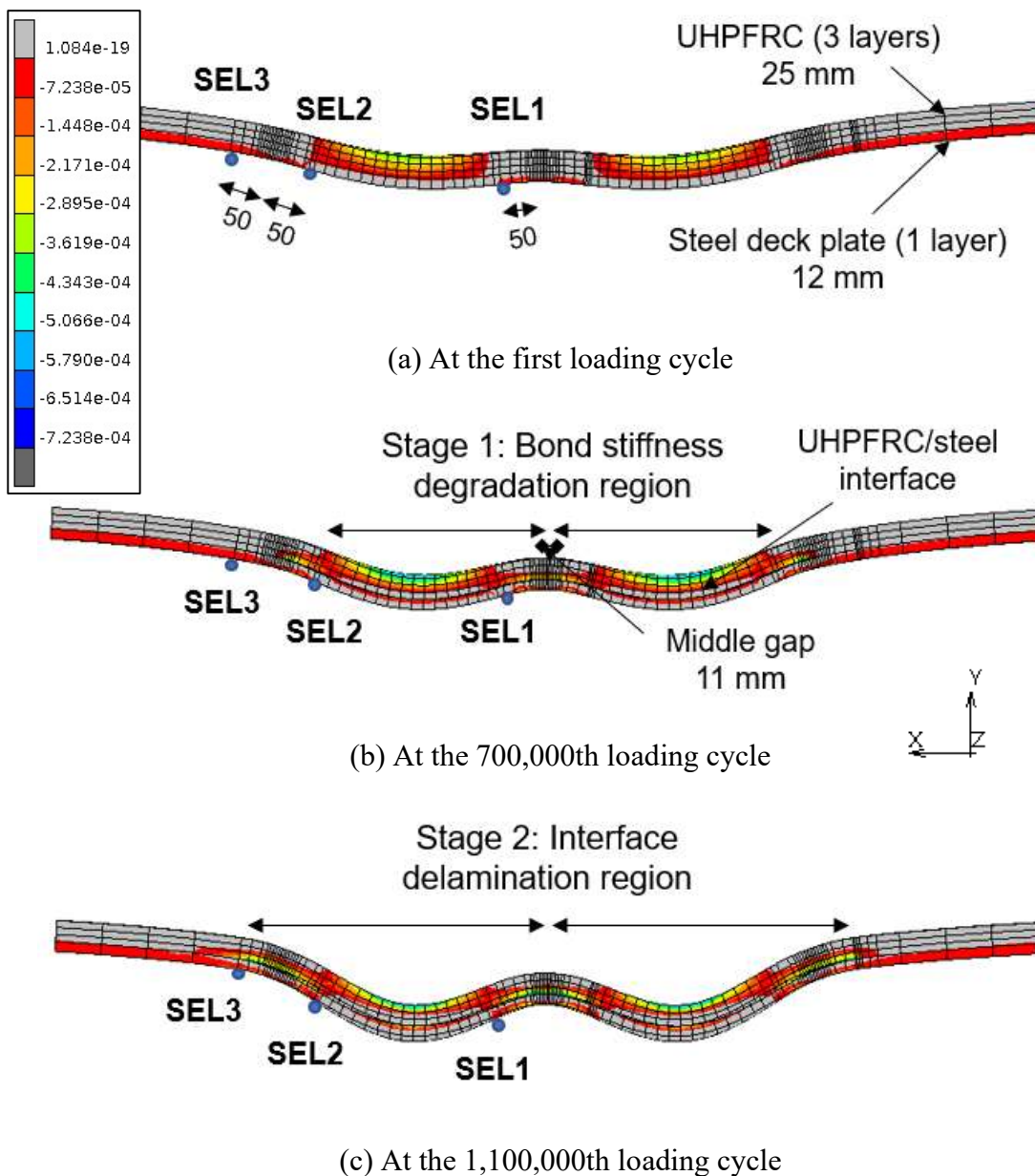
Figure 4.9 Transverse strain distribution along SN cross-section for each phase from stage 1 of fatigue analysis under load case 10 (deformed magnifying factor: 150)

deformation of the composite bridge deck.

From Figure 4.9, it can be seen that the UHPFRC overlay and the steel deck plate act as the double beam for both two phases. This leads to the occurrences of the tensile zones under the UHPFRC reinforced layer and the compressive zones on the top surface of the steel plate in the contact regions under the wheel rubber tire. The stress redistributions with the spreading of compressive zone from the wheel load area to the regions above the longitudinal Ribs 3, 4 and 5 are then observed as well. Consequently, the overall stiffness of the composite deck decreases with the increase of loading cycles resulting in the continuous deformation increases in both UHPFRC and steel deck plate subjected to moving wheel loading.

On the other hand, the decrease in stiffness of the composite deck is also caused by the degradation of the bridging stress of the cracked UHPFRC. Owing to the stress concentration at the crack tip lead by the reduction in the tensile strength after the crack initiates, the additional crack length is newly formed at the crack tip causing the propagation of the fatigue cracks in the reinforced overlay. Due to the continuous loss in composite action of the OSD strengthened by UHPFRC from phases 1 and 2, the progressive cracks caused by the bridging stress degradation induce the strain re-distributions along both the longitudinal and transverse directions in the steel bridge deck. The transverse strain distributions for each phase in the steel deck obtained from the East load patch under load case 10 are illustrated in Figure 4.10. It is obvious that the strain levels in steel deck plate are significantly increased in both compressive zones above the longitudinal stiffeners and the tensile zones under the contact area of the wheel path due to the decrease in overall stiffness. In phase 2, when the interface delamination area broadens across the regions above Ribs 3 and 5, the compressive zones at these regions are notably expanded in accordance with the direction of interfacial failure. It is also noticed that the loss in interfacial bond stiffness in phase 1 and the expansion of the debonding area in phase 2 under fatigue loading considerably accelerate the bridging stress degradation in UHPFRC which depends on the maximum tensile strain level, as shown in Equation (4.1).

(a) At the first loading cycle

(b) At the 700,000th loading cycle

(c) At the 1,100,000 loading cycle
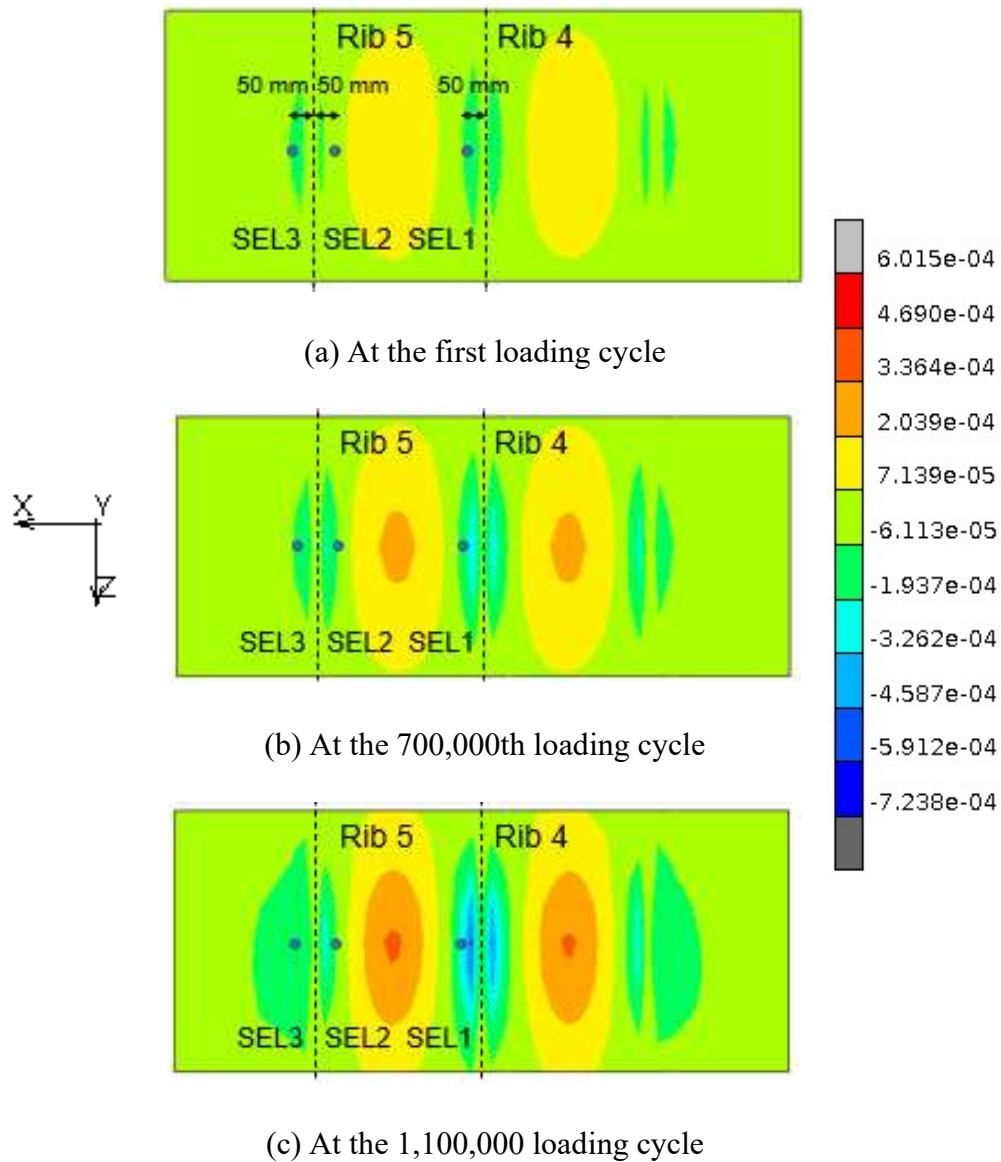
Figure 4.10 Transverse strain distribution in steel deck plate versus the number of loading cycles at zone A (shown in Figure 4.4(b)) under load case 10.

From Figures 4.11 to 4.13, the strain range evolutions in transverse and longitudinal directions under load case 10 obtained from the positions of the strain gauges SEL1, SEL2 and SEL3 are plotted comparatively with the data from the experiment. From the beginning to 1,100,000th loading cycles, the experimental strain levels continuously increase in the steel deck plate, except for the longitudinal strains at SEL1 and the transverse strains at SEL2. In Figure 4.11, it is obvious that the accuracy of the model for transverse strain at SEL1 is considerably increased due to the considering of factors mentioned in the static analysis, i.e., the actual geometry of the longitudinal
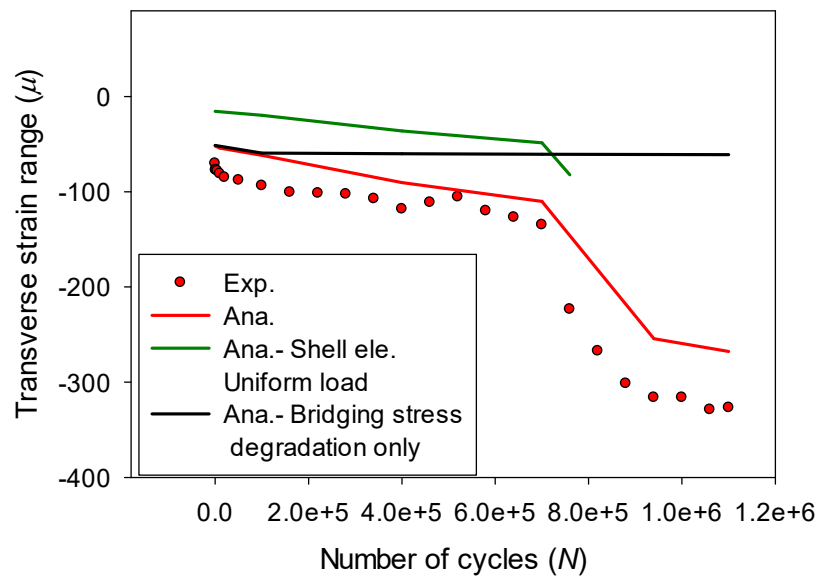
(a) Transverse strain range
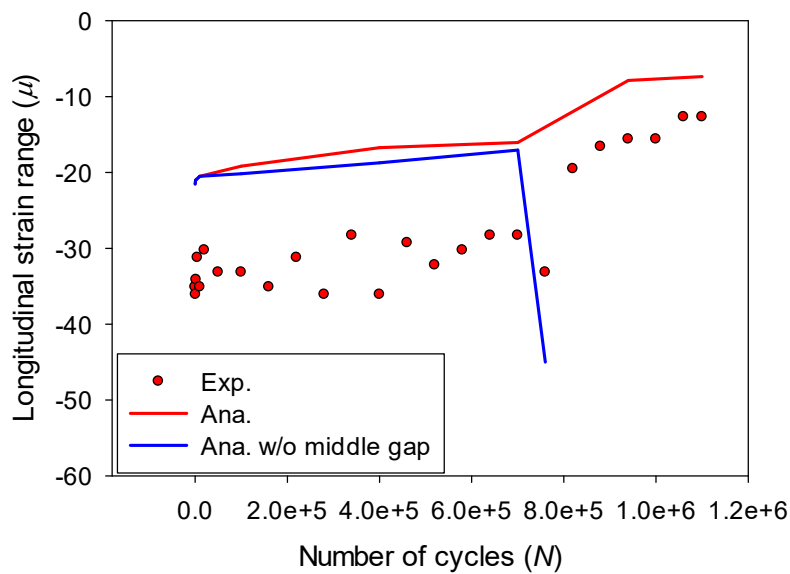
(b) Longitudinal strain range

Figure 4.11 Strain range versus the number of loading cycles at strain gauge SEL1 in steel deck plate

ribs, the welding area and the non-uniformly distributed load by rubber tire. With the existence of the gap of the bond stiffness degradation, the interfacial bond slip displacement in the longitudinal direction is constrained by the stiffer part (gap) leading to the decrease in longitudinal strain level at SEL1 (see Figure 4.11(b)). This gives a
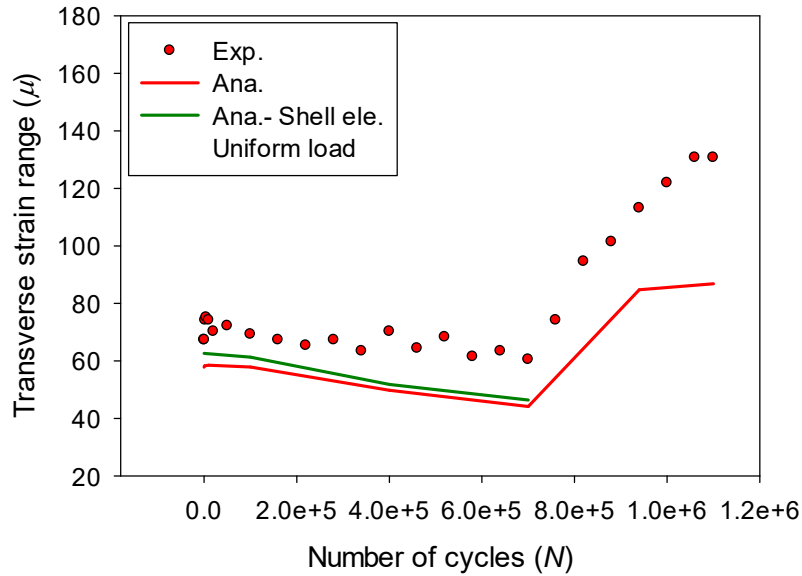
(a) Transverse strain range
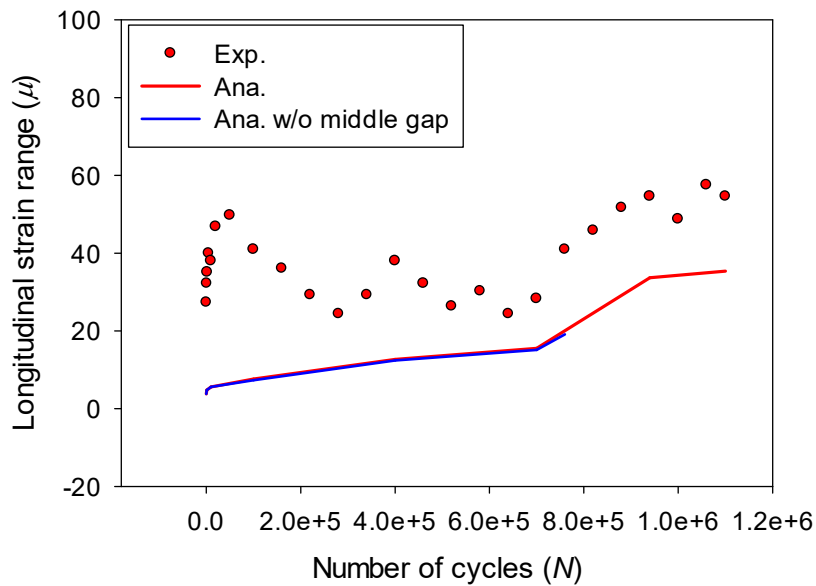
(b) Longitudinal strain range

Figure 4.12 Strain range versus the number of loading cycles at strain gauge SEL2 in steel deck plate

tendency agreement between the experimental and analytical strain results in the longitudinal direction for point SEL1. As the distances between the middle gap and points SEL2 or SEL3 are relatively large, the influences of this gap on the strain results at these two points are insignificant, as observed by Figures 4.12(b) and 4.13(b).
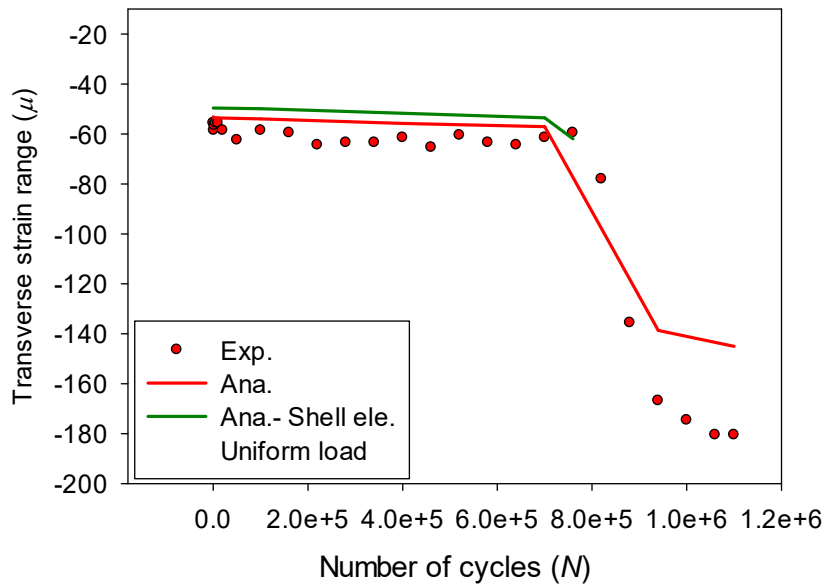
(a) Transverse strain range
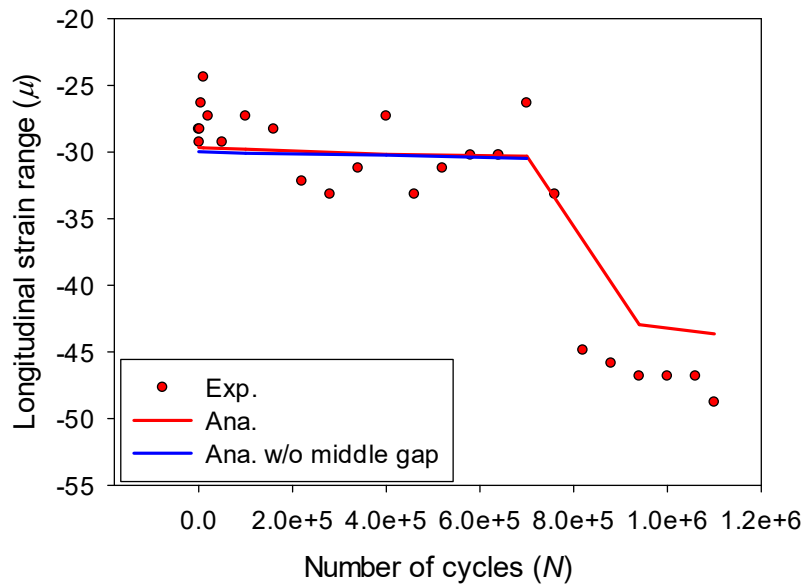
(b) Longitudinal strain range

Figure 4.13 Strain range versus the number of loading cycles at strain gauge SEL3 in steel deck plate

Comparing the models with and without the interfacial bond stiffness degradation, it is found that the effect of bond stiffness degradation on steel strains is predominant in the composite deck in comparison with that of bridging stress degradation in cracked

UHPFRC due to the high fatigue resistance of UHPFRC after cracking under dry condition, as represented by transverse strain results at strain gauges SEL1 in Figure 4.11(a).

For point SEL2, the transverse strain results may be influenced by the bond stiffness degradation at the two regions: one is above the longitudinal Rib 5, another is under the contact area of wheel load. To elucidate the effect of the interfacial delamination area at each mentioned region on the strain results in steel deck plate, the additional analysis is conducted considering the separate debonding areas, as shown in Figure 4.14. From this analysis, the transverse strain distributions in steel deck plate for different delamination areas are plotted at zone A under load case 10 in Figure 4.15. The gray color represents the regions with tensile values of transverse strain in steel plate. It is found that when the debonding area occurs at the longitudinal ribs (see Figures 4.15(b) and 4.15(d)), the stiffening effect of these ribs increase at these local regions due to the loss in composite action at interface, causing more negative bending is obtained. This leads to the increase in maximum transverse strain levels and the narrowing of the compressive regions at local regions above the ribs. The increasing tendency in transverse strain is then observed at point SEL2 when debonding area happens at Rib 5. Similarly, more positive bending is obtained at wheel load region when the delamination area is applied here (see Figure 4.15(c)), leading to the reduction in transverse strain at point SEL2. With the chosen of

(a) At Rib 4   (b) At wheel load region

(c) At Ribs 3 and 5
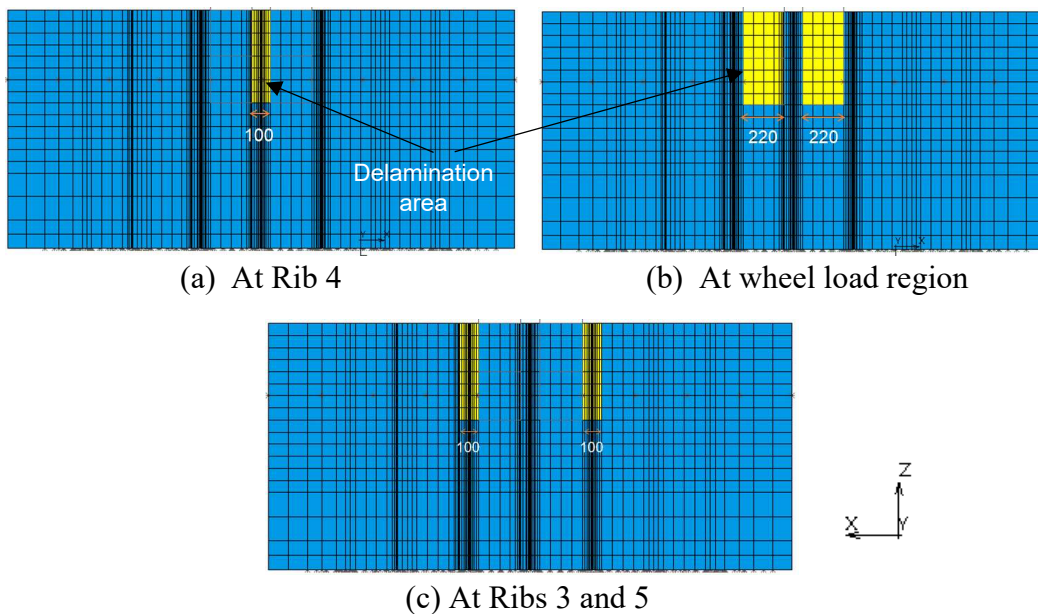
Figure 4.14 Interfacial delamination areas at the separate regions in the analysis

(a) No interfacial delamination

(b) Delamination area at Rib 4

Contour boundary
from model
without bond
degradation

(c) Delamination area at wheel load region

(d) Delamination areas at Ribs 3 and 5
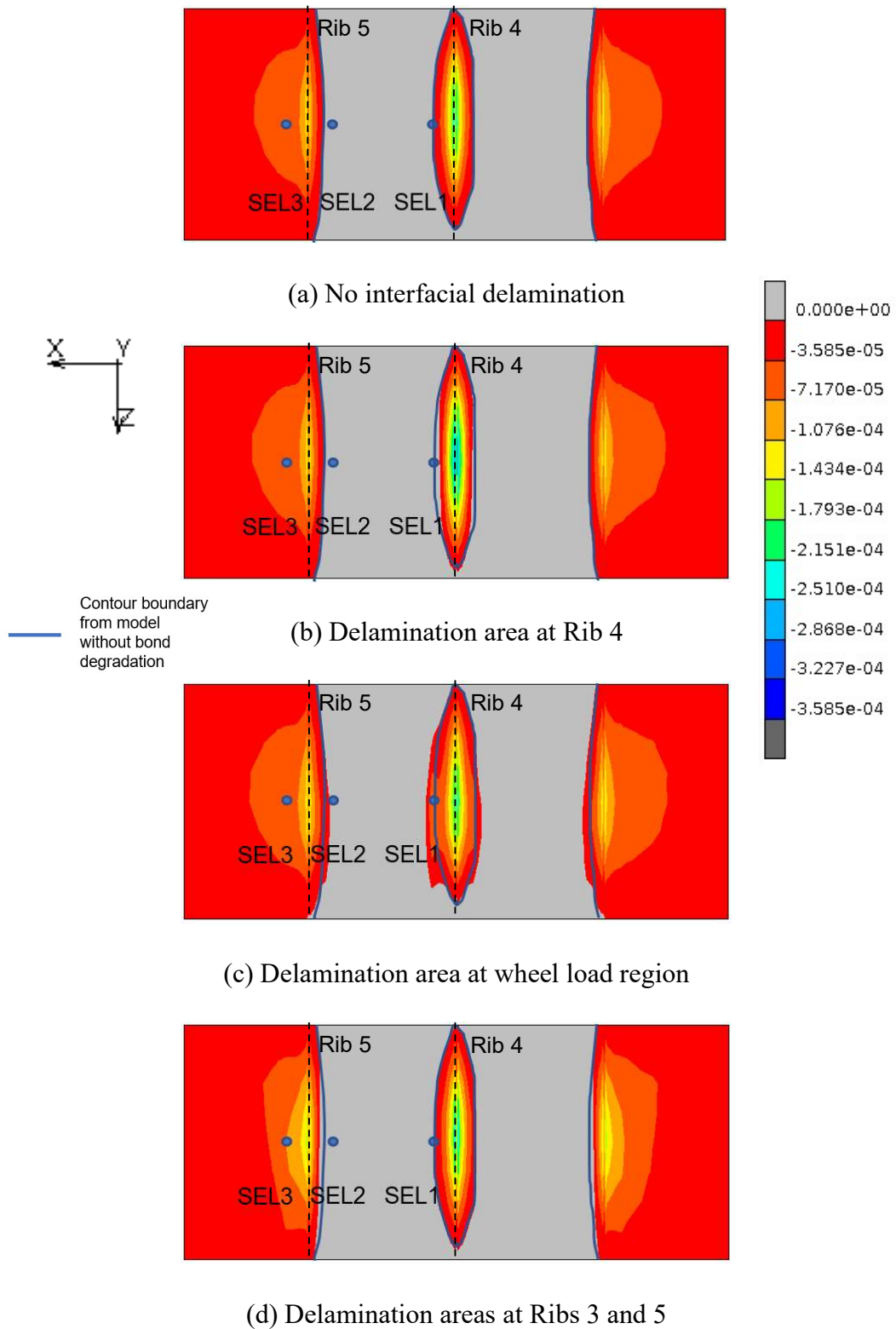
Figure 4.15 Transverse strain distributions in steel deck plate for different interfacial
delamination area (displayed at zone A under load case 10)

the area S_1 for the bond stiffness degradation in phase 1 without covering the longitudinal Ribs 3 and 5, the decreasing tendency in transverse strains at point SEL2 is obtained. Comparing the transverse strain results at strain gauge SEL2 between the analytical models (see Figure 4.12(a)), the minor decreases in strain level are obtained from the current model caused by the wheel load concentration at the middle of the tire patch in this model.

As can be seen from the Figures 4.11 to 4.13, from the 700,000th to 1,100,000th loading cycles, it is obvious that there are sharp variations in both transverse and longitudinal strain levels obtained from the three gauge-points SEL1, SEL2, and SEL3 in the experiment. As discussed in phase 1, the increasing tendency can be obtained at SEL2 when the interfacial degradation area expands across the Rib 5. Therefore, the region S_1 is gradually widened in the transverse direction into area S_2 in the analysis in phase 2 (see Figure 4.4). With the expansion of the delamination area, the analytical strain levels increase significantly after the 700,000th loading cycle, which is caused by the loss of composite action at the interface. In phase 2, two expansion speeds of the delamination

(a) At the 700,000th loading cycle

(b) At the 940,000th loading cycle
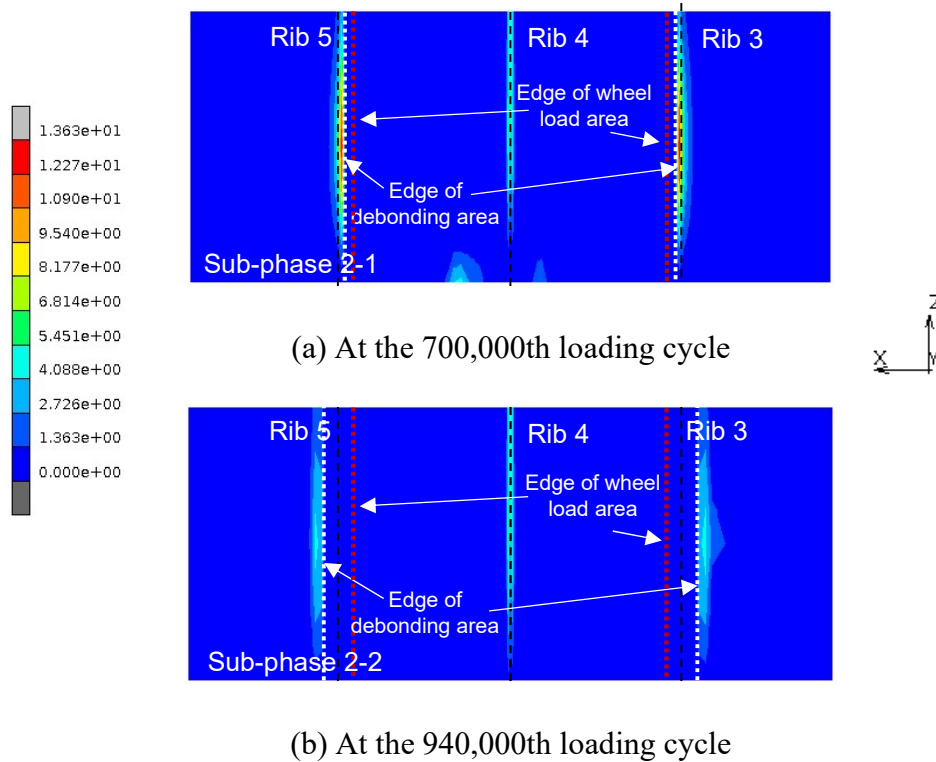
Figure 4.16 Interfacial contact shear stress at zone A in phase 2 of the analysis.

area are used in the analysis, as presented in section 4.3.2, giving an acceptable agreement in tendencies between the analytical and experimental strain results in steel plate. This can be explained by the contact shear stress at the interface which mostly concentrates at the boundary of the delamination area, as shown Figure 4.16. The maximum level of interfacial contact shear stress obtained from the 700,000th cycle is higher than that from the 940,000th cycle. This may be because the edge of delamination area from the 940,000th cycle is far from the wheel load region, the effect of the wheel load on the contact stress concentration at this cycle is thus less than that from the 700,000th cycle. However, the distribution of the contact shear stress from 940,000th is more even, as can be observed in Figure 4.16 (b).

Generally, for the current FEM model considering the two kinds of degradations, the strain results in the steel deck plate show an acceptable agreement with those from the experiment, which verify the reliability of the proposed method. Since the data trends from the experiment were well reproduced by the analytical model, it can be indicated that the considered fatigue degradations of the cracked UHPFRC and the steel-concrete interface, as well as the assumed scenarios with the different interfacial degradation phases were the occurred scenarios in the current experiment of the UHPFRC/steel composite deck. Due to the repetition of contact shear stress, the fatigue degradation of the interfacial bond stiffness between thin layer of UHPFRC and steel plate may always occur right under the local region of wheel loads. The neglect of this fatigue problem can lead to the underestimation of stress range results in OSD, especially at the local region of Rib 4. For examples, the differences in transverse strain results at strain gauge SEL1 between the models with and without considering interfacial fatigue deterioration is more than 5 times (from about -270μ to -50μ). However, in the current stage, even when a part of UHPFRC overlay delaminated from the steel deck plate after 64-year-equivalent traffic load (700,000 wheel moving cycles of 100 kN), the fatigue test found no crack occurred in the steel members of OSD. This demonstrates the UHPFRC overlay can sustain its high rigidity and the fiber bridging effect to resist the local bending in the steel deck plate after fatigue failure at the interface.

4.4.3 Strain results in UHPFRC overlay

As one main factor of fatigue deterioration in the UHPFRC-steel bridge deck, it is significant to investigate the degradation of cracked UHPFRC represented by the crack propagation in the concrete matrix under a moving wheel loading with rubber tire. The maximum strain distributions obtained at the top and bottom layers of the UHPFRC overlay from the fatigue analysis are illustrated in Figure 4.17 for different loading cycles. The strain results are displayed in zone A (see Figure 4.4(b)) under load case 10. As shown in Figure 4.17, the gray color areas represent the cracked regions on the UHPFRC surface. Similar to the static analysis, it is observed from the top layer of UHPFRC that the cracked elements are distributed on the local regions above the longitudinal stiffeners,

(a) At the first loading cycle

(b) At the 700,000th loading cycle

(c) At the 1,100,000th loading cycle
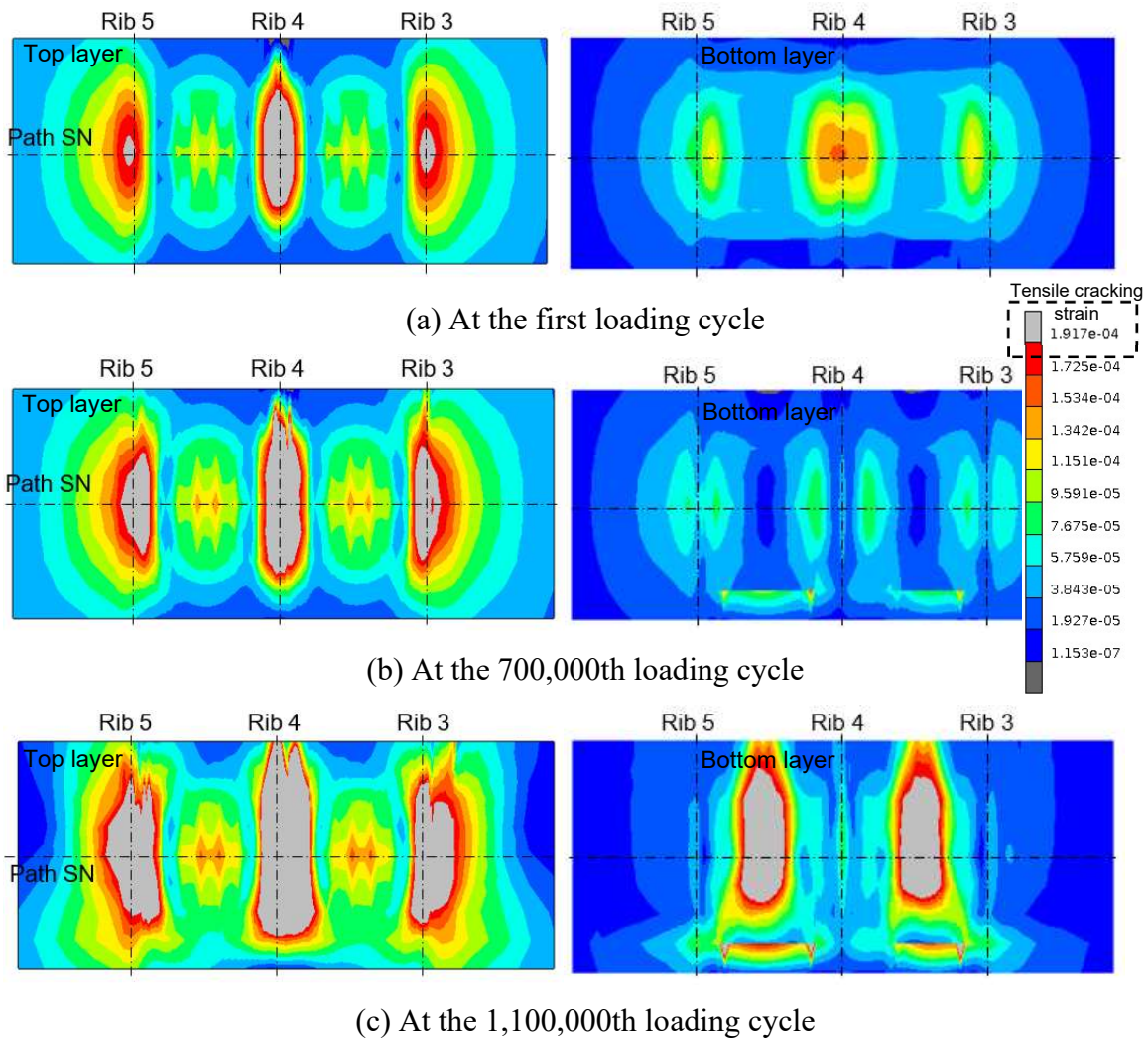
Figure 4.17 Maximum principal strain distributions at zone A under load case 10 on top and bottom layers of UHPFRC overlay (Gray color: crack region)

i.e., Ribs 3, 4 and 5, where the large negative bending moments are obtained. As can be seen in the maximum principal strain distribution along path SN on the top layer of UHPFRC in Figure 4.18, the tensile strain levels are much lower than those from Rib 4, however, the ranges of tensile zones in the transverse direction above Ribs 3 and 5 are wider. The reason is that the negative bending moments above region of Rib 4 are induced by the two balanced wheel loads from two rubber tires. While only one component of wheel load from one tire is acting on the adjacent span of the Rib 3 or Rib 5, leading to the compensating effect is not obtained above these regions, as mentioned in [10]. Therefore, the speeds of crack propagation at the regions above Ribs 3 and 5 are higher than that of Rib 4 causing more expansions of the crack zone at the 700,000th loading cycle. In phase 2, the crack spreading speeds above the longitudinal ribs are remarkably accelerated after the 700,000th loading cycle. This leads to the rapid development of crack zones, especially at Ribs 3 and 5, when the delamination area expands across these regions. Considering the at the bottom layer of UHPFRC overlay, it is found that the tensile cracks initiate under bottom surface of UHPFRC at the end of phase 2 (1,100,000th cycle), as shown in Figure 4.17(c). This is caused by the significant increase in positive
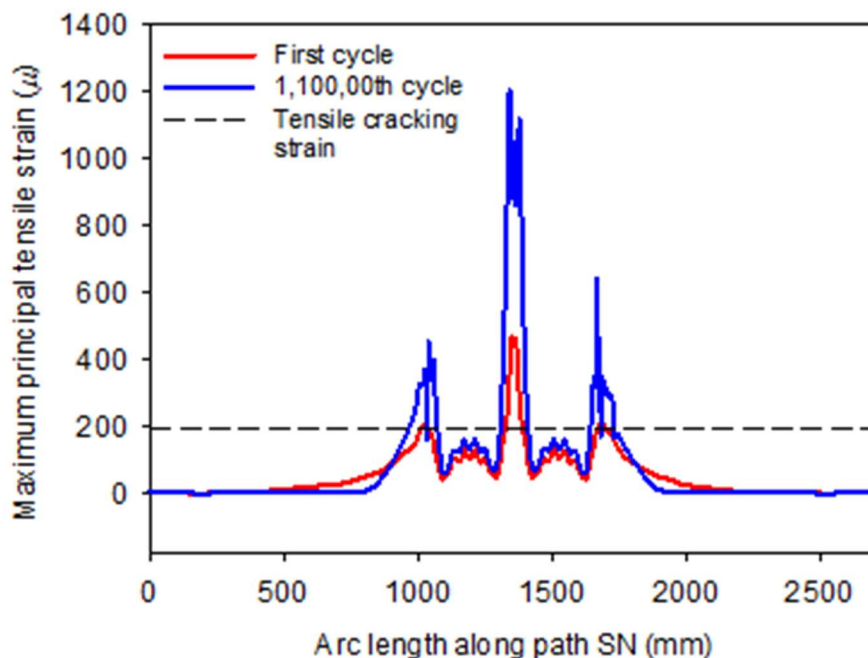
Figure 4.18 Maximum principal strain distributions along path SN on top surface of UHPFRC overlay

bending at the wheel load region after the delaminated interfacial layer loses its possibility in transferring shear stress between UHPFRC overlay and steel deck plate.

The directions of the maximum principal strains from the cracked elements at the 1,100,000th loading cycles are represented in Figure 4.19 for the top and bottom layers of UHPFRC reinforcing overlay. The displayed results are at zone A under load case 10. It is found that the directions of the maximum principal tensile strains in the cracked elements distributed along the ribs are mainly in the transverse direction on top surface of UHPFRC. In other words, the cracks form and propagate in the longitudinal direction above the local regions of the stiffeners. While the diagonal cracks which are distributed around the centerline of the East load patch can be found under bottom surface of UHPFRC overlay at the wheel load region, as can be seen in Figure 4.19(b).

(a) At top layer of UHPFRC

(b) At bottom layer of UHPFRC
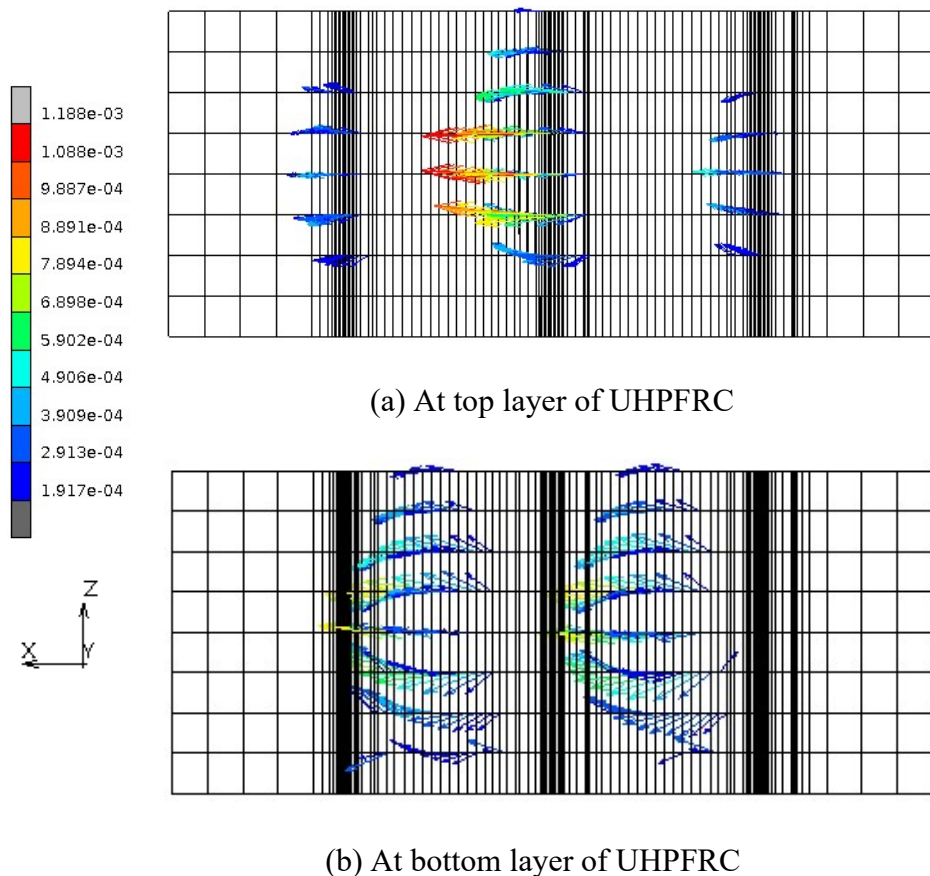
Figure 4.19 Directions of the maximum principal strains from cracked elements at the top and bottom layers of UHPFRC overlay at the 1,100,000th loading cycle

The principal tensile strain distributions on top surface of UHPFRC overlay for the different load cases of moving wheel load are shown in Figure 4.20, in comparison between the first and the 1,100,000th loading cycles. From Figures 4.20(a) to 4.20(d), the wheel tire load moves from the East load patch toward the Center load patch, following

(a) Load case 10   (b) Load case 11

(c) Load case 12   (d) Load case 13
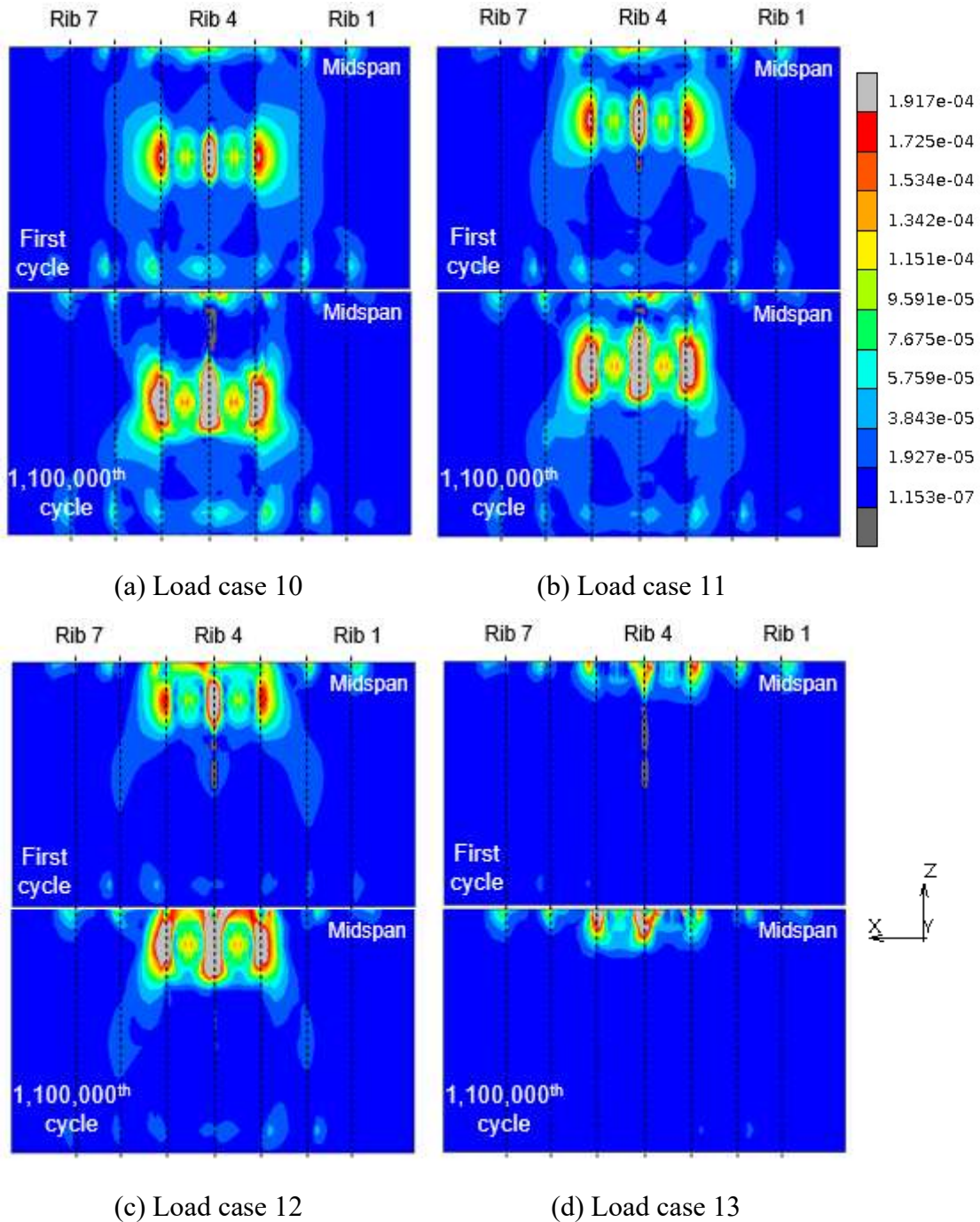
Figure 4.20 Maximum principal tensile strain distributions for each load case of moving wheel load on top surface of UHPFRC layer (Gray color: crack region)

74

the load cases in the Figure 4.3. From the analysis, it is found that the tensile strain magnitudes continuously increase when the wheel load moves from load cases 10 to 12. The highest value of tensile strain on the top surface of UHPFRC is obtained at Rib 4 from load case 12. The reason is that the longitudinal ribs become stiffer by the connections with the middle cross beams under the midspan, which generate the more negative bending moment above the ribs. Thus, the larger crack zones are obtained from load case 10 to 12. As can be seen from Figure 4.20(c), at load case 12 from the 1,100,000th loading cycle, the wheel load also produces negative bending at the local region above the middle cross beam, and the cracks propagate along the midspan between longitudinal Ribs 3 and 5. At Center location or load case 13, due to the strengthening effect of the middle cross beam, the numbers of cracked element are much smaller than those from the other load cases (see Figure 4.20(d)). In addition, it is noticed that under the current level of wheel load (100 kN), there is no occurrence of a localized crack in the analysis. The crack zones are only composed of the multiple fine cracks which are formed in the strain hardening domain of UHPFRC. This is caused by the high tensile cracking and ultimate strengths, as well as the high fatigue resistance after cracking of the developed UHPFRC. As a result, the fatigue degradation in the current OSD-UHPFRC composite bridge deck is generally driven by the interfacial bond degradation, as mentioned in section 4.4.2.

4.5 Summary

In this chapter, fatigue performances of the composite bridge deck in stage 1 subjected to a moving wheel loading with rubber tire under dry condition are investigated by a fatigue analysis based on the appropriate model chosen from the static analysis.

Due to the progressive reduction of the interfacial bond stiffness under tire contact zone in phase 1 and the expansion of the debonding area in phase 2, the overall stiffness of the composite deck decreased with the increase of loading cycles leading to the continuous deformation increases in both UHPFRC and steel deck plate. The other cause of stiffness decrease was the progressive cracks caused by the bridging stress degradation. It was found in the analysis that the cracked elements were distributed on the local regions

above the longitudinal stiffeners, i.e., Ribs 3, 4, and 5, where the large negative bending moments are obtained.

As the data tendencies from the experiment were well reproduced by the numerical model, it may be stated that the considered degradations of the cracked UHPFRC and the steel/UHPFRC interface, as well as the scenarios for the different phases of interfacial degradation could be applied for stage 1 of fatigue test under a moving wheel loading with rubber tire.

CHAPTER 5 FATIGUE ANALYSIS OF THE UHPFRC-STEEL COMPOSITE BRIGDE DECK SUBJECTED TO A MOVING LOADING WITH RUBBER TIRE UNDER SURFACE WATER CONDITION

5.1 Introduction

In this chapter, the fatigue behaviors of the UHPFRC-steel composite bridge deck subjected to a moving wheel loading with rubber tire (see Figure 5.1) are subsequently investigated and evaluated under surface water condition in stage 2 of fatigue analysis after the first stage under dry condition, as presented in Chapter 4. The FEM model of the composite bridge deck (see Figure 5.2) and the procedure for fatigue analysis under moving loading with rubber tire (see Figure 5.3) are the same as those from the previous stage. Two phases of the material model considering self-healing behavior and reduction of fatigue life for cracked UHPFRC are assumed in the analysis for the second stage of fatigue analysis. The assumed scenarios for the material model of cracked UHPFRC are then assessed by examining the displacement and strain behavior in steel deck plate and UHPFRC crack propagation throughout the analysis of stage 2.

Figure 5.1 Fatigue test of UHPFRC-steel composite bridge deck in stage 2 subjected to a moving wheel loading with rubber tire under surface water condition [9]
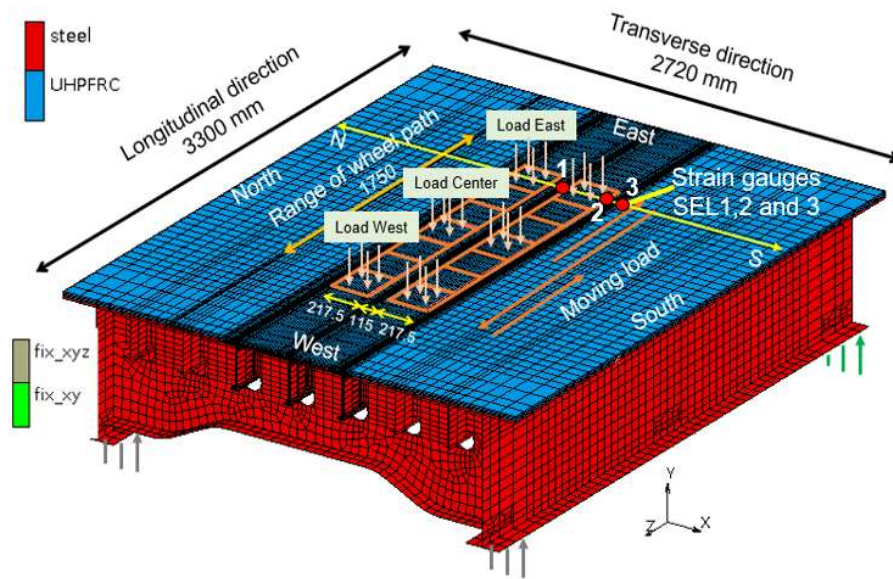
Figure 5.2 FEM model of UHPFRC-steel composite bridge deck subjected to a moving wheel loading with rubber tire under surface water condition.
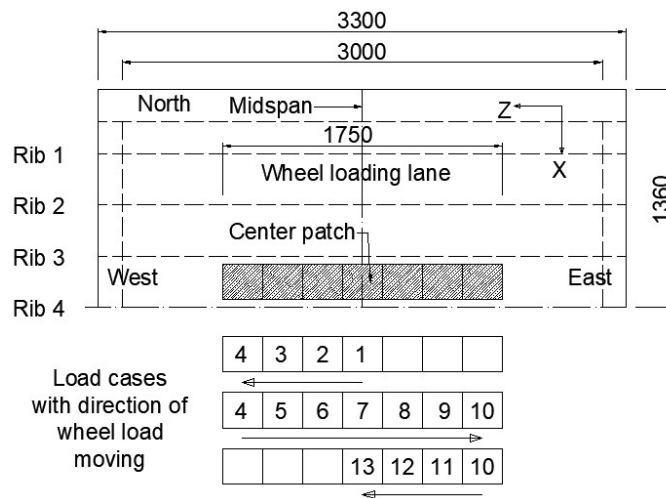
Figure 5.3 Load cases in accordance with the direction of moving loading with rubber tire.

5.2 Assumed phases for material model of cracked UHPFRC under surface water condition

After the first stage with 1,100,000 cycles subjected to moving wheel loading with rubber tire under dry condition, the composite deck was subsequently tested for 60,000

78

cycles under surface water condition in one day. A thin layer of water had been supplied on the top surface of UHPFRC overlay for one night before the stage 2 of fatigue test under surface water condition. Correspondingly, in the current fatigue analysis, two phases are assumed for the material model of cracked UHPFRC as follows

- Phase 1: self-healing of cracked UHPFRC for one night from the 1,100,000th to the 1,100,0001st loading cycles.

- Phase 2: a higher degradation speed of cracked UHPFRC caused by the stagnant water for 60,000 cycles.

5.2.1 Phase of self-healing in cracked UHPFRC for one night from the end of the 1,100,000th cycle to the beginning of the 1,100,0001st cycle (phase 1)

As represented in Section 2.3.6, for phase 1 of the current analysis, the mechanical recoveries in term of reloading stiffness and tensile strength caused by the autogenous self-healing are applied to the cracked UHPFRC from the end of dry condition (1,100,000th cycle) to the beginning of surface water condition (1,100,001st cycle), as shown in Figure 5.4. The recovery ratios for the reloading stiffness, κ, and the tensile strength, ξ, in the cracked UHPFRC are represented as follows

$$\kappa = \frac{K_{1,100,001} - K_{1,100,000}}{K_1 - K_{1,100,000}} \tag{5.1}$$

$$\xi = \frac{\sigma_{1,100,001} - \sigma_{1,100,000}}{\sigma_1 - \sigma_{1,100,000}} \tag{5.2}$$

where K_1 is the elastic stiffness at the first cycle

$K_{1,100,000}$ and $K_{1,100,001}$ are the reloading stiffnesses at the 1,100,000th and 1,100,001st cycles, respectively.

σ_1, $\sigma_{1,100,000}$ and $\sigma_{1,100,001}$ are the crack bridging stresses at the first, 1,100,000th and 1,100,001st cycles, respectively.

Since the exposure time of the top surface of UHPFRC overlay under surface water condition is one night, the reloading stiffness and tensile strength recovery ratios in this study are roughly chosen as 70%, $\kappa = \xi = 70\%$, following the research of Okuizumi et al. [48].
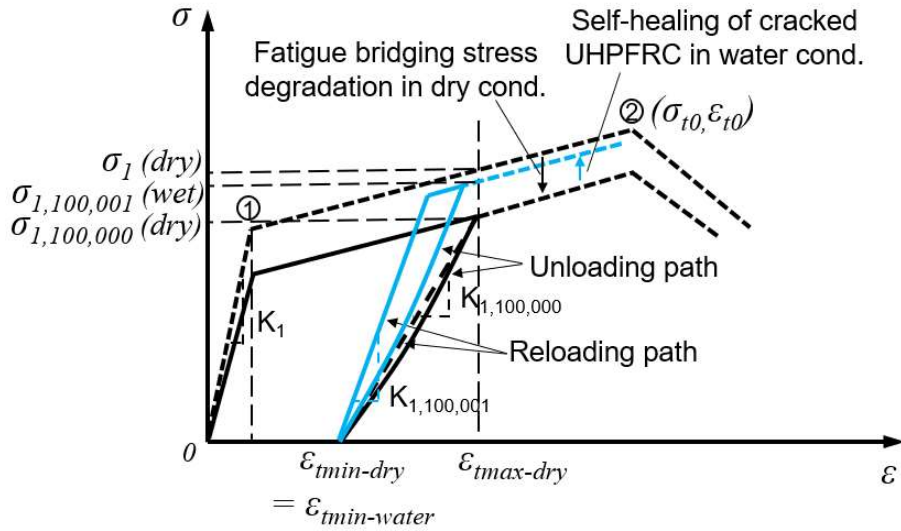
Figure 5.4 Tensile stress-strain relation of cracked UHPFRC under surface water condition

5.2.2 Stage of the increase in fatigue degradation speed of cracked UHPFRC from the 1,100,001st to the 1,160,0000th cycles (phase 2)

The bridging stress degradation law of UHPFRC material applied for the composite bridge deck under dry condition (stage 1) was presented in Chapter 4 as follows

$$\frac{\sigma_N}{\sigma_1} = 1 - (0.015 + 5\varepsilon_{t\max})\log(N) \tag{5.3}$$

$$\text{for } 1 \le N \le 1,100,000$$

where ε_{tmax} is maximum tensile strain

N is number of loading cycles

σ_N/σ_1 is bridging stress degradation ratio between the N_{th} and the first cycles.

For stage 2 of fatigue analysis, following Section 2.3.5.2, the bridging stress degradation relation of cracked UHPFRC under surface water condition is applied to the material model of UHPFRC as follows

$$\frac{\sigma_N}{\sigma_{1,100,001}} = 1 - (0.058 + 3.5\varepsilon_{t\max})\log(N - 1,100,000) \tag{5.4}$$

$$\text{for } 1,100,001 \le N \le 1,160,000$$

in which $\sigma_N/\sigma_{1,100,001}$ is bridging stress degradation ratio of the Nth to the 1,100,001st cycle in surface water condition.

5.3. Interfacial bond degradation between UHPFRC overlay and steel deck plate

For stage 2, the fatigue degradation at the interface between the two materials is continued to be governed by the transverse expansion of the interfacial delamination area. Due to the lack of information about the hammer test results in this stage, the expansion speed from the previous stage under dry condition from the 940,000th to 1,100,000th cycles is simply used for interfacial condition in stage 2. The total expansion of 28 mm in transverse direction is then applied for the interfacial debonded area in the analysis. That is, from the 1,100,000th to 1,160,000th cycles, the transverse dimension of the delamination area is gradually increased from 840 mm to 868 mm, as shown in Figure 5.5.

(a) At 1,100,000th or 1,100,001st cycle   (b) At 1,160,000th cycle
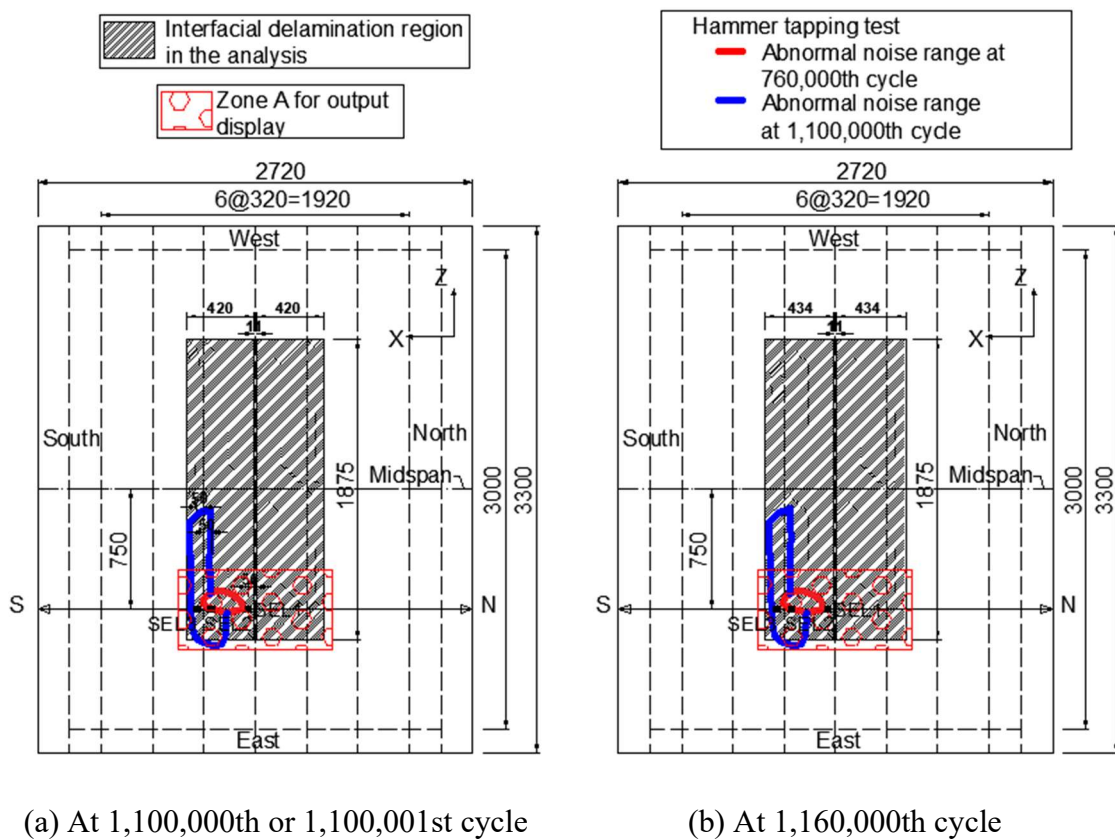
Figure 5.5 Delamination area at interfacial bond layer for stage 2 of the fatigue analysis

5.4 Results and discussions

5.4.1 Displacement results
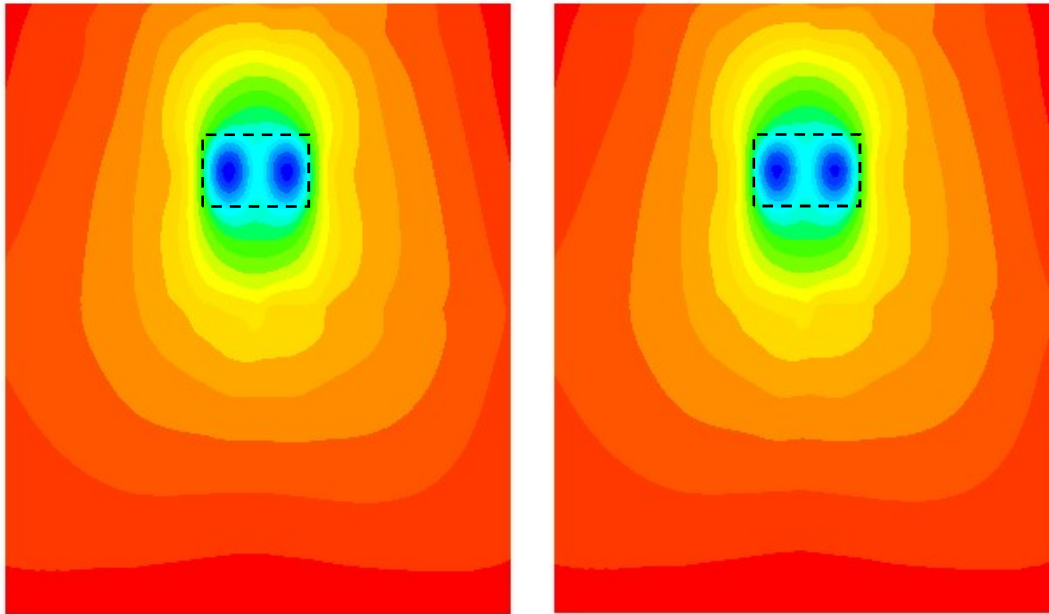
(a) At 1,100,000th cycle (stage 1)   (b) At 1,100,001st cycle (stage 2)
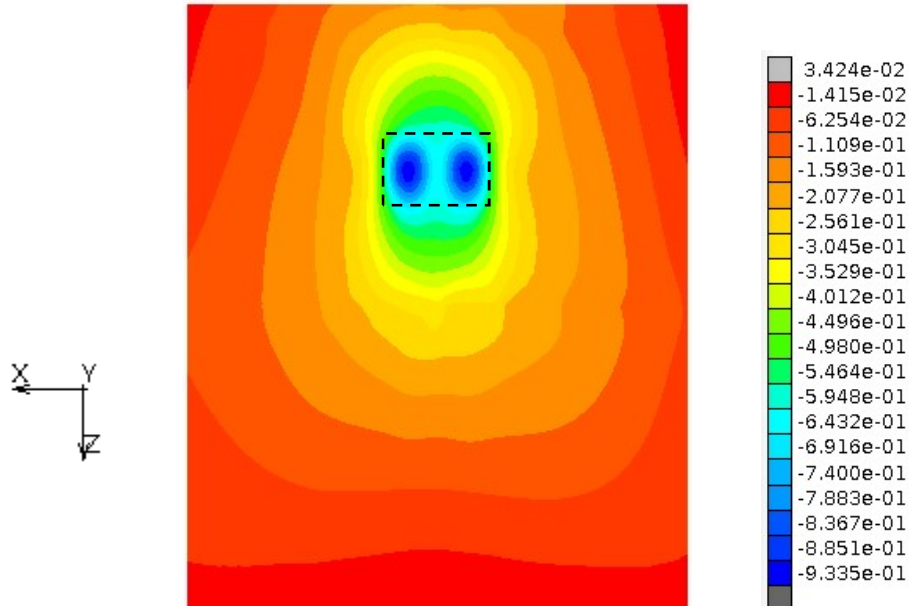
(c) At 1,160,000th cycle (stage 2)

Figure 5.6 Vertical displacement distribution under bottom of the steel deck plate for different cycles of fatigue analysis.
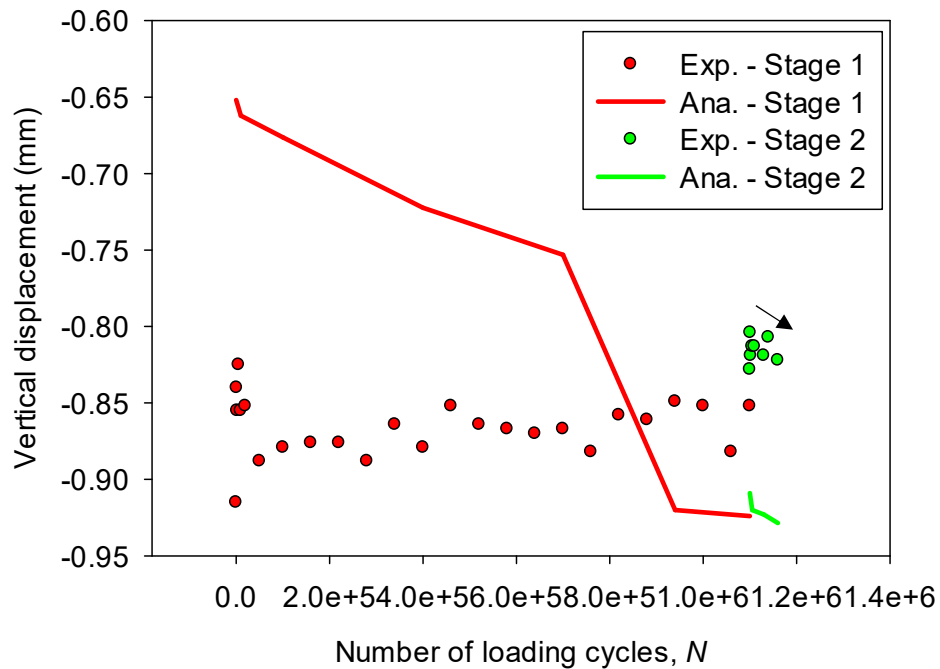
Figure 5.7 Maximum vertical displacement versus the number of loading cycles from stage 2 of fatigue analysis.

The vertical displacement distributions under bottom of steel deck plate obtained from load case 10 for different cycles from the stage 1 and 2 of fatigue analysis are presented in Figure 5.6. It can be known from Figure 5.6(b) that the magnitudes of displacement in steel bridge deck decrease at the beginning of stage 2 due to the self-healing of UHPFRC cracks in the overlay as assumed for phase 1 of the UHPFRC's material model. The reduction in maximum displacement level also agrees with that from the experiment, as shown in Figure 5.7.

Throughout stage 2, due to the shortening in fatigue life of cracked UHPFRC caused by the stagnant water, the analytical displacement levels increase markedly after 60,000 loading cycles (see Figure 5.7), which exhibits the relative agreement with the tendency from the experimental data.

5.4.2 Strain results in steel deck plate

The transverse strain distributions for each phase in the steel deck plate obtained from the East load patch under load case 10 are shown in Figure 5.8. It is obvious that, due to

83

(a) At 1,100,000th cycle (stage 1)

(b) At 1,100,001 cycle (stage 2)

(c) At 1,160,000th cycle (stage 2)
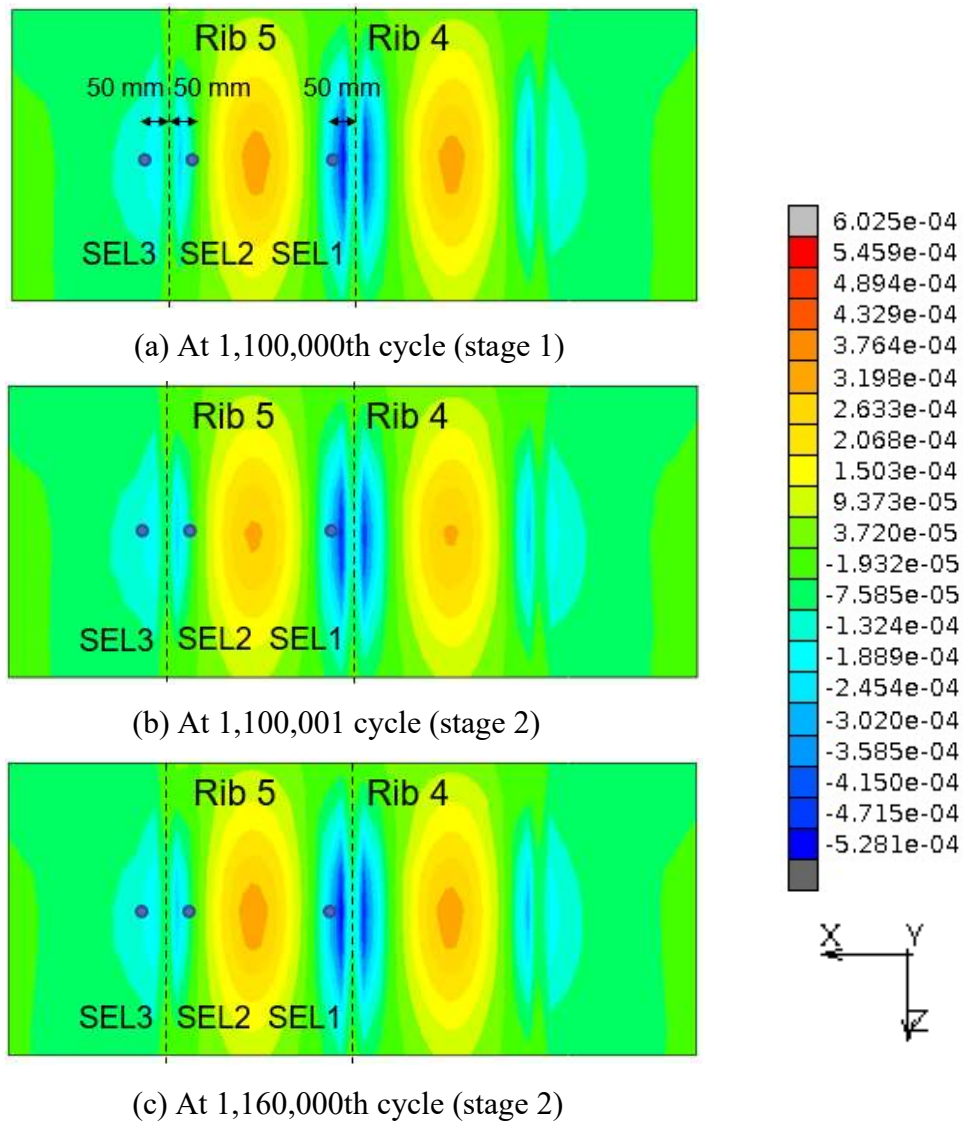
Figure 5.8 Transverse strain distribution in steel deck plate versus the number of loading cycles at zone A (shown in Figure 5.5) under load case 10.

the increase in tensile strength caused by the autogenous self-healing of the fine cracks in UHPFRC overlay, the overall stiffness of the composite deck increases after one-night exposure in water. This leads to the decreases in strain levels in both compressive zones above the longitudinal stiffeners (ribs) and the tensile zones under the contact area of the wheel path in steel deck plate at the 1,100,001st loading cycle. As for the mechanical recoveries in phase 1 of cracked UHPFRC, it can be interpreted by the opening-closing process of a single crack before and after self-healing, as illustrated in Figure 5.9. As can be seen from Figure 5.9(d), with the existence of the healing part inside UHPFRC crack, the stress transfers between pulled-out or ruptured fibers have been restored, causing the

increase in bridging stress between the crack surfaces. As a result, the decrease in reloaded maximum strain or the crack opening displacement can be obtained after the self-healing of UHPFRC crack. It is noted that, the autogenous self-healing process of the UHPFRC cracks is assumed to finish at the beginning of the 1,100,001st cycle, and the healing parts are kept unchanged throughout stage 2 of fatigue analysis. Therefore, the unloaded minimum strain in water condition is maintained equal to that from dry condition, as shown in Figure 5.9(e).

(a) Loading in dry cond.   (b) Unloading in dry cond.

(c) Self-healing part formed inside UHPFRC crack in phase 1

(d) Reloading in water cond.   (e) Unloading in water cond.
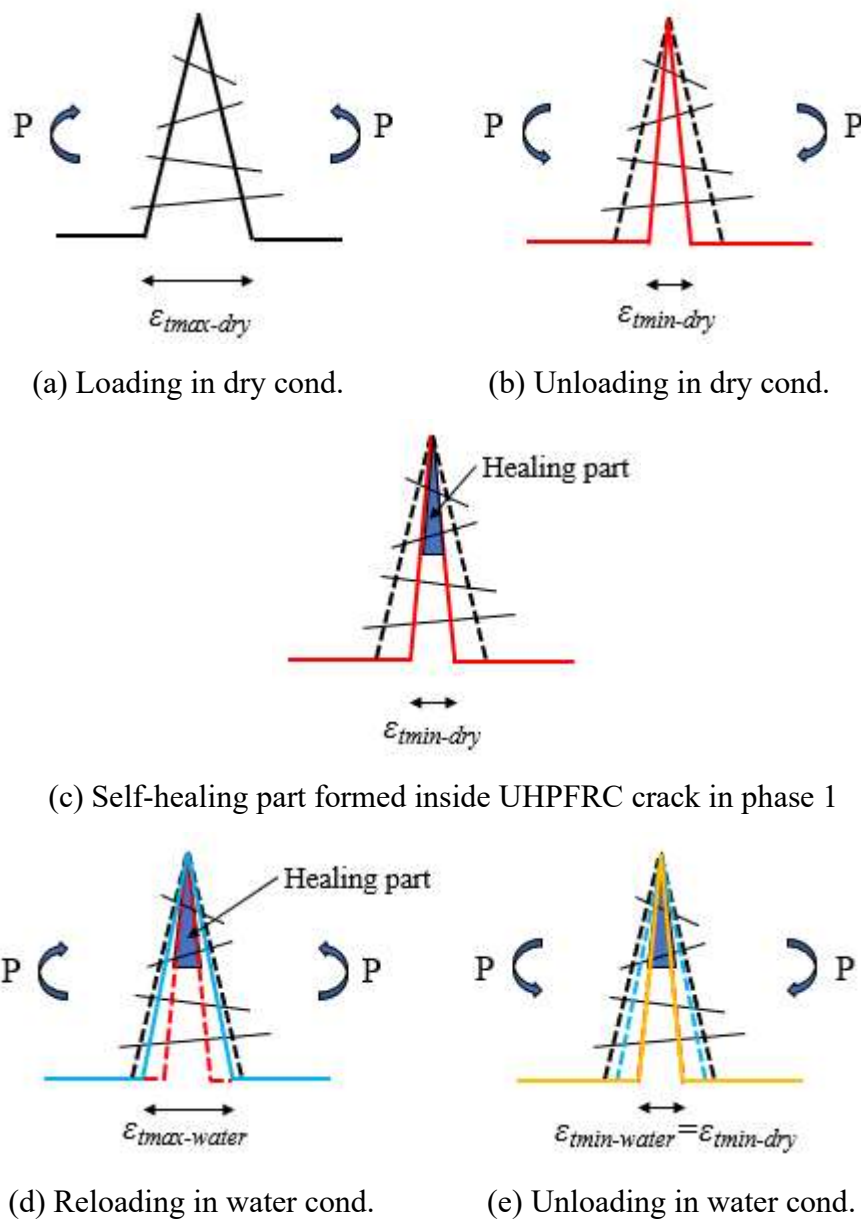
Figure 5.9 Opening-closing behaviors of a UHPFRC crack before (a and b) and after (d and e) self-healing.

The relationships between the transverse strain range evolutions under load case 10 obtained from the positions of the strain gauges SEL1, SEL2 and SEL3 versus the number of loading cycles are plotted in comparison to the experimental data in Figures 5.10 to 5.12, respectively. The decreases in strain range magnitudes obtained at the strain gauges can be clearly observed from the end of stage 1 to the beginning of stage 2 owing to the self-healing of UHPFRC cracks in the reinforcing overlay, as discussed above. Thereafter, in phase 2 of the material model for cracked UHPFRC, the increase in degradation speed
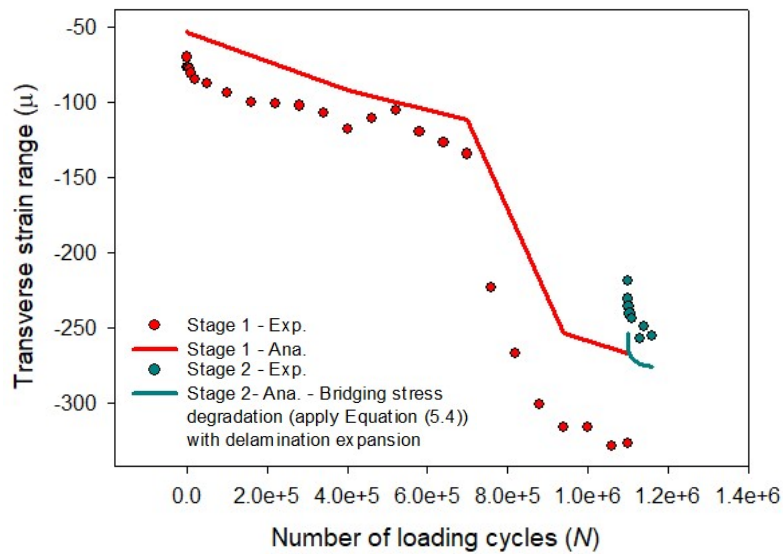
(a) Stages 1 and 2
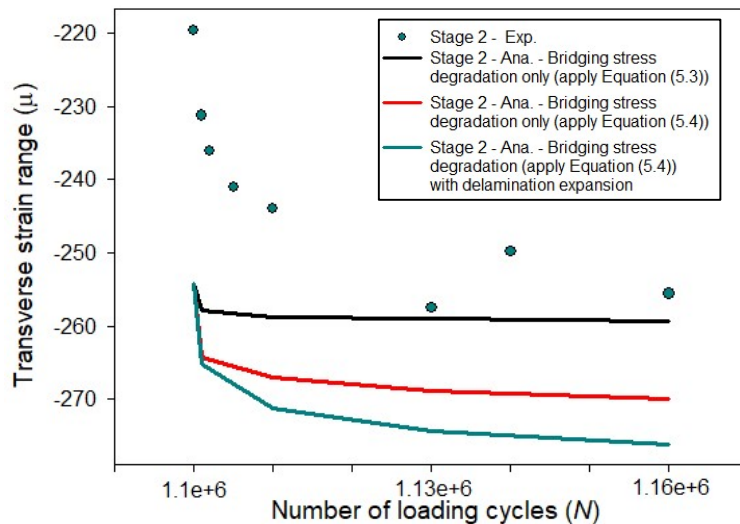
(b) Stage 2 only

Figure 5.10 Transverse strain range versus the number of loading cycles at strain gauge SEL1 in steel deck plate
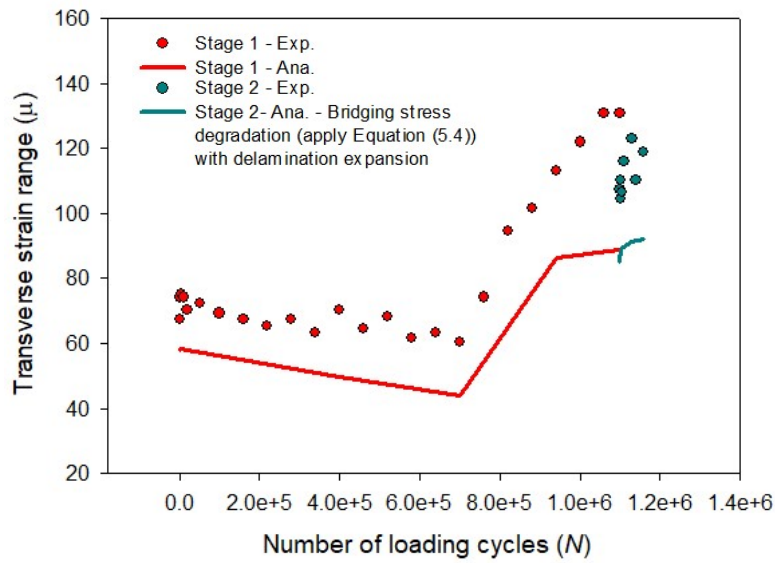
(a) Stages 1 and 2
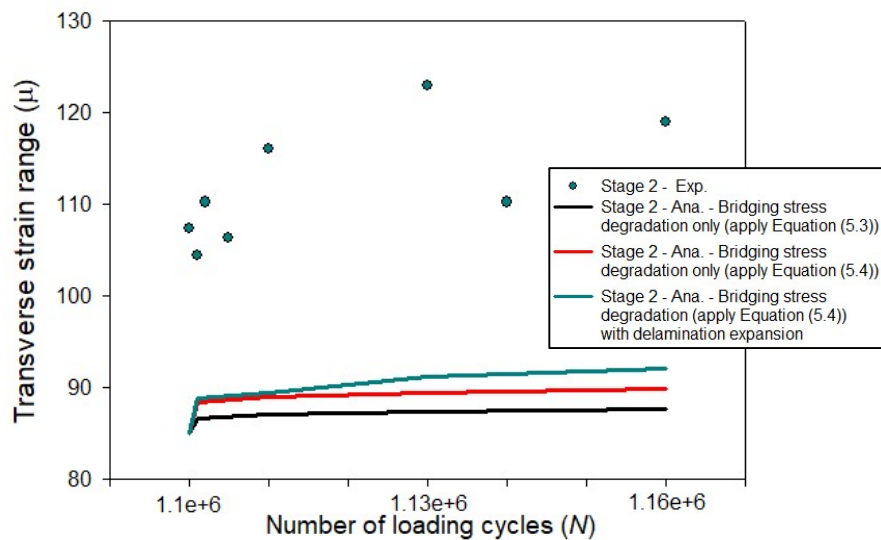
(b) Stage 2 only

Figure 5.11 Transverse strain range versus the number of loading cycles at strain gauge SEL2 in steel deck plate

of bridging stress in cracked UHPFRC is applied in the analysis, as presented in Equation (5.4). This leads to the sharp increases in transverse strain range levels from the early cycles of stage 2 of fatigue analysis in steel deck plate (cycles from 1,100,001st to 1,105,000th), which exhibits the acceptable agreement in tendency to the data from experiment. From the models applying Equations (5.3) and (5.4), it can be seen that the increase in bridging stress degradation speed may probably occur in cracked UHPFRC
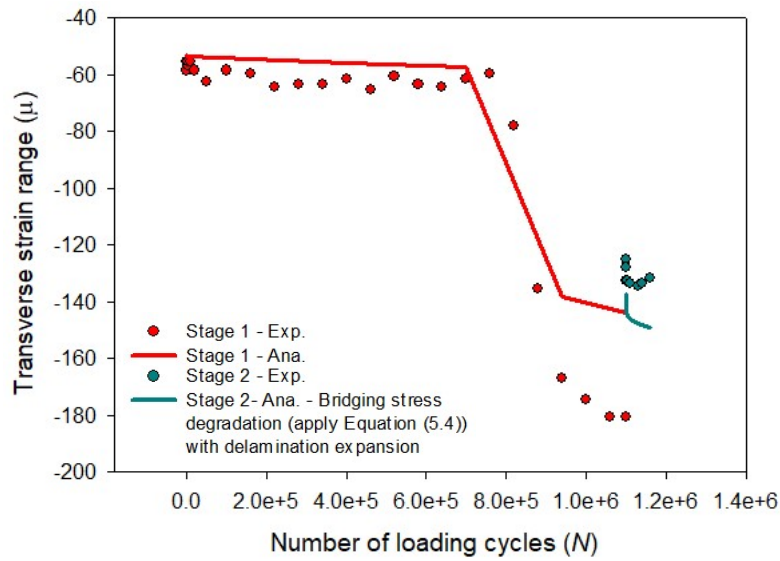
(a) Stages 1 and 2
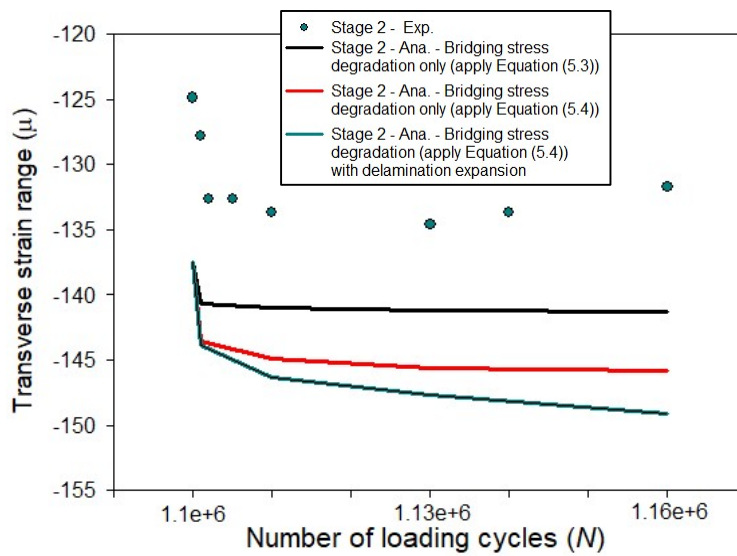
(b) Stage 2 only

Figure 5.12 Transverse strain range versus the number of loading cycles at strain gauge SEL3 in steel deck plate

due to the existence of the stagnant water. This mechanism can be explained by the generated water pressure inside the cracks under repetitive cyclic loading, as illustrated in Figure 5.13. Under cyclic loading, the water pressure acting on the crack surfaces turns into negative values with the opening process of UHPFRC crack. In contrast, the positive water pressure can be obtained when UHPFRC crack closes with water. Hence, under the repetitive moving wheel load, the additional forces caused by stagnant water may
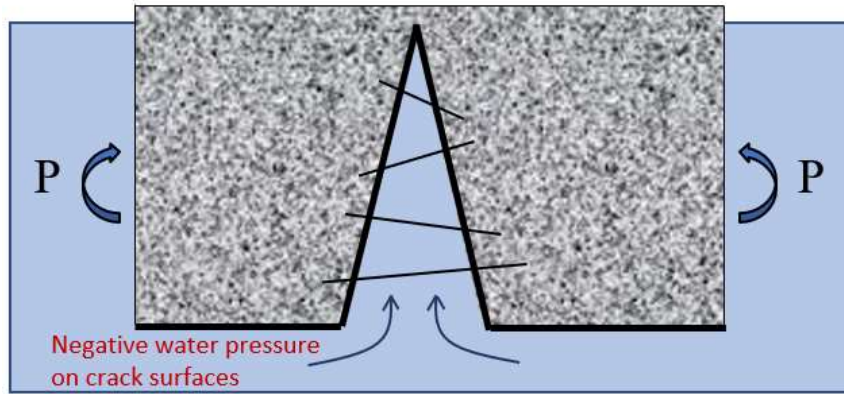
(a) Crack opening in water
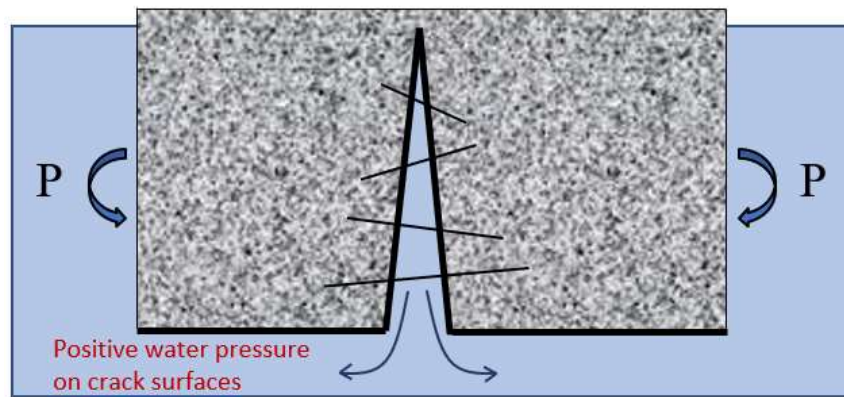
(b) Crack closure in water

Figure 5.13 Water pressure generated inside a UHPFRC crack under cyclic loading

accelerate the fatigue fiber deterioration (i.e., fiber pullout) in the fracture zone, which may result in the increase in the degradation speed of bridging stress in cracked UHPFRC as assumed for phase 2 of UHPFRC's material model.

Comparing the models with and without the interfacial bond stiffness degradation, it is clearly seen that the contribution of bridging stress degradation on the increases of strain range is dominant in the early stage of fatigue analysis under surface water condition, since the expansion of debonding area is relatively small at the beginning cycles. With the increase of the number of loading cycles, more increases in strain ranges in steel plate are obtained due to the continuous loss in composite action between UHPFRC and steel plate when the delamination area is progressively expanded in transverse direction.

Overall, for the current FEM model considering the two phases for the material model of cracked UHPFRC under surface water condition as well as the transverse expansion of the interfacial delamination area, the transverse strain range results in steel deck plate show an acceptable agreement in tendency with those from experiment. Therefore, it can be stated that the assumed behaviors in the material model of cracked UHPFRC in the analysis are reasonable for reproducing the experiment. However, at the end of fatigue test of composite deck in surface water condition (1,160,000th cycle), the experimental strain range levels are still lower than those from the 1,100,000th cycle in dry condition. This may be due to the neglect of the residual bond slip at the UHPFRC/steel interface caused by the fatigue loading as presented in Section 2.4, which may lead to the underestimation of the unloading strain levels of steel plate in the analysis. Figure 5.14 shows the loading and unloading transverse strain results at strain gauge SEL1 in comparison between the analysis and the experiment. It is observed that there are large differences between the analytical and experimental results since the residual bond slip at each loading cycle is neglected. From the end of stage 1 to the beginning of stage 2, not only the decrease in loading strain level but also the increase in unloading strain magnitude is observed from the experimental data. The significant decrease in experimental strain range level is then obtained, as shown in Figure 5.10. Although the
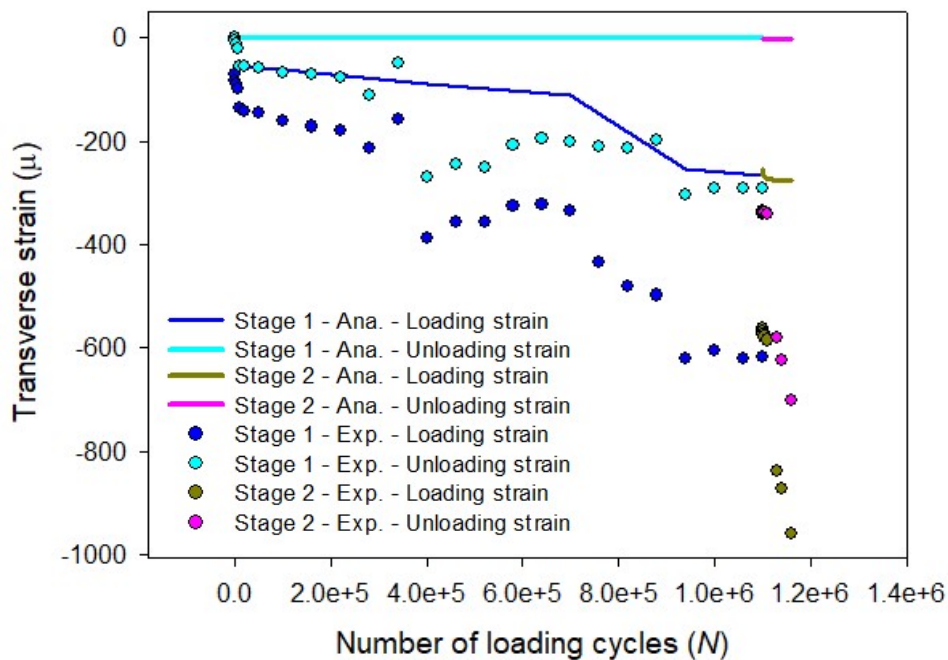
Figure 5.14 Loading and unloading strain results versus number of cycles at SEL1

90

experimental tendencies from strain range results can be relatively reproduced by the current model, the reproduction of the unloading strain levels caused by the residual bond slip at interface is also a topic for future studies of the composite bridge deck under moving wheel loading.

5.4.3 Strain results in UHPFRC overlay

The maximum strain distributions from the cracked elements obtained on the top and bottom layers of UHPFRC overlay under load case 10 from stages 1 and 2 are showed in Figures 5.15. The strain results are displayed in zone A (see Figure 5.5). The cracked regions on UHPFRC surface are represented by the band from blue to red colors. It is obvious that the cracked elements on the top surface of overlay are distributed on the local regions above the longitudinal stiffeners (Ribs 3, 4 and 5), while the wheel load produces tensile cracks at bottom layer of UHPFRC overlay at the contact regions of rubber tire.

(a) At 1,100,000th loading cycle (stage 1)

(b) At 1,100,001st loading cycle (stage 2)

(c) At 1,160,000th loading cycle (stage 2)
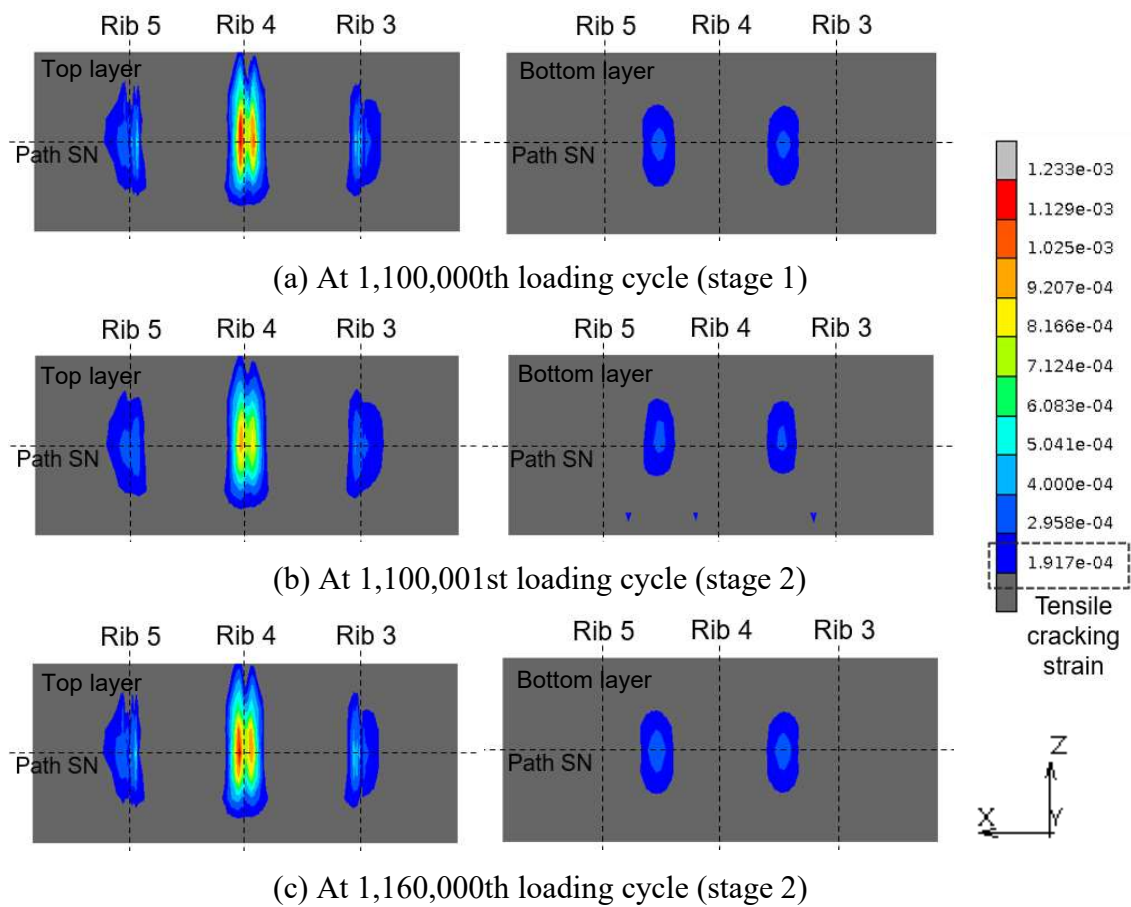
Figure 5.15 Maximum principal strain distributions from cracked areas under load case 10 on top and bottom layers of UHPFRC overlay

At the beginning of fatigue analysis in stage 2 (1,100,001st cycle), due to the increase in tensile strength caused by the self-healing of cracks on the top surface of UHPFRC overlay, the maximum tensile strain levels from both top and bottom layers of UHPFRC overlay decrease as compared to those from dry condition. On the contrary, the increases in tensile strain levels in UHPFRC are obtained at the end of this stage owing to the significant increase in degradation speed of bridging stress of healed UHPFRC with stagnant water. Due to the lesser deformation obtained from the beginning of stage 2 compared to that from the end of stage 1, the narrower crack region at the 1,100,001st cycle is observed at the bottom layer of overlay (see Figure 5.15(b)), compared with that from the 1,100,000th cycle (see Figure 5.15(a)). For the top layer, the changes in longitudinal dimension of crack regions are inconsiderable due to the existence of the longitudinal stiffeners (Ribs 3, 4 and 5).

The directions of the maximum principal strains from cracked elements at the top and bottom layers of UHPFRC overlay at the 1,160,000th loading cycle are shown in Figure 5.16. Similar to the observations from the previous stage under dry condition, the tensile

(a) At top layer of UHPFRC

(b) At bottom layer of UHPFRC
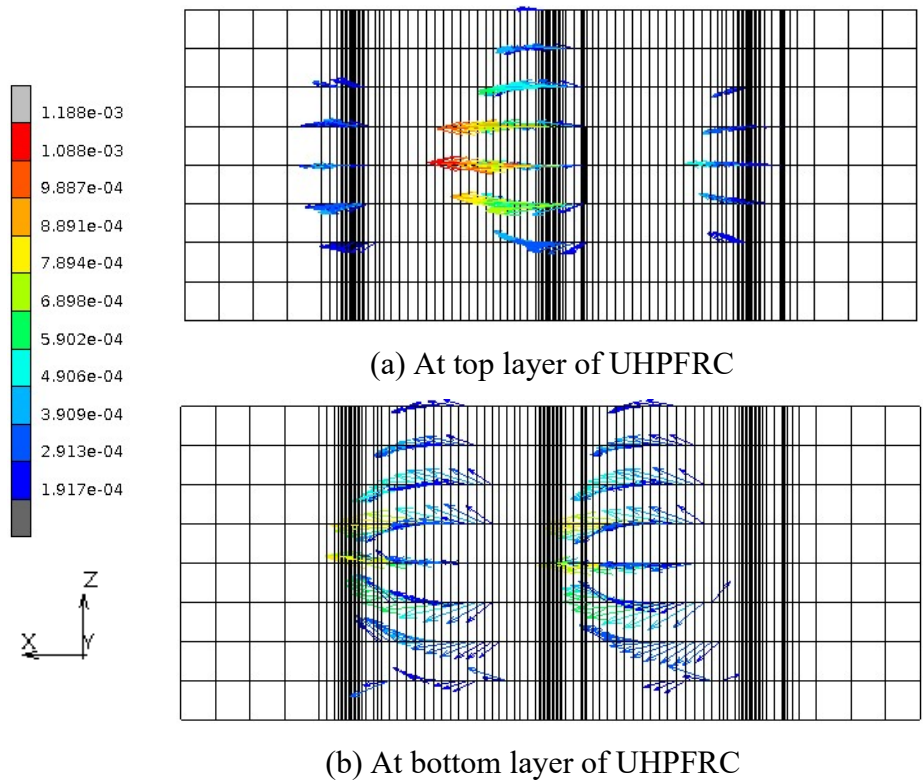
Figure 5.16 Directions of the maximum principal strains from cracked elements at the top and bottom layers of UHPFRC overlay at the 1,160,000th loading cycle

cracks form and propagate in the longitudinal direction above the stiffeners on the top layer of UHPFRC. While, under bottom surface of the overlay, the diagonal cracks are distributed at the contact region of wheel load (see Figure 5.16).

Figure 5.17 presents the principal tensile strain distributions on top surface of

(a) Load case 10   (b) Load case 11

(c) Load case 12   (d) Load case 13
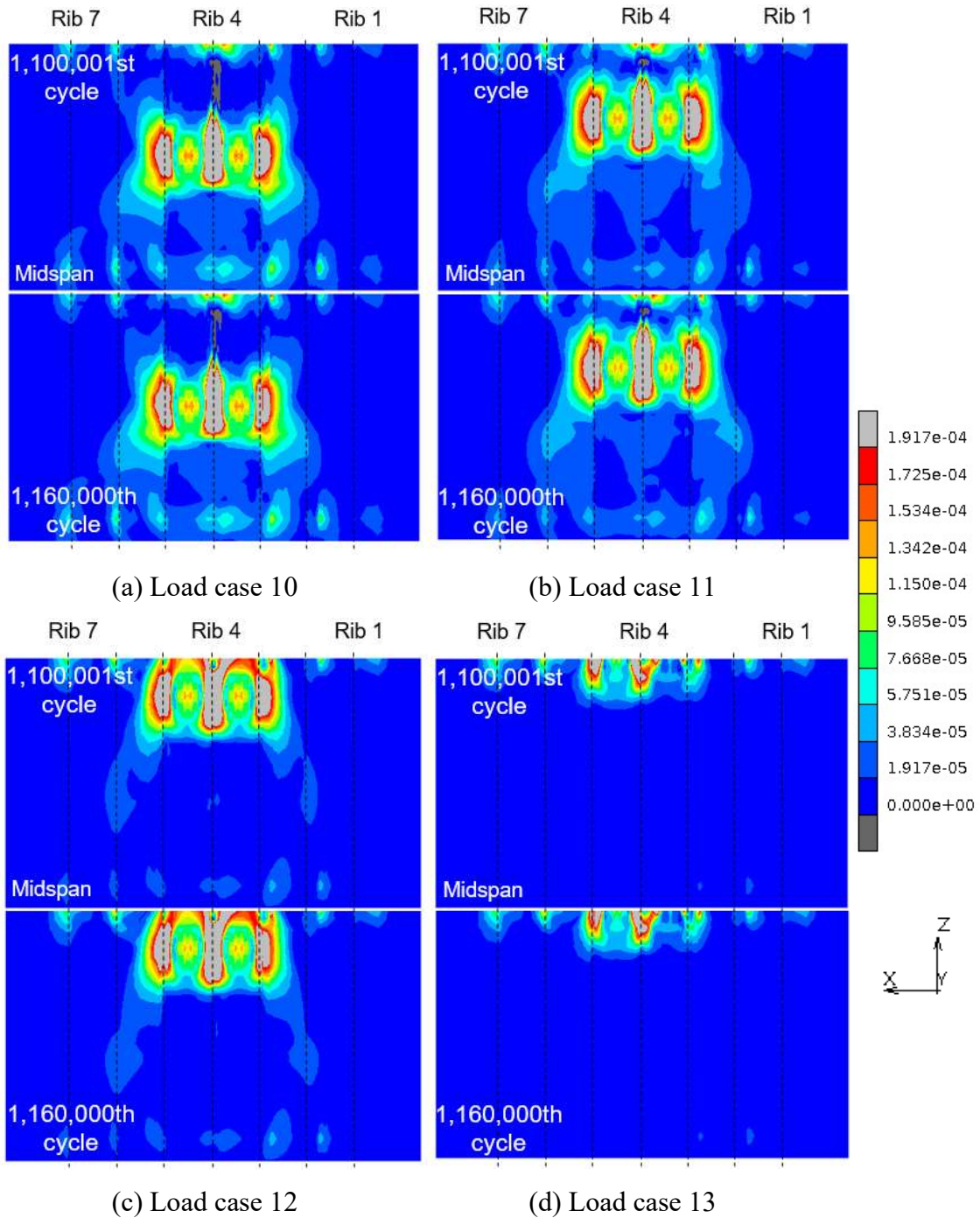
Figure 5.17 Maximum principal strain distributions for each load case of moving wheel load on top surface of UHPFRC layer (Gray color: crack region)

UHPFRC overlay for the different load cases of moving wheel load in comparison between the 1,100,001st and the 1,160,000th loading cycles. The cracked regions are represented by gray color. From the analysis, the highest level of maximum principal strain on the top surface of UHPFRC is obtained at the middle rib (Rib 4) from load case 12 (see Figure 5.17(c)). At the end of this stage, from load case 12, it is found that the multiple fine cracks have not been localized in the analysis. Despite the significant increase in bridging stress degradation speed, the highest level of maximum principal strain from the cracked elements is still within the strain-hardening domain of UHPFRC, i.e., lower than 1750μ, at the end of stage 2 from fatigue analysis, thanks to the autogenous self-healing of cracked UHPFRC under surface water condition from the beginning of this stage. For stage 2, it can be indicated that the fatigue degradation in the composite bridge deck is mainly dominated by the bridging stress degradation of cracked elements on top surface of the overlay. The development of the crack region on top layer of UHPFRC in this stage is thus insignificant in comparison to that from stage 1, due to the small expansion of the interfacial delamination area.

5.5 Summary

In this chapter, the fatigue behaviors of the UHPFRC-steel composite bridge deck subjected to the moving wheel loading with rubber tire are subsequently investigated and evaluated under surface water condition, i.e., stage 2 of fatigue analysis. The self-healing behavior and the shortening of the fatigue life of the cracked UHPFRC due to the existence of stagnant water are considered in the analysis with the two assumed phases for UHPFRC material model.

Due to the self-healing of the fine cracks in the UHPFRC overlay, the mechanical recoveries of reloading stiffness and tensile strength from these cracks are obtained leading to the decreases in strain range level results in both steel plate and UHPFRC layer.

On the other hand, later under the moving wheel loading, the fatigue degradation in the UHPFRC cracks may be accelerated due to the existence of stagnant water. By considering a higher speed of the bridging stress degradation in cracked UHPFRC, it is found that the analytical strain range results of steel deck plate exhibit an acceptable agreement in tendency in comparison to those from the experiment. Therefore, it can be

stated that the assumed behaviors for the material model of cracked UHPFRC in the analysis are reasonable for reproducing the experiment.

However, due to the neglect of the permanent bond slip at the UHPFRC/steel interface, the unloading strain levels in the steel deck plate may be underestimated in the analysis. This is also a topic for future studies of the composite bridge deck under moving wheel load.

CHAPTER 6   FATIGUE ANALYSIS OF THE UHPFRC-STEEL COMPOSITE BRIGDE DECK SUBJECTED TO A MOVING LOADING WITH STEEL WHEEL UNDER DRY CONDITION

6.1 Introduction

To accelerate the fatigue deterioration of the orthotropic steel bridge deck reinforced with UHPFRC overlay after the stages 1 and 2, the loading condition in the fatigue test was switched from the rubber tire wheel to steel wheel along with the increase in loading levels, as shown in Figure 6.1. In stage 3, the composite bridge deck is examined under dry condition.

In this chapter, the fatigue analysis of the UHPFRC-steel composite bridge deck in stage 3 under a moving wheel loading with steel wheel is carried out. The bridging stress degradation relation for dry condition is applied in the analysis. Two sub-stages corresponding to the applied wheel load levels, i.e., 150 kN in sub-stage 3-1 and 200 kN in sub-stage 3-2, are considered in this stage. The fatigue behaviors, i.e., displacement and strain in steel deck plate and UHPFRC reinforcing overlay, from each sub-stage are then investigated numerically by the analytical model.

Figure 6.1 Fatigue test of UHPFRC-steel composite bridge deck in stage 3 subjected to a moving loading with steel wheel under dry condition. [9]

6.2 Boundary conditions in the finite element model of the composite bridge deck under a moving loading with steel wheel

The boundary conditions and mesh pattern from the FEM model of the UHPFRC-steel composite deck under the wheel loading with steel wheel are shown in Figure 6.2. Four
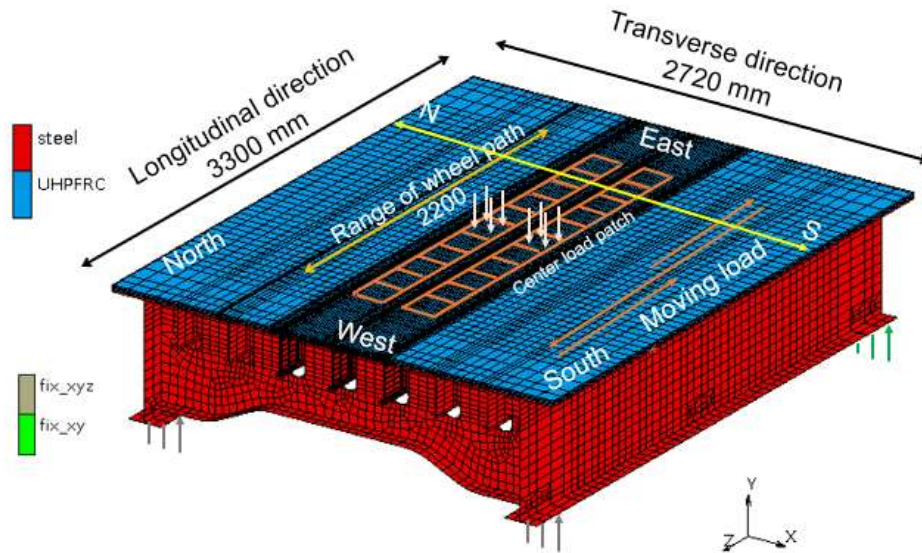
Figure 6.2 FEM model of UHPFRC-steel composite deck subjected to moving loading with steel wheel
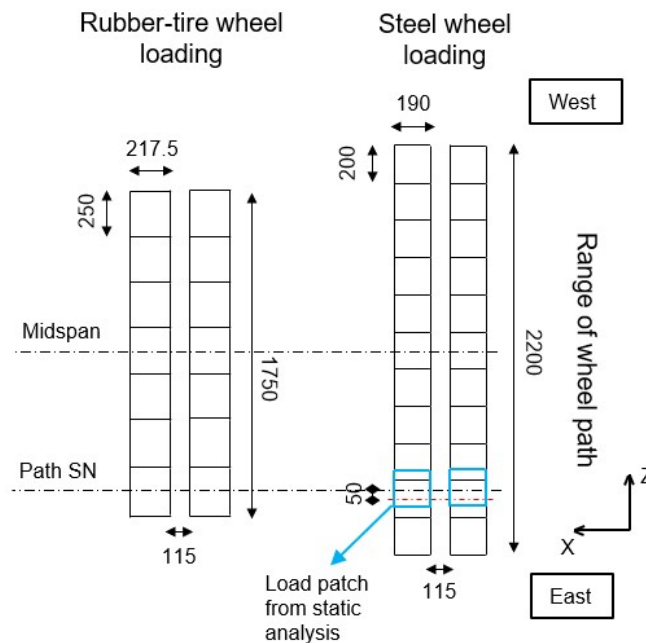
Figure 6.3 Range of wheel path from the loadings with rubber tire and steel wheel

edges under the flanges of the main girders are simply supported on a span of 3000 mm in longitudinal direction. Two West-edges are restricted in all three translational directions. The other edges from East side are constrained from translations in X and Y directions. The lane pattern of the steel wheel loading in this stage is simulated as 2 paths along the longitudinal direction with a range of ± 1100 mm from the midspan. The distance between two loading paths is 115 mm, which represents the gap between the supporting steel plates under the steel wheel in the experiment. The steel wheel loading is simulated by a sequence of eleven uniformly distributed loads with a size of 2×190×200 mm, as illustrated in Figure 6.3. The load levels of the steel wheel are assigned to be 150 and 200 kN for sub-stages 3-1 and 3-2, respectively, in the analysis. As can be seen from Figure 6.3, the centerline of the steel wheel load patch is not consistent with that of the rubber tire load patch. Therefore, to obtain the strain results from the strain gauges along path SN, the additional static analysis is conducted for each loading cycle in stage 3, in which the centerline of the steel wheel load patch coincides with path SN (Figure 6.3). For convenience, the steel wheel load applied at the above load patch from the static analysis is named as Load E-St (East-Static) in this stage from now on.

6.3 Procedure of fatigue analysis subjected to a moving loading with steel wheel

Similar to the case of moving loading with rubber tire, the wheel load with rubber tire is firstly applied at the Center load patch (load case 1) in the fatigue analysis. These elements are then unloaded after reaching the peak value (i.e., 150 kN for sub-stage 3-1 or 200 kN for sub-stage 3-2) simultaneously with the loading process of the adjacent elements (load case 2) with the same increasing rate, as shown in Figure 6.4. This procedure is continuously applied along the loading lane reproducing the moving process of the wheel loading. One cycle of fatigue analysis including a total of twenty-one load cases is finally completed at the Center patch position again. Throughout the wheel load moving process, the bridging stress degradation equation, as well as the unloading behavior, at each node of smeared crack elements in UHPFRC is modified based on the recorded maximum tensile strain from the previous cycle of fatigue analysis.

In stage 3, the bridging stress degradation relation for dry condition is applied in fatigue analysis as follows

$$\frac{\sigma_N}{\sigma_{1,160,001}} = 1 - (0.015 + 5\varepsilon_{t\max})\log(N - 1,160,000)$$ (6.1)

$$\text{for } 1,160,001 \le N \le 1,330,000$$

where ε_{tmax} is maximum tensile strain

N is number of loading cycles

$\sigma_N/\sigma_{1,160,001}$ is bridging stress degradation ratio between the N_{th} and the 1,160,001st cycles.

The tensile strength of UHPFRC is then modified based on Equation (6.1) that causes appearance of new cracks in the UHPFRC reinforcing overlay. The procedure is continued until the number of cycles reaches 1,330,000 when the fatigue test of the composite bridge deck in stage 3 completes. For this stage, the determination of the number of loading cycles used in the test is similar to Section 4.2. When the fatigue test is performed with a steel wheel load of 200 kN, the calculated number of 160,000 loading cycles can give a load that is equivalent to the 118-year design traffic load for only stage 3 [9].
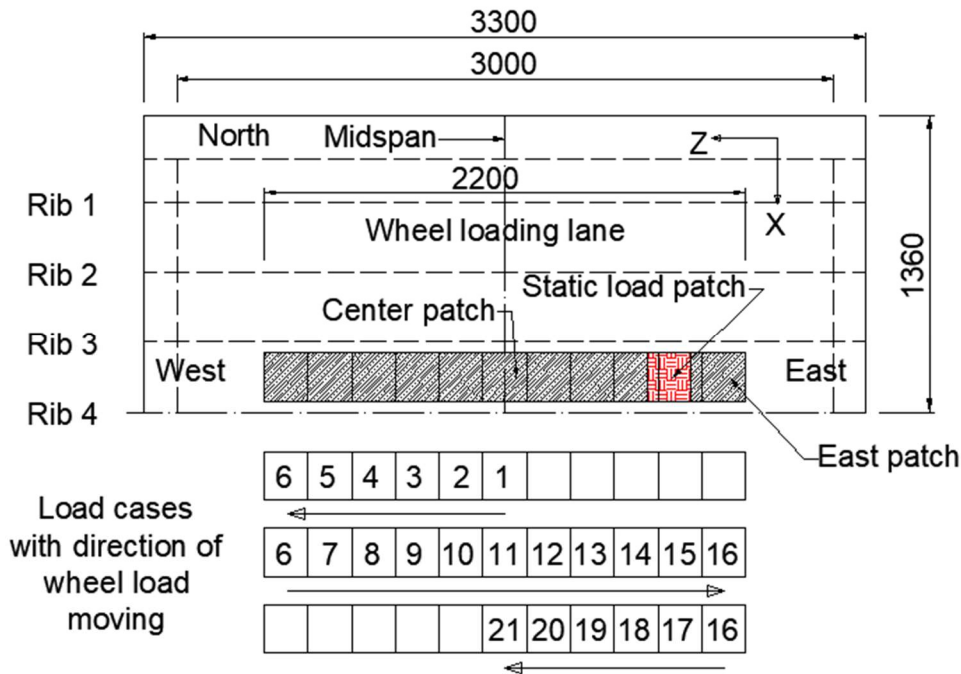
Figure 6.4 Load cases in accordance with the direction of the wheel load moving

6.4 Scenarios of the interfacial bond degradation for fatigue analysis

In stage 3 of fatigue analysis, the expansion of the interfacial delamination area based on the experimental observations, i.e., hammer tapping test and strain in steel deck plate, is continued to be assumed to govern the fatigue damage at the bond layer. The speed of expansion for each sub-stage are presented in the following sections.

6.4.1 The expansion of interfacial delamination area from 1,160,001st to 1,170,000th cycles in sub-stage 3-1 under load level of 150 kN

In sub-stage 3-1, due to the lack of information about hammer test results at the end of this condition, the delamination area for this sub-stage is limited within the delamination area at the end of sub-stage 3-2 (at 1,330,000th cycle). As can be seen from Figure 6.5, due to the expansion in longitudinal direction of loading path under steel wheel, the delamination region obtained from the hammer test also expanded in

(a) At 1,160,000th or 1,160,001st cycle   (b) At 1,170,000th cycle
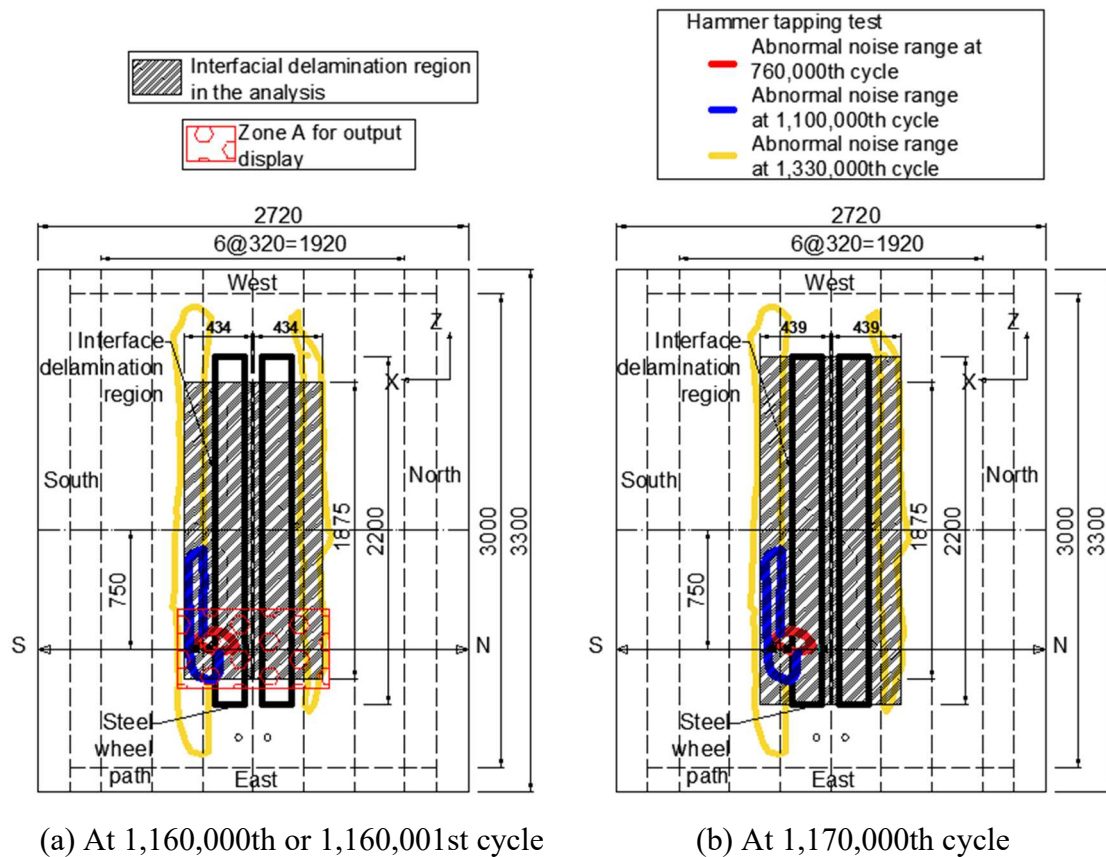
Figure 6.5 Interfacial delamination region for different cycles in sub-stage 3-1

longitudinal direction. In this sub-stage, the total expansion of 10 mm in transverse direction is simply applied in the analysis, in which the expansion speed is twice of that from stage 2. For longitudinal direction, the debonding area is gradually expanded with a speed of 325 mm per 10,000 cycles. The interfacial delamination region at the end of this sub-stage (1,170,000th cycle) is shown in Figure 6.5(b), where the longitudinal dimension of this region is chosen equal to that of the loading lane.

6.4.2 The expansion of interfacial delamination area from 1,170,001st to 1,330,000th cycles in sub-stage 3-2 under load level of 200 kN

In sub-stage 3-2, based on the hammer test results at the end of this condition (at 1,330,000th cycle), the progressive expansion of the interfacial delamination area is applied in the analysis as follows

- From the 1,170,001st to 1,190,000th: the constant speeds of 60 mm/20,000 cycles in

(a) At 1,170,000th or 1,170,001st cycle   (b) At 1,330,000th cycle
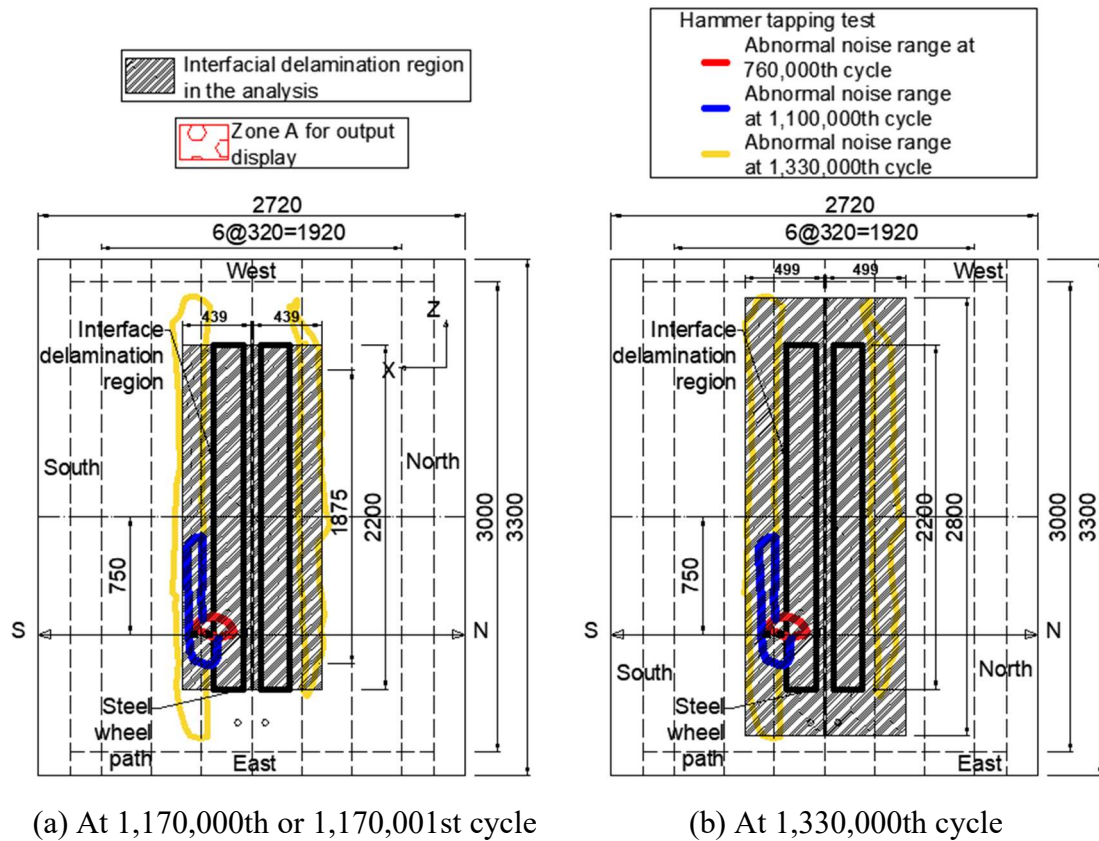
Figure 6.6 Interfacial delamination region for different cycles in sub-stage 3-2

transverse direction and 300 mm/20,000 cycles in longitudinal direction are applied to the expansion of debonding area.

- From the 1,190,001st to 1,300,000th: the slower speeds of delamination area expansion are applied in the analysis, which are chosen to be 60 mm/140,000 cycles for transverse direction and 300 mm/140 cycles for longitudinal direction.

As shown, in Figure 6.6 (b), at the 1,330,000th cycle, the interfacial delamination area is 2×499 (transverse)×2800 mm (longitudinal) in the current model. The debonding area in the analysis is relatively compatible with the results from the hammer tapping test.

6.5 Results and discussions

6.5.1 Displacement results

Figure 6.7 shows the vertical displacement distribution from the bottom of steel deck plate under Load E-St for different cycles from the stages 2 and 3 of fatigue analysis. The results from sub-stage 3-1 are presented by Figures 6.7(b) and (c), while Figures 6.7(d) and (e) represent the displacement results from sub-stage 3-2. It can be seen that the magnitude of displacement in steel bridge deck increases with the increase of the number of loading cycles. From Figure 6.7, it can be seen that the vertical displacements of steel deck plate significantly increase when the load levels increase from stage 2 (100 kN) to sub-stage 3-1 (150 kN), and from sub-stage 3-1 to sub-stage 3-2 (200 kN). Throughout each sub-stage, the displacement levels gradually increase owing to the continuous loss in composite action between reinforcing overlay and steel plate when the interfacial delamination region is expanded in both longitudinal and transverse directions.

Figure 6.8 represents the relationship between the maximum levels of vertical displacement obtained in the bridge deck under Load E-St in the analysis and the number of loading cycles in comparison to experimental results. From Figure 6.8, despite the lower level of applied load, the larger increases in experimental displacement magnitudes are obtained from the sub-stage 3-1 compared to those from sub-stage 3-2. This may be because the vertical deformation from the supporting steel beams under the main girders (as discussed in Section 3.4.1) has mostly happened in the sub-stage 3-1 of the experiment when the load condition was shifted from rubber tire wheel to steel wheel. For each

(a) At the 1,160,000th cycle (stage 2, 100 kN)
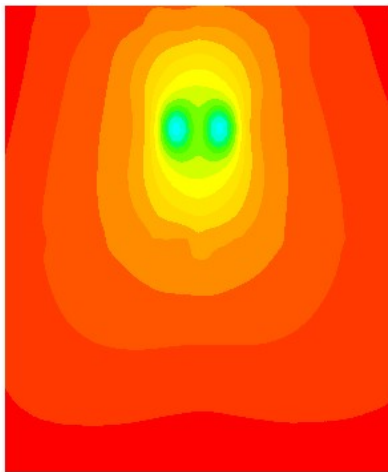
(b) At the 1,160,001st cycle (150 kN)　　(c) At the 1,170,000th cycle (150 kN)
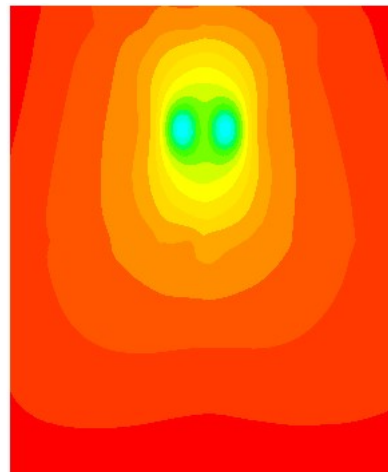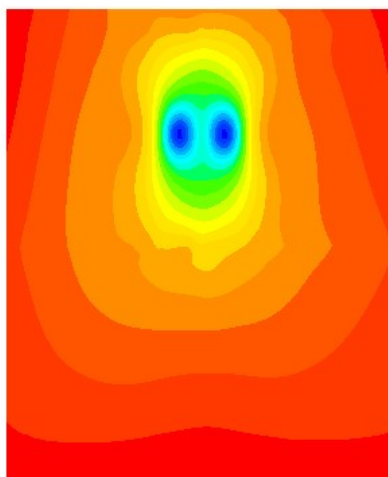
(d) At the 1,170,001st cycle (200 kN)　　(e) At the 1,330,000th cycle (200 kN)
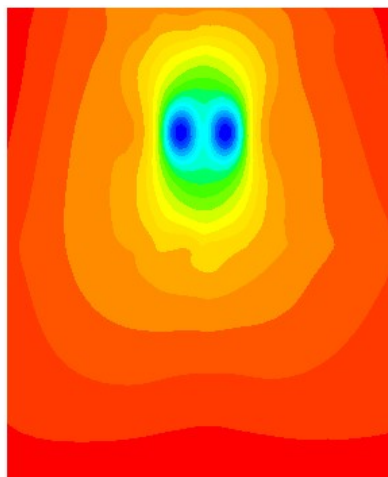
Figure 6.7 Vertical displacement distribution under bottom of the steel deck plate for different cycles from the stage 3 of fatigue analysis.
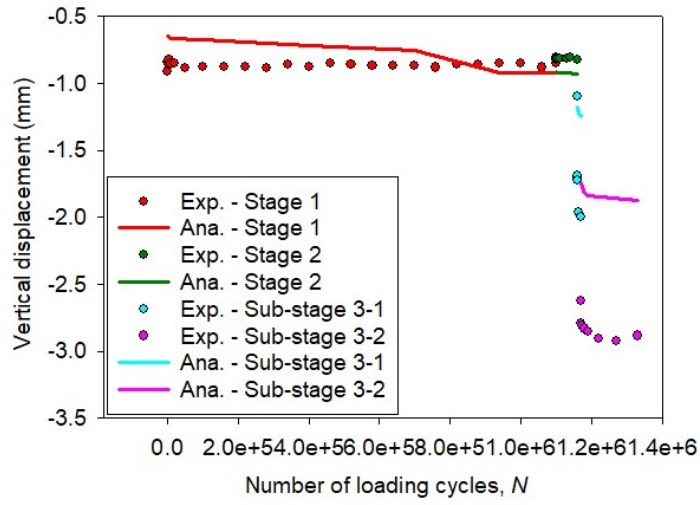
(a) Stages 1, 2 and 3
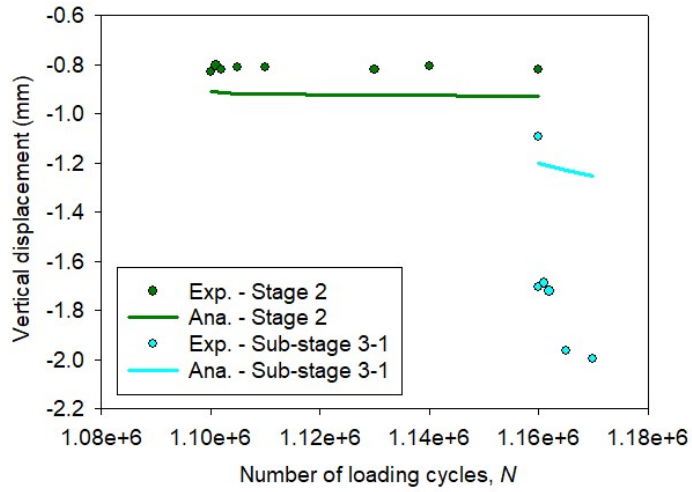
(b) Stage 2 and sub-stage 3-1
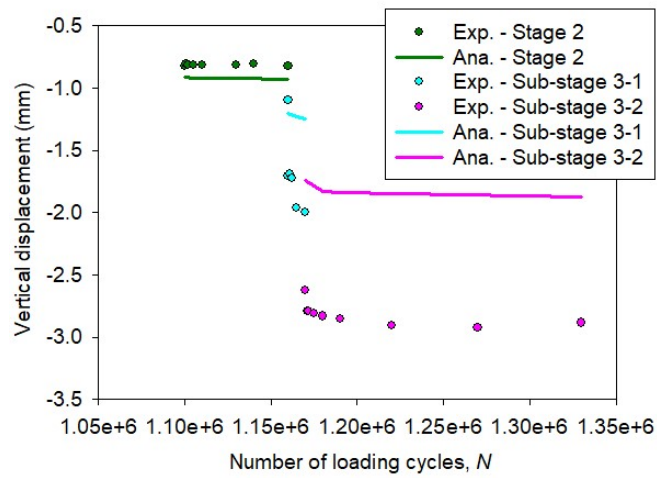
(c) Stage 2 and stage 3

Figure 6.8 Maximum vertical displacement results from stage 3 of fatigue analysis.

increasing step of loading level, it is obvious that there are the considerable increases in vertical displacement results obtained from the analytical model. As shown in Figure 6.8(c), for sub-stage 3-2, the tendency of the analytical displacement results relatively agrees with that from experimental data.

6.5.2 Strain results in steel deck plate

The transverse strain distributions in the steel deck for different cycles from each sub-stage under Load E-St are plotted in Figure 6.9. Due to the progressive loss in the capability of shear force transferring caused by the expansion of the interfacial debonded area, the deformations of the composite bridge deck significantly increase with the increase of the number of loading cycles, especially when the applied load level of the steel wheel increases from the 1,160,000th to 1,160,001st cycles or from the 1,170,000th to the 1,170,001st cycles. As a result, it is apparent that the strain levels in steel deck plate at the longitudinal ribs as well as the contact regions of wheel loading continuously increase due to the gradual decrease in overall stiffness of the composite deck. At the end of sub-stage 3-2, the compressive zones at the regions above Ribs 3 and 5 are markedly expanded due to the relatively large expansion in transverse direction of the delamination area in this sub-stage.

Along with the fatigue damage at the interface between UHPFRC reinforcing overlay and the steel deck plate, the bridging stress degradation of cracked UHPFRC which is dependent on the level of maximum tensile strain is notably accelerated under the moving loading with steel wheel (see Equation (6.1)).

In reverse, the stress redistribution caused by fatigue bridging stress degradation in UHPFRC cracks may also cause more contact stress at the interface, leading to the development of the interfacial debonded area. The mutual interaction of these two kinds of fatigue deteriorations may significantly degrade the structural performance of the UHPFRC-steel composite bridge deck subjected to repetitive moving loadings.

(a) At the 1,160,000th loading cycle (100 kN)

(b) At the 1,160,001st loading cycle (150 kN)

(c) At the 1,170,000th loading cycle (150 kN)

(d) At the 1,170,001st loading cycle (200 kN)

(e) At the 1,330,000th loading cycle (200 kN)
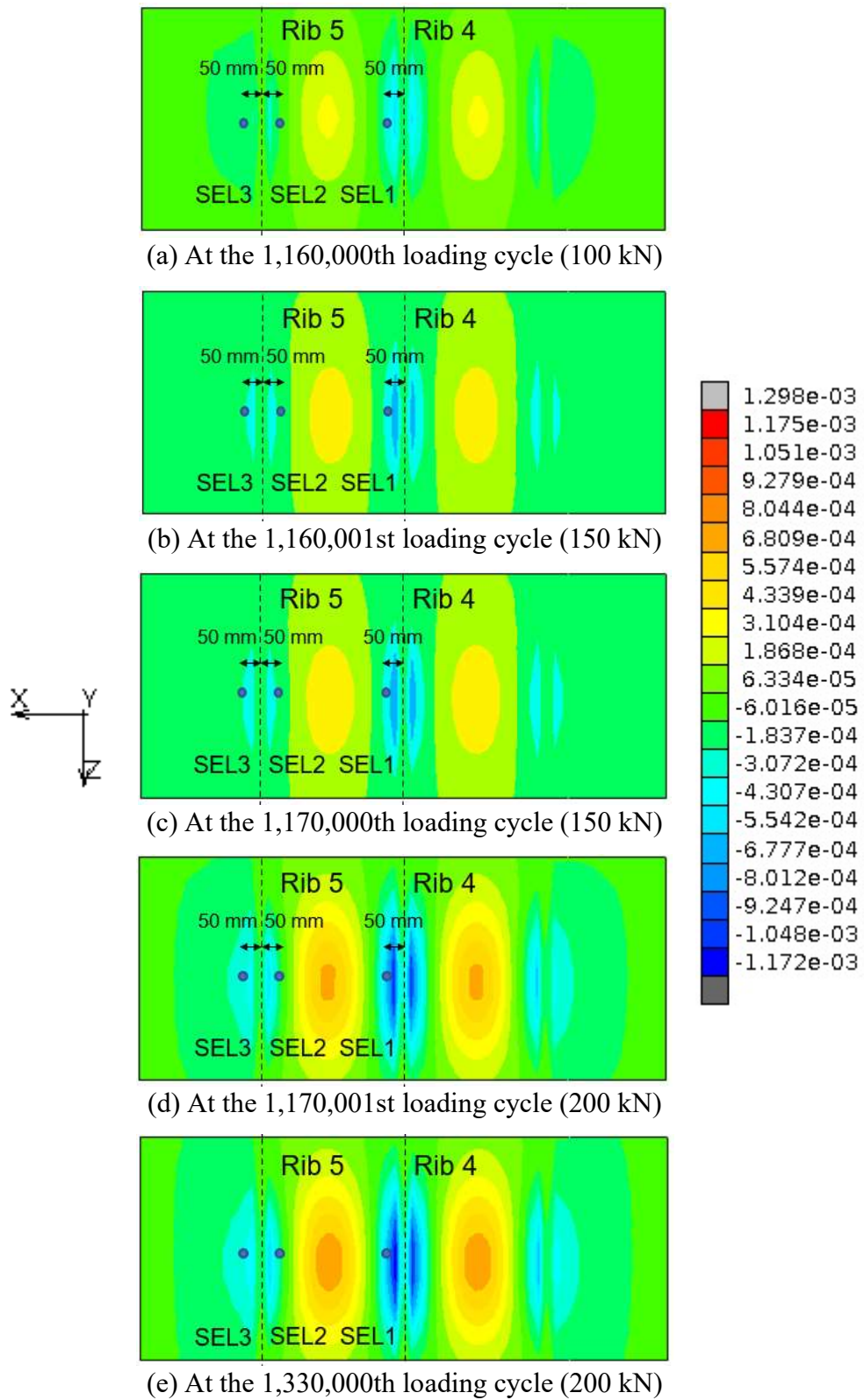
Figure 6.9 Transverse strain distributions in steel deck plate versus the number of loading cycles at zone A under Load E-St

From Figures 6.10 to 6.12, the transverse strain range evolutions under load case 10 (for stages 1 and 2) or Load E-St (for stage 3) obtained from the positions of the strain gauges SEL1, SEL2 and SEL3 are plotted in comparison to the data from the experiment.

In Figure 6.10, there is an increase in strain level at the beginning of the steel wheel condition (at 1,160,001st cycle) due to the increase in applied load level from 100 to 150 kN. Similarly, at the 1,170,001st cycle, the transverse strain range magnitude also increase at SEL1 as the load level increases to 200 kN. The considerable increase in strain range results throughout the stages 3 is caused by two reasons. The first one is that the bridging stress degradation in cracked UHPFRC is speeded up with the increases of not only applied load level but also the range of wheel path (from 1875mm to 2200mm), leading to the development in both transverse and longitudinal directions of cracked region in UHPFRC. Another reason is the increasing range in longitudinal direction of wheel path also causes the longitudinal expansion of the interfacial delamination area, leading to the considerable loss in composite action between UHPFRC and steel deck plate.

Comparing the models with and without the expansion of the delamination area at the interface, it is found that the effect of interfacial degradation on steel strains for both sub-stages 3-1 and 3-2 is dominant in the composite deck comparatively with that of bridging stress degradation in cracked UHPFRC, due to the slow speed of bridging stress degradation of UHPFRC cracks under dry condition, as shown in Figure 6.10(c).

For point SEL2, as can be seen from Figure 6.11(b), there is a decrease in strain range result at the 1,160,001st cycle from sub-stage 3-1. This may be due to the shortening of transverse dimension of the applied load region from 220mm to 190mm, as shown in Figure 6.13. This leads to the lesser positive bending obtained at the local region right above the position of strain gauge SEL2, leading to the observed decreasing tendency in transverse strain range at this point. As discussed in Section 4.4.2, it is known that the strain results at SEL2 are sensitive and affected by two regions: one is right under applied wheel load, another is above the longitudinal rib (Rib 5). When the interfacial delamination occurs at the former region, the more positive bending and the narrowing of the tensile regions at this region are obtained leading to the decreasing tendency at

SEL2. Similarly, more negative bending at the Rib 5 can be observed with a smaller compressive zone when the interfacial debonding happens in this region, causing the increase in transverse strain at SEL2. Throughout sub-stage 3-1 under wheel load of 150 kN, the effect from Ribs 5 may be dominant due to the shortening in transverse dimension of applied wheel load. However, when the load level increases to 200 kN in sub-stage 3-2, the positive bending at the wheel load contact region has increased and governed the strain results at SEL2. This leads to the reverse tendency obtained from sub-stage 3-2 in comparison to that from sub-stage 3-1, as shown in Figure 6.11(c).

Overall, the strain range results in the steel deck plate exhibit an acceptable agreement with those from the experiment for both sub-stages 3-1 and 3-2. In sub-stage 3-2, two expansion speeds of the interfacial delamination area are used in the analysis, as presented in Section 6.4.2. This can be explained by the contact shear stress distributions at the interface from the 1,170,001st and the 1,190,000th cycles, as shown Figure 6.14. It can be seen that the maximum level of interfacial contact shear stress obtained from the 1,170,001st cycle is higher than that from the 1,190,000th cycle. After the expansion of the debonded area, the edges of this area from the 1,190,000th cycle are relatively far from the loading region of steel wheel. Therefore, the contact shear stresses caused by the wheel load which is mostly distributed at the debonded area's edges at this cycle are much lesser than that from the 1,170,001st cycle, leading to the slower expansion speed from the delamination area from the 1,190,000th cycle. Since the trends from the experimental data were reproduced rationally well by the analytical model, it can be indicated that the assumed scenarios with the different expansion speeds of interfacial debonding area have probably happened in the experiment of the UHPFRC/steel composite deck.

At the end of this stage, no crack has been found in the steel members of OSD from the fatigue test of the composite bridge deck. This indicates that the UHPFRC overlay can still maintain the strengthening effect at the critical locations in the steel deck plate after the severe conditions of the moving loadings and the environments, even when a part of the overlay delaminated from the steel bridge deck (about 31% of deck area in the analysis).
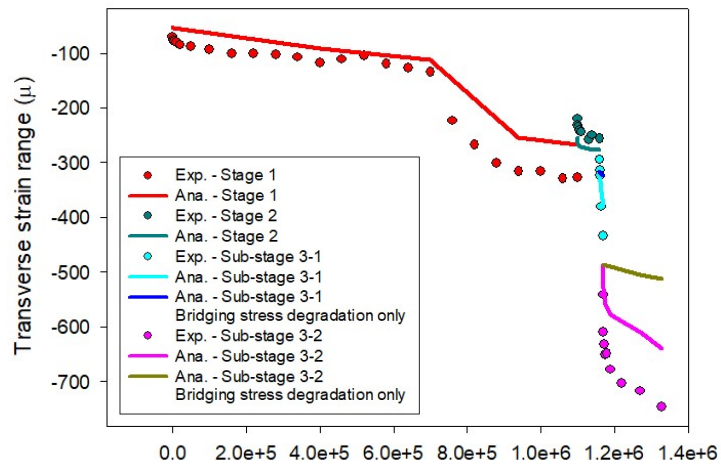
(a) Stages 1, 2 and 3
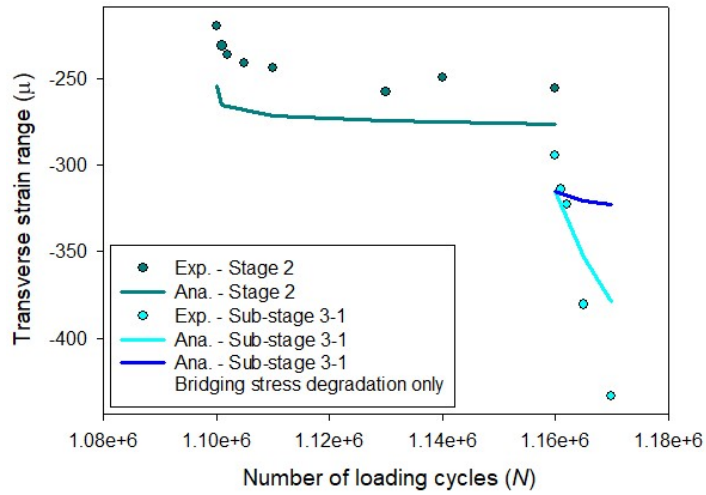
(b) Stage 2 and sub-stage 3-1
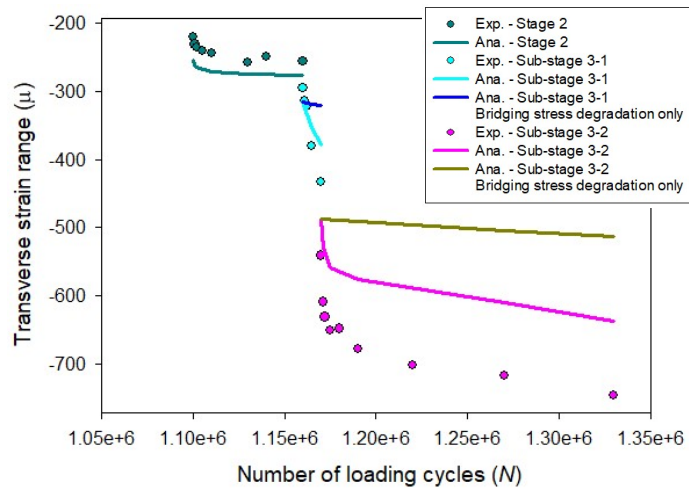
(c) Stage 2 and stage 3

Figure 6.10 Transverse strain range evolutions at strain gauge SEL1

109
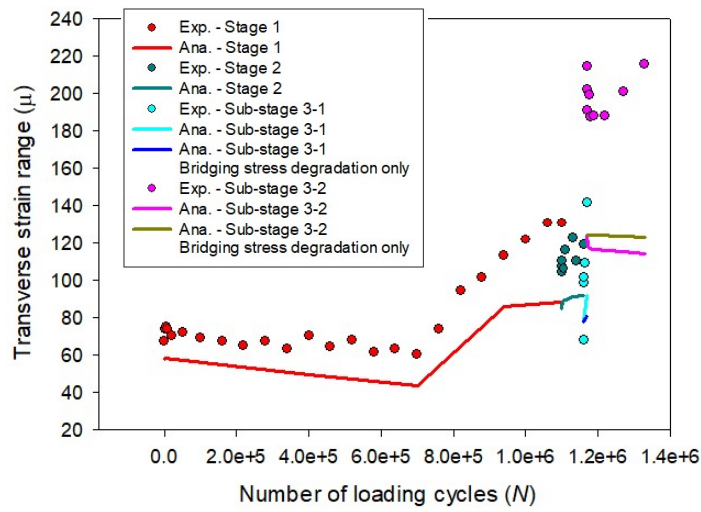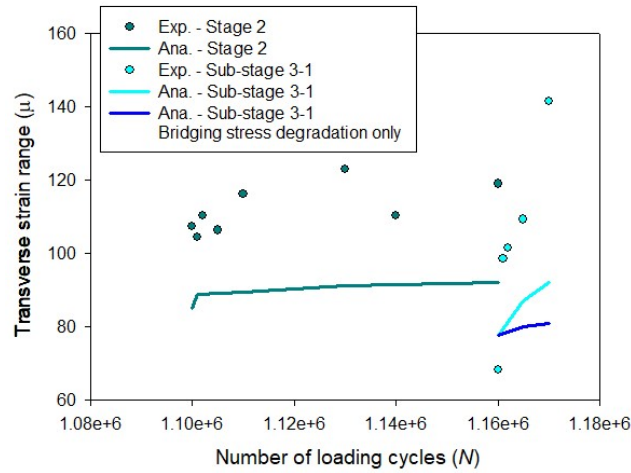
(a) Stages 1, 2 and 3

(b) Stage 2 and sub-stage 3-1
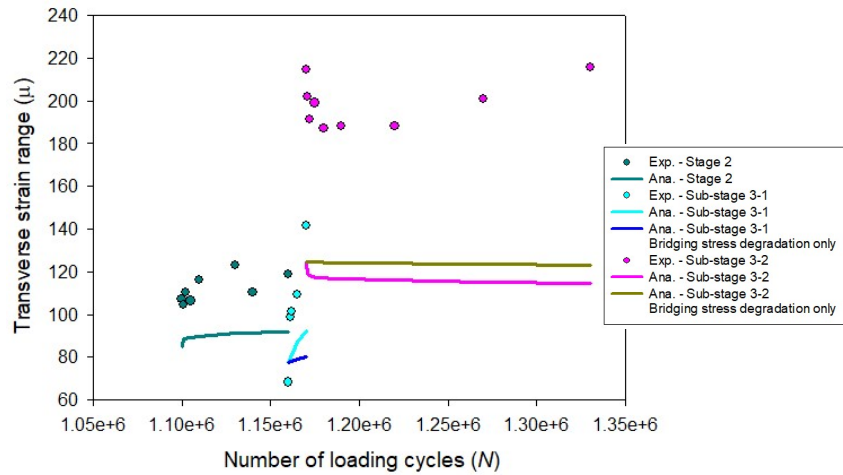
(c) Stage 2 and stage 3

Figure 6.11 Transverse strain range evolutions at strain gauge SEL2
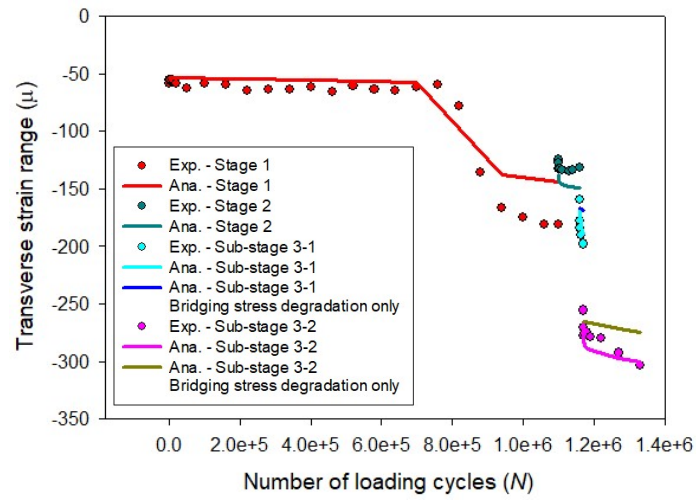
(a) Stages 1, 2 and 3
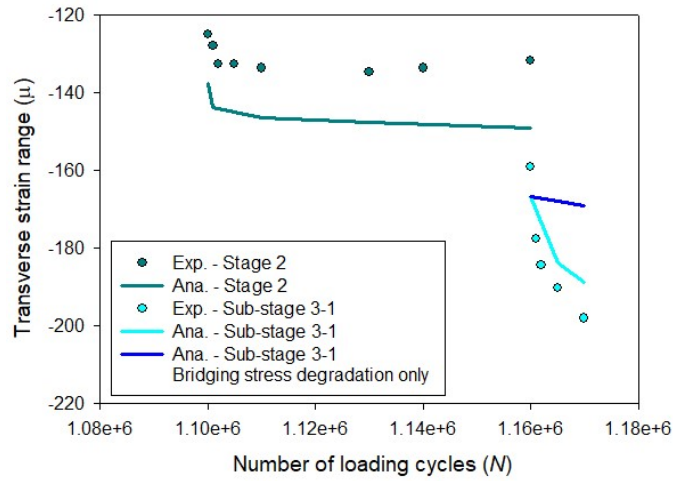
(b) Stage 2 and sub-stage 3-1
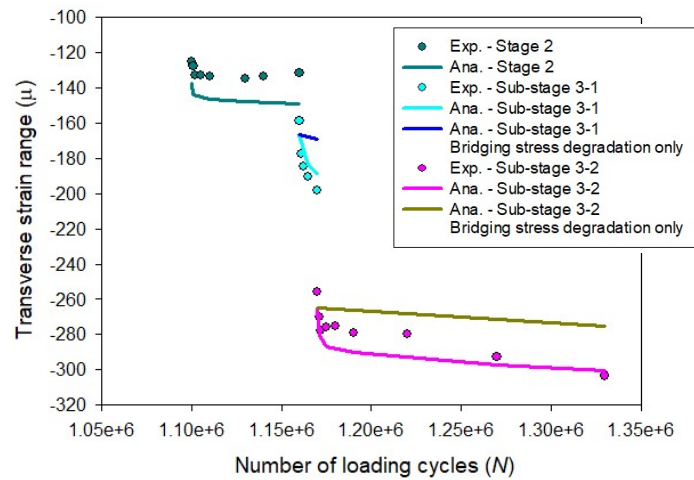
(c) Stage 2 and stage 3

Figure 6.12 Transverse strain range evolutions at strain gauge SEL3
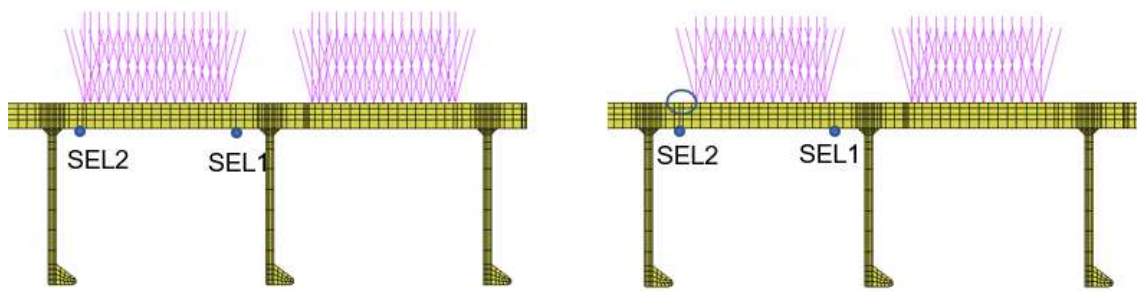
(a) Rubber tire wheel loading   (b) Steel wheel loading

Figure 6.13 Transverse dimensions of the applied load region from the different loading condition
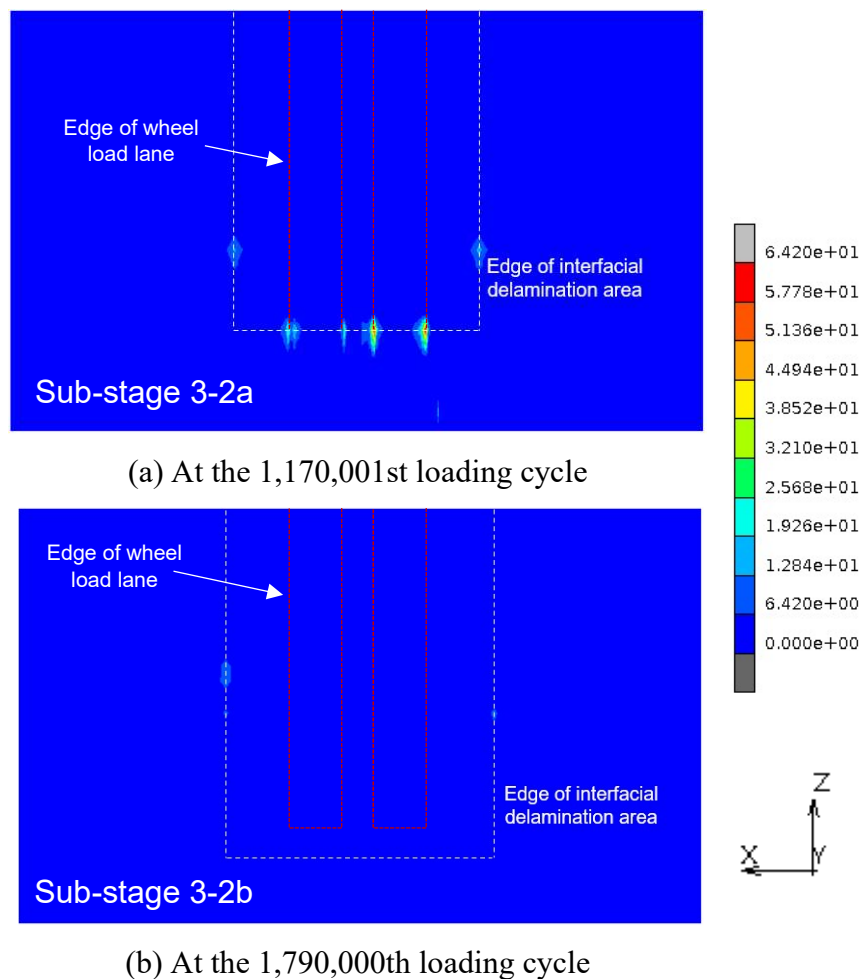
(a) At the 1,170,001st loading cycle

(b) At the 1,790,000th loading cycle

Figure 6.14 Interfacial contact shear stress in sub-stage 3-2 of the analysis

6.5.3 Strain results in UHPFRC overlay

Figure 6.15 shows the maximum strain distributions from the cracked elements obtained on the top and bottom layers of UHPFRC overlay from the different loading cycles under load case 10 (for stage 2) or Load E-St (for stage 3). The strain results are displayed in zone A (see Figure 6.5). The cracked regions on UHPFRC surface are represented by the band from blue to red colors. It is obvious that the tensile strain levels at the longitudinal ribs from top layer as well as the contact region of wheel load from bottom layer increase with the increase of the number of loading cycles. From the 1,160,000th to 1,160,001st cycles, due to the increase of load level from 100 kN to 150 kN, the marked development of the cracked region can be observed from the analytical model. Similar observation is aslo obtained from the 1,170,000th to 1,170,001st cycles in the analysis due to the increase of steel wheel load to 200 kN. Throughout sub-stage 3-1 (from 1,160,001st to 1,170,000th cycles) or sub-stage 3-2 (from 1,170,001st to 1,330,000th cycles), the changes in cracked area are insignificant, and only the increases in strain levels from the cracked region are observed due to the continuous expansion of the delamination area at UHPFRC/steel interface and the bridging stress degradation of UHPFRC cracks. It is known from the analysis that the development of cracked region in UHPFRC overlay is mostly dependent on the applied load level of steel wheel. In sub-stage 3-2, under load level of 200 kN, it can be seen that the tensile cracks has propagated from the bottom layer to top layer at the wheel load contact region, as can be seen from Figures 6.15(d) and 6.15(e).

The principal tensile strain distributions on top surface of UHPFRC overlay for the different load cases of moving loading with rubber tire wheel (at 1,160,000th cycle) and steel wheel (at 1,170,000th cycle and 1,330,000th cycle) are illustrated in Figures 6.16 and 6.17, respectively. The cracked regions are represented by gray color. The wheel loadings move from the East location (875mm from midspan for rubber tire, 1100mm from midspan for steel wheel) toward the Center load patch at midspan. As mentioned above, the cracked regions in UHPFRC layer are driven by the applied load level. In Figure 6.17, due to the increase in level of applied steel wheel load from 150 kN to 200 kN, the crack region significantly increases on top surface of UHPFRC layer for both the regions above the ribs 3,4 and 5, and applied regions of steel wheel loading between the

(a) At 1,160,000th cycle (stage 2, 100 kN)

(b) At 1,160,001st cycle (sub-stage 3-1, 150 kN)

(c) At 1,170,000th cycle (sub-stage 3-1, 150 kN)

(d) At 1,170,001st cycle (sub-stage 3-2, 200 kN)

(e) At 1,330,000th cycle (sub-stage 3-2, 200 kN)
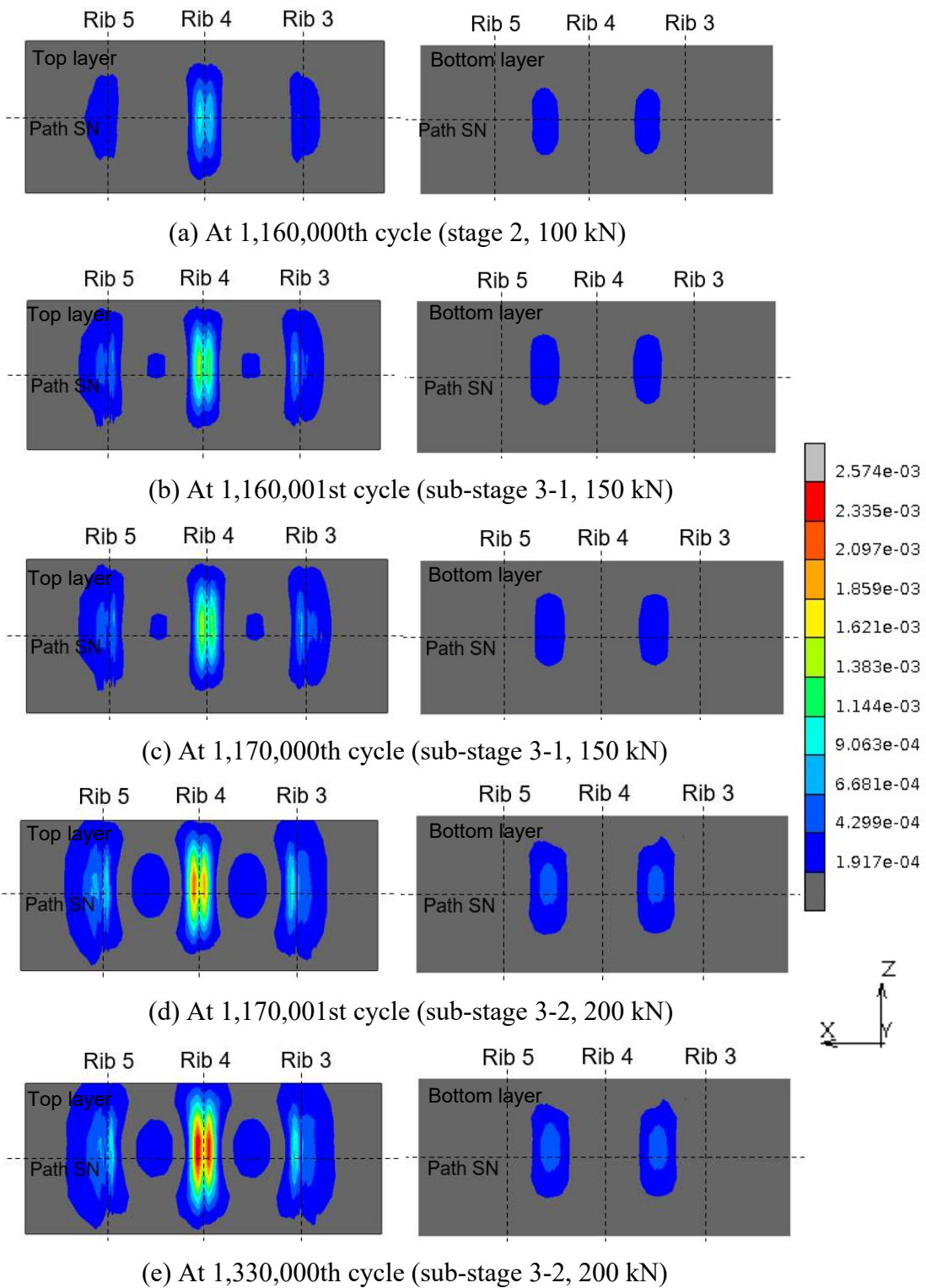
Figure 6.15 Maximum principal strain distributions from cracked areas under Load E-St on top and bottom layers of UHPFRC overlay

(a) Load case 10   (b) Load case 11

(c) Load case 12   (d) Load case 13
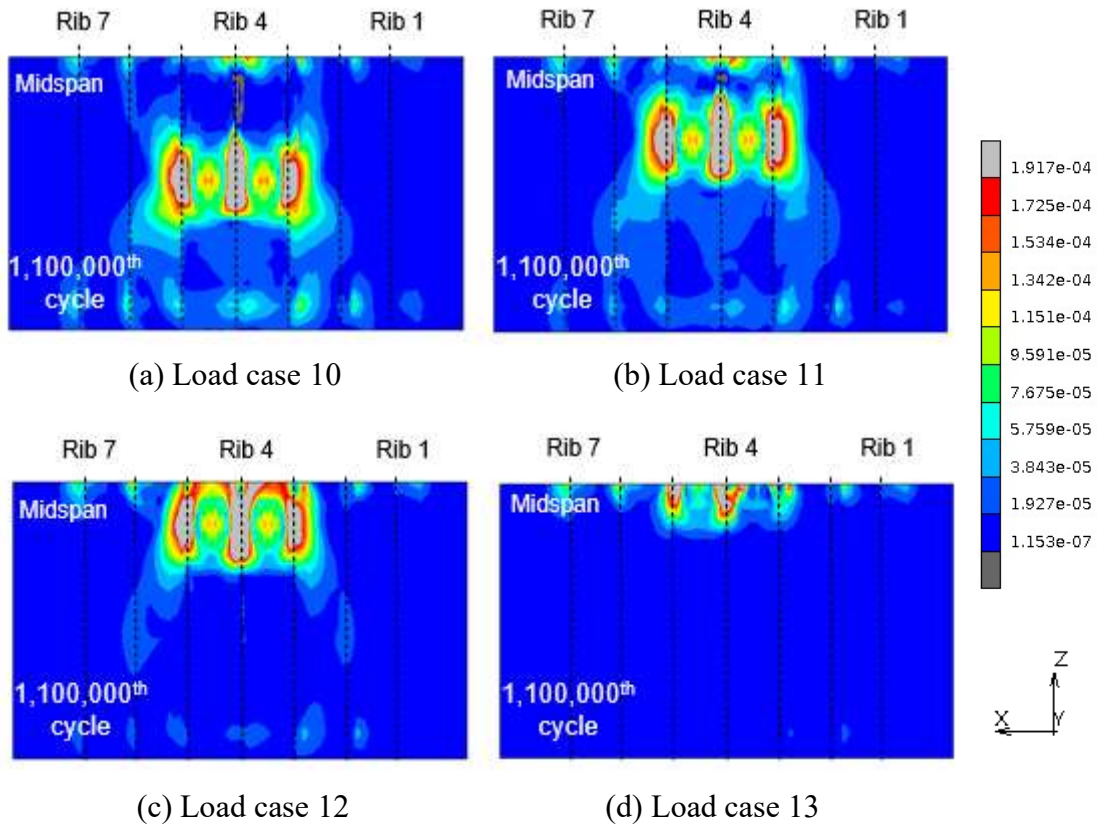
Figure 6.16 Maximum principal strain distributions for each load case of rubber tire wheel load on top layer of UHPFRC at the 1,160,000th cycle (Gray color: crack region)
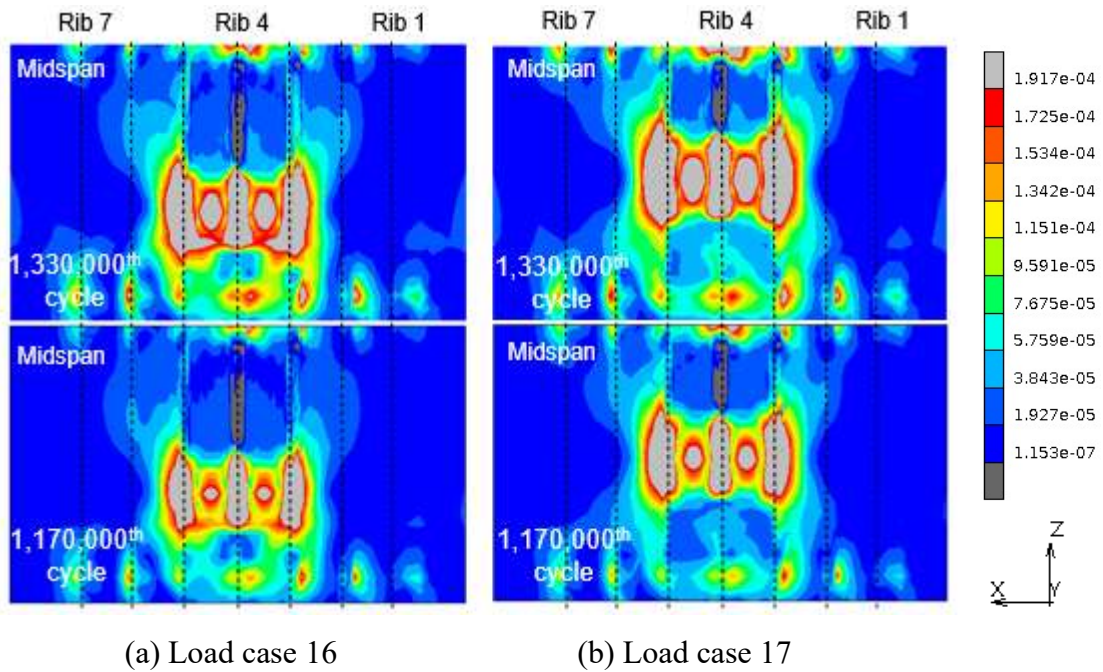
(a) Load case 16   (b) Load case 17

Figure 6.17 Maximum principal strain distributions for each load case of steel wheel load on top layer of UHPFRC at the 1,170,000th and 1,330,000th cycles

(c) Load case 18   (d) Load case 19

(e) Load case 20   (f) Load case 21
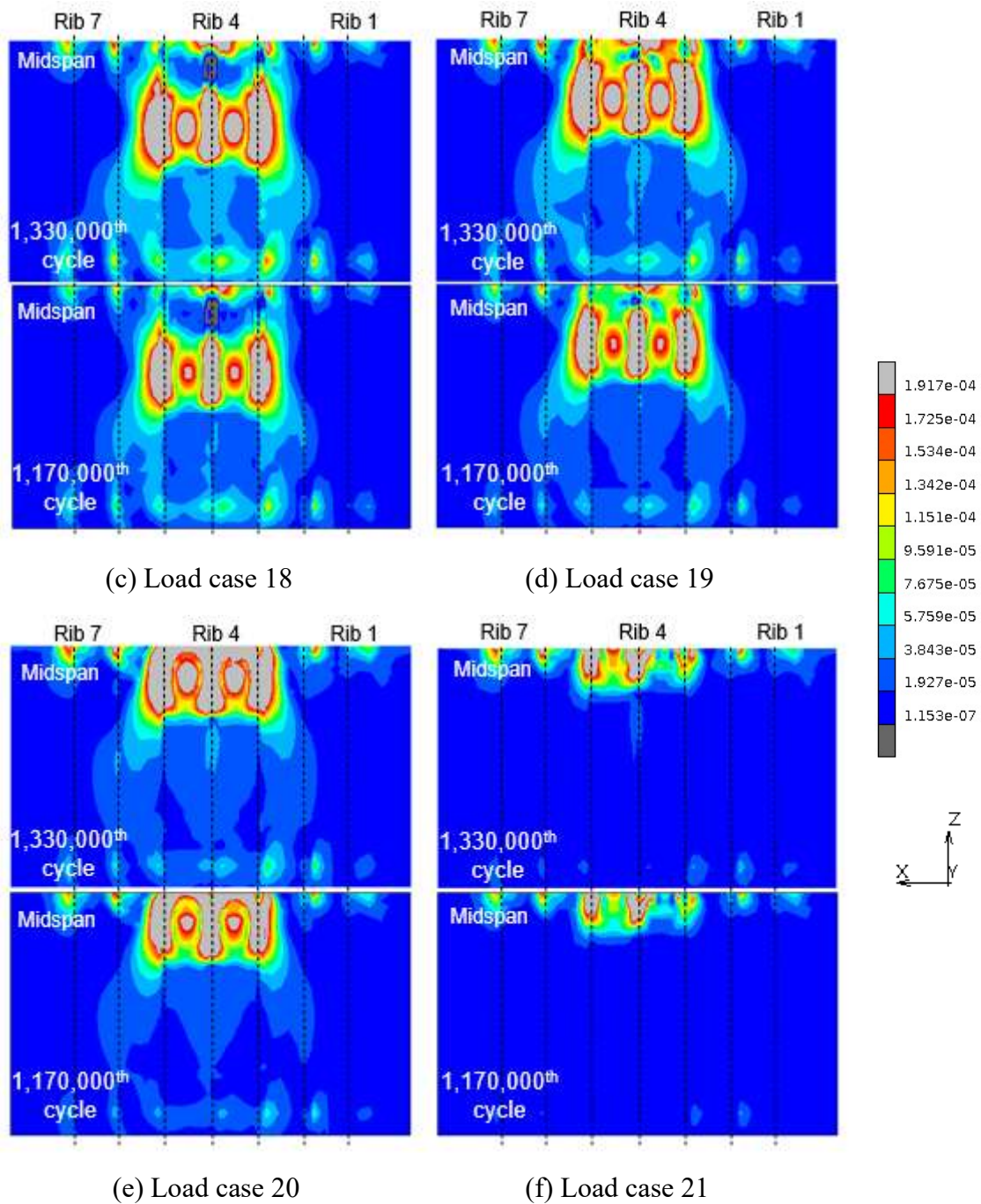
Figure 6.17 Maximum principal strain distributions for each load case of steel wheel
load on top layer of UHPFRC at the 1,170,000th and 1,330,000th cycles

ribs. From the analysis, the highest level of maximum principal strain on the top surface
of UHPFRC is obtained at the longitudinal middle rib (Rib 4) from load case 20 (see
Figure 6.17(e)). The reason is that the wheel load generates more negative bending

moment above the ribs at load case 20 due to the additional stiffening effect from the middle cross beam at the midspan.

Figure 6.18 presents the directions of maximum principal strains from the cracked elements obtained from the load case 17 at the midway between midspan. Since the steel wheel load produces the positive bending under the loading region, and the negative bending at the regions above the longitudinal Ribs 3, 4 and 5, the tensile cracks in UHPFRC can be observed from these regions. As can be seen from Figure 6.18, the longitudinal cracks above the ribs and the diagonal cracks under the wheel load region are obtained in the analysis, similar to the observations from the previous stages. At the end of stage 3, it is found that the localized cracks (i.e., the tensile strain is larger than 1750μ) have occurred at the local region above Rib 4 in the analysis, as can be observed

(a) Top layer

(b) Bottom layer
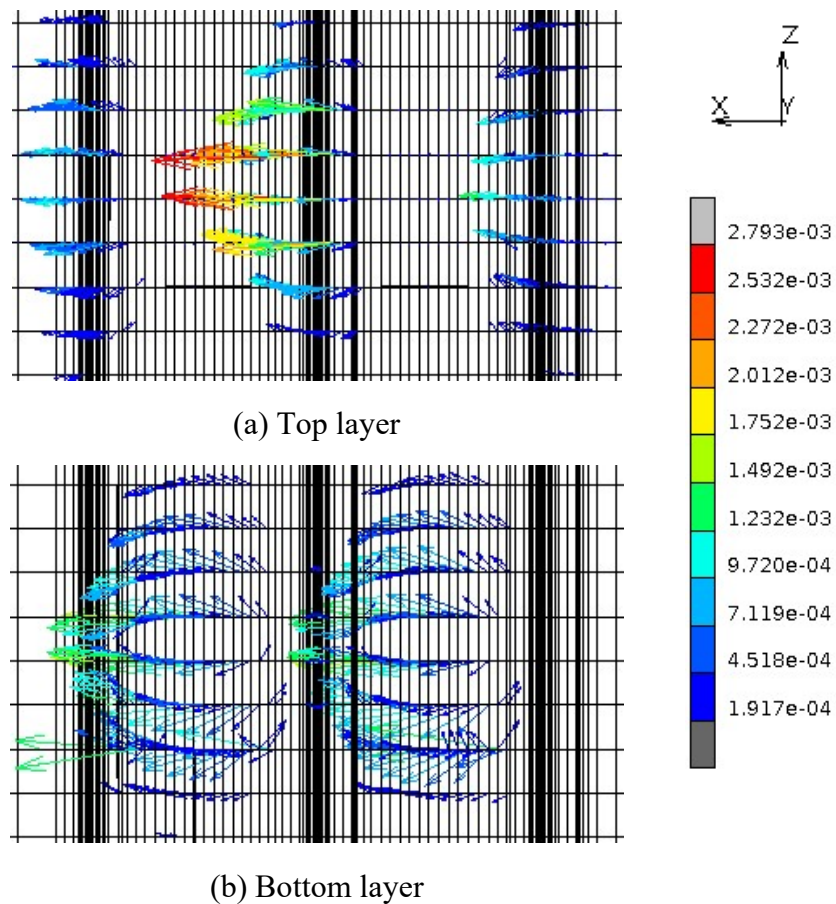
Figure 6.18 Direction of tensile maximum principal strain in UHPFRC overlay obtained from load case 17 at the 1,330,000th loading cycle.

in Figure 6.18(a). Figure 6.19 shows the crack pattern on top surface of UHPFRC overlay and the images of the sampled cores from the tensile bond test at the end of stage 3 in the experiment. From the crack pattern shown in Figure 6.19(a), there is no report of material separation in UHPFRC overlay at the end of this stage, and only the micro cracks are observed on the top surface of UHPFRC layer. The reason may be because the values of the cracking strength and tensile strength of UHPFRC material were underestimated in the analysis. These values from the real case of experiment may be much larger than those used in the analysis.
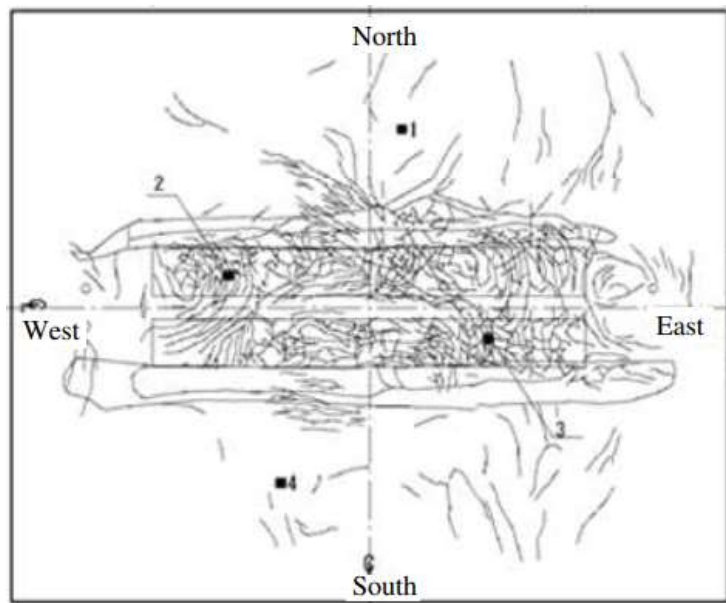
(a) Crack pattern and lositions of tensile bond test
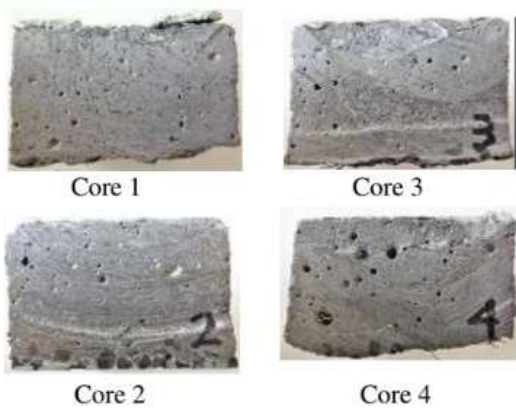
Results of tensile bond test

Sampling locations	Bond strength (N/mm^2)
1	2.77
2	0.00
3	0.84
4	3.57

(b) Cross-section of the sampled cores from the tensile bond test

Figure 6.19 Crack pattern and tensile bond test at the end of stage 3. [9]

Another issue is that the UHPFRC cracks in the experiment are mostly distributed on the top surface of the overlay. This may be due to the non-uniformly distribution of the steel fibers in the UHPFRC overlay. It has been reported from the experiment of UHPFRC flexural beams that the fiber contents near the bottom surface of the specimens are higher than those from the upper parts [56]. Accordingly, for the case of UHPFRC overlay in the composite deck, the cracking strength as well as the tensile strength from the top layer of UHPFRC overlay may be lower than those from the middle and bottom layers. Further investigations of the composite bridge deck are needed to examine the effect of the material properties of UHPFRC material in the cracking behavior of the reinforcing overlay.

As can be observed in Figure 6.19(b), the bond strength at the location of core 3 is 0.84 N/mm². Hence, the interfacial bond layer at the contact regions of wheel loadings may not be delaminated totally as assumed in the analysis. This can be explained by the contact shear stress distribution at the first cycle in stage 1, as shown in Figure 6.20. It can be seen that the interfacial contact shear stresses at the adjacent regions of the longitudinal ribs are larger than those from the middle regions right under the tire contact zone. In other words, the degradation speed of interfacial bond stiffness around the longitudinal stiffeners may be faster than in the middle regions below the wheel load. But for the simplicity of the analytical model, only one interfacial degradation speed is applied in stage 1. Therefore, the interfacial bond stiffness degradation with the different speeds which depends on the contact bond stresses at the interface may be a topic for the future construction of the analytical model.
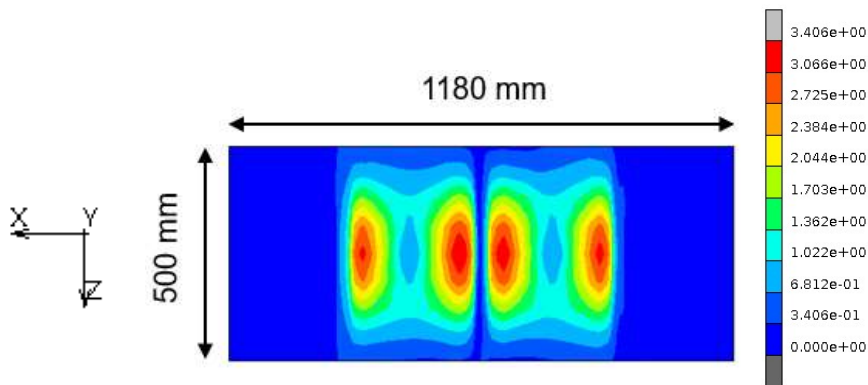
Figure 6.20 Contact shear stress at UHPFRC/steel interface from the first cycle

6.6 Summary

In stage 3, the loading condition in the fatigue test was switched from the rubber tire wheel to steel wheel along with the increase in loading levels to accelerate the fatigue deterioration of the composite bridge deck.

In this chapter, the fatigue analysis of the UHPFRC-steel composite bridge deck in stage 3 is carried out. The bridging stress degradation relation for dry condition is applied in the analysis of this stage. Two sub-stages corresponding to the applied wheel load levels, i.e., 150 kN in sub-stage 3-1 and 200 kN in sub-stage 3-2, are considered in this stage. The expansion of the interfacial delamination area based on the experimental observations, i.e., hammer tapping test and strain in steel deck plate, is continued to be assumed to govern the fatigue degradation at the interface bond layer.

It is found that, with the assumed scenarios with the different expansion speeds of interfacial debonding area for each sub-stage, the current analytical model could give an acceptable agreement in tendencies of the strain range results in the steel deck plate with those from the experiment for both sub-stages 3-1 and 3-2. At the end of this stage, no crack has been found in the steel members of OSD from the fatigue test of the composite bridge deck. This demonstrates that the UHPFRC overlay can still maintain the strengthening effect in the steel deck plate after the severe conditions of the moving loadings and the environments.

For the strain results in UHPFRC, it is known that the development of cracked region in UHPFRC overlay is mostly dependent on the applied load level of steel wheel. When the wheel load level increases at the beginning of each sub-stage, there are the significant expansion of the cracked region in both the top and bottom layers in UHPFRC overlay. Since the cracking behaviors, i.e., crack pattern, etc., from the experiment at the end of this stage has not been reproduced by the analysis, further investigations of the composite bridge deck are needed to examine the effect of the material properties of UHPFRC material on the cracking behaviors in the reinforcing overlay.

CHAPTER 7 CONCLUSIONS AND FUTURE WORKS

7.1 Major conclusions

This study presents a numerical model developed in a finite element method to predict the fatigue behaviors of an orthotropic steel bridge deck reinforced with UHPFRC overlay under the multi-stages of moving loading and environmental conditions. The bridging stress degradation of cracked UHPFRC and the bond stiffness degradation at the UHPFRC/steel interface were considered as the primary degradation mechanisms in the composite deck under the moving wheel loadings. The fatigue analyses were conducted for the following stages

- Stage 1: under moving loading with rubber tire wheel in dry condition, applied load is equivalent to 100-year design traffic load.

- Stage 2: under moving loading with rubber tire wheel in surface water condition.

- Stage 3: under moving loading with steel wheel in dry condition, applied load is equivalent to 118-year design traffic load.

In static analysis of stage 1, it was found that the maximum value of the deflection and the strain level in the steel deck plate were reduced approximately by 53% and 83%, respectively, after applying UHPFRC layer in the current model. It was also known that the accuracy of the numerical prediction was considerably improved after including the factors such as the actual geometry of the longitudinal ribs, the welding area and the non-uniformly distributions for wheel rubber tire load in the analytical model, especially for the strains of steel deck plate.

In fatigue analysis of stage 1, due to the progressive reduction of the interfacial bond stiffness under tire contact zone and the transverse expansion of the debonded area at UHPFRC/steel interface, the overall stiffness of the composite deck decreased with the increase of loading cycles leading to the continuous deformation increases in both UHPFRC and steel deck plate. The other cause of stiffness decrease was the progressive cracks caused by the bridging stress degradation. It was found in the analysis that the cracked elements were distributed above the longitudinal ribs 3, 4, and 5 from top layer of UHPFRC and under the applied load contact region from bottom layer of the overlay.

In this stage, the current analytical model could provide an acceptable agreement from the strain range results in steel deck plate in comparison with the experimental data.

In stage 2, due to the self-healing of the fine cracks in the UHPFRC overlay, the mechanical recoveries of reloading stiffness and tensile strength from these cracks were obtained leading to the decreases in strain range results in both steel plate and UHPFRC layer. On the other hand, later under the moving wheel loading with rubber tire, the fatigue degradation in the UHPFRC cracks might be accelerated due to the existence of stagnant water. By considering a higher speed of the bridging stress degradation of cracked UHPFRC, it was found that the analytical strain range results of steel deck plate exhibited an acceptable agreement in tendency in comparison to those from the experiment. However, due to the neglect of the residual bond slip at the UHPFRC/steel interface, the unloading strain levels in the steel deck plate may be underestimated in the analysis.

In stage 3, it is found that, with the assumed scenarios with the different expansion speeds of interfacial debonding area for each sub-stage, the current analytical model could give an acceptable agreement in tendencies of the strain range results in the steel deck plate with those from the experiment. At the end of this stage, no crack has been found in the steel members of OSD from the fatigue test of the composite bridge deck. This demonstrates that the UHPFRC overlay can still maintain the strengthening effect in the steel deck plate after the severe conditions of the moving loadings and the environment.

From the analysis, it is found that the effect of interfacial bond stiffness deterioration, which was often neglected from the previous analytical studies of OSD structure, on steel stain results was predominant in comparison to the bridging stress degradation in cracked UHPFRC thanks to the high fatigue durability of UHPFRC. Therefore, the neglect of the interfacial bond stiffness degradation might lead to the unexpected shorten of fatigue lifetime estimated from the design of UHPFRC-steel composite deck, caused by the inaccurate prediction of stress (strain) ranges at the critical locations in the steel members of OSD.

7.2 Recommendations for future studies

Since the effect of bond stiffness degradation on strain results in steel deck plate is predominant in the composite deck in comparison with that of bridging stress degradation in cracked UHPFRC, as mentioned above. Therefore, the fatigue deterioration at the interfacial bond layer may be a significant issue for the future research related to the UHPFRC-steel composite deck. It is recommended that the static and fatigue adhesive joint tests should be carried out beside the standard-specified laboratory tests such as the direct pull-off test, to quantify the interfacial bond stiffness degradation at UHPFRC/steel interface experimentally before conducting the fatigue analysis of the composite deck. The residual bond slip at the UHPFRC/steel interface under fatigue loading, which may be an essential factor to reproduce the experimental unloading strain levels in the steel deck plate, can be also revealed from the above tests.

Because the cracking behaviors in UHPFRC, i.e., crack pattern, etc., from the experiment at the end of stage 3 has not been reproduced by the analysis, further investigations of the composite bridge deck are needed to examine the effect of the material properties of UHPFRC material, i.e., cracking strength, tensile strength, non-uniform properties from top and bottom layers, etc., on the cracking behaviors in the reinforcing overlay.

REFERENCES

[1] Connor RJ, Fisher JW. Identifying effective and in-effective retrofits for distortion fatigue cracking in steel bridges using field instrumentation. J Bridge Eng 2006; 11(6):745-752.

[2] De Jong FBP. Overview fatigue phenomenon in orthotropic bridge decks in the Netherlands. In: Proceedings of the 2004 Orthotropic Bridge Conference, Sacramento, California, 2004, p. 489-512.

[3] Ya S, Yamada K, Ishikawa T. Fatigue evaluation of rib-to-deck welded joints of orthotropic steel bridge deck. J Bridge Eng 2011; 16(4):492–499.

[4] Kodama T, Ichinose Y, Kagata M, Ohta K, Niinobe, Y. Effect of reducing strains by SFRC pavement on orthotropic steel deck of Ohira Viaduct. J Struct Eng, A (JSCE) 2010; 56A:1249-1258.

[5] Liu Y, Zhang Q, Bao Y, Bu Y. Fatigue behavior of orthotropic composite deck integrating steel and engineered cementitious composite. Eng Struct 2020; 220:111017.

[6] Zhang S, Shao X, Cao J, Cui J, Hu J, Deng L. Fatigue performance of a lightweight composite bridge deck with open ribs. J Bridge Eng (ASCE) 2016; 21(7):04016039.

[7] Dieng L, Marchand P, Gomes F, Tessier C, Toutlemonde F. Use of UHPFRC overlay to reduce stresses in orthotropic steel decks. J Const Steel Res 2013; 89:30-41.

[8] Manabe H, Huang CW, Kosaka Y, Mitamura H, Matsumoto T, Imai T. Verification of repair effect of bridge deck using UHPFRC (J-THIFCOM). In: Proceedings of the 12th Japanese German Bridge Symposium, University of Munich, Germany, September 2018.

[9] Makino D, Gouda Y, Mitamura H, Matsui S. Wheel-load-running fatigue test of an UHPFRC-steel composite bridge deck. In: Proceedings of the 10th International Conference on Bridge Maintenance, safety and Management, Sapporo, Japan, April 11-18, 2021. (Virtual conference)

[10] Deng P, Kaminishi H, Gouda Y, Matsumoto T. Influence of insufficient early-age strength of UHPFRC on rehabilitation of OSDs. In: Proceedings of the 10th International

Conference on Bridge Maintenance, safety and Management, Sapporo, Japan, April 11-18, 2021. (Virtual conference)

[11] Makita T, Brühwiler E. Tensile fatigue behaviour of ultra-high performance fibre reinforced concrete (UHPFRC). Mater Struct 2014; 47(3):475-491.

[12] Ma CH, Deng P, Ueda K, Mitamura H, Matsumoto T. Finite element analysis on strengthening effect of the UHPFRC-steel composite deck. In: Proceedings of the 10th International Conference on Bridge Maintenance, safety and Management, Sapporo, Japan, April 11-18, 2021. (Virtual conference)

[13] Safdar M, Matsumoto T, Kakuma K. Flexural behaviour of reinforced concrete beams repaired with ultra-high performance fiber reinforced concrete (UHPFRC). Compos Struct 2016; 157:448-460.

[14] Li VC, Matsumoto T. Fatigue crack growth analysis of fiber reinforced concrete with effect of interfacial bond degradation, Cem Concr Compos 1998; 20(5):339-351.

[15] Matsumoto T, Li VC. Fatigue life analysis of fiber reinforced concrete with a fracture mechanics based model. Cem Concr Compos 1999; 21(4):249-261.

[16] Zhang J, Stang H, Li VC. Fatigue life prediction of fiber reinforced concrete under flexural load. Int J Fatigue 1999; 21(10):1033-1049.

[17] Zhang J, Stang H, Li VC. Experimental study on crack bridging in FRC under uniaxial fatigue tension. J Mater Civ Eng (ASCE) 2000; 12(1):66-73.

[18] Suthiwarapirak P, Matsumoto T, Kanda T. Flexural fatigue failure characteristics of an engineered cementitious composite and polymer cement mortar. J Materials, Concr Struct Pavements (JSCE) 2002; 57(718):121-134.

[19] Suthiwarapirak P, Matsumoto T, Kanda T. Multiple cracking and fiber bridging characteristics of Engineered Cementitious Composites under fatigue flexure. J Mat Civ Eng (ASCE) October 2004; 16(5).

[20] Kakuma K, Matsumoto T, Hayashikawa T, He X. Prediction of fatigue crack initiation of ECC-steel composite deck by wheel trucking analysis. J Struct Eng, A (JSCE) 2011, 57A:1338-1345. (in Japanese)

[21] Suthiwarapirak P, Matsumoto T. Fatigue analysis of RC slabs and repaired RC slabs based on crack bridging degradation concept. J Struct Eng (ASCE), October 1, 2004; 132(6).

[22] Ahmed AD, Matsumoto T. Fatigue analysis of RC slabs reinforced with plain bars based on the bridging stress degradation concept. J Adv Concr Technol 2016; 14:21-34.

[23] Deng P, Matsumoto T. Determination of dominant degradation mechanisms of RC bridge deck slabs under cyclic moving loads. Int J Fatigue 2018; 112:328-340.

[24] Duan L, Brühwiler E, Wang CS. Cold stiffening of orthotropic steel decks by a composite UHPFRC layer. J Constr Steel Res 2020; 172:106209.

[25] Mi H. Finite element analysis on the stress reduction effects of UHPFRC overlaid steel bridge deck developed with a new interfacial bond method. Master thesis, Hokkaido University, Hokkaido, Japan, 2020.

[26] Dai J, Saito Y, Ueda T, Sato Y. Static and fatigue bond characteristics of interfaces between CFRP sheets and frost damage experienced concrete. In: Proceedings of the Fourth International Symposium on Fiber Reinforced Polymer Reinforcement for Reinforced Concrete Structures (FRPRCS-7), Kansas City, Missouri, November 6-9, 2005, p. 1515-1530.

[27] Yun Y, Wu YF, Tang WC. Performance of FRP bonding systems under fatigue loading. Eng Struct 2008; 30:3129-3140.

[28] Loo K, Foster S, Smith T. Fatigue behaviour of CFRP-repaired corroded RC beams. Doctoral thesis, The University of New South Wales, Australia, 2010.

[29] Rots JG, Blaauwendraard J. Crack models for concrete: discrete or smeared? Fixed, multi-directional or rotating?, HERON 1989; 34(1):1-59.

[30] Japan Society of Civil Engineers (JSCE). Recommendations for Design and Construction of High Performance Fiber Reinforced Cement Composites with Multiple Fine Cracks (HPFRCC), Tokyo, Japan, 2008.

[31] J-THIFCOM Construction Association. The material pamphlet of J-THIFCOM (Japan – Thixotropic Hardening Impermeable Fiber Reinforced Composite). Retrieved from https://www.j-thifcom.com/tech.html, 2020.

[32] Matsumoto T, Wangsiripaisl K, Hayashikawa T, He X. Uniaxial tension-compression fatigue behaviour and fiber bridging degradation of strain hardening fiber reinforced cementitious composites. Int J Fatigue 2010; 32(11):1812-1882.

[33] Wille K, Naaman AE. Fracture energy of UHP-FRC under direct tensile loading. In: Proceedings of the 7th International Conference on Fracture Mechanics of Concrete and Concrete Structures (FraMCoS-7), Korea, May 23-28, 2010, ISBN 987-89-5708-180-8, p. 65-72.

[34] Yassin M. Nonlinear analysis of prestressed concrete structures under monotonic and cyclic loading. Doctoral thesis, University of California, Berkeley, CA USA, 1994.

[35] Fairbairn EMR, Toledo Filho RD, Battista RC, Brandao JH, Rosa JI, Formagini S. Experimental and numerical analysis of UHPFRC plates and shells. In: Symposium of Measuring, Monitoring and Modeling Concrete Properties, Proceedings of the 16th European Conference of Fracture (ECF16), Greece, July 3-7, 2006, p. 49-58.

[36] Khan A, Deng P, Matsumoto T. Fatigue tests of UHPFRC beams under four-point bending load. In: Proceedings of the JSCE Conference Hokkaido branch No. 77, Paper report collection No. A-45, Japan, January 30 - February 5, 2021. (Virtual conference)

[37] Jimi H, Deng P, Matsumoto T. Bridging stress degradation model of UHPFRC from numerically fitting fatigue flexural test results using FEA. In: Proceedings of the JSCE Conference Hokkaido branch No. 77, Paper report collection No. A-46, Japan, January 30 - February 5, 2021. (Virtual conference)

[38] Mitamura H, Omote S, Nishi H. Effects of Retrofit with Two CFRP Materials of Different Properties on Fatigue Durability Improvement of RC Slabs. In: CERI Monthly Report, Japan, 2011, p. 2-14.

[39] Wang W, Yan S, Zhao S. Experimental verification and finite element modeling of radial truck tire under static loading. J Reinf Plast Compos 2013; 32(7): 490-498.

[40] De Beer M, Fisher C. Stress-In-Motion (SIM) system for capturing tri-axial tyre-road interaction in the contact patch. Measurement 2013; 46:2155-2173.

[41] Matsui S. Fatigue strength of RC-slabs of highway bridge by wheel running machine and influence of water on fatigue. Proceedings of JCI, 9(2): 627-632, 1987.

[42] Matsui, S. Lifetime prediction of bridge. J Jpn Soc Civ Eng. 30: 432–440, 1996.

[43] Waagaard K. Fatigue strength evaluation of offshore concrete structures. ACI-SP-75: 373-397, 1982.

[44] Solwik V, Saouma EV. Water pressure in propagating concrete cracks. J Struct Eng, 126(2): 235-242, 2000.

[45] Matsushita H. A study on compressive fatigue strength of concrete in the water. J Mat Conc Struct Pave, JSCE, 296: 87-95, 1980.

[46] Maekawa K, Fujiyama C. Crack water interaction and fatigue life assessment of RC bridge decks. Poromechanics V: Proceedings of the Fifth Biot Conference on Poromechanics, ASCE, 2013.

[47] Matsushita H, Tokumitsu Y. A study on compressive fatigue strength of concrete considered survival probability. J Mat Conc Struct Pave, JSCE, 284: 127-138, 1979.

[48] Okuizumi T, Deng P, Matsumoto T. Experimental study about the effects of crack self-healing in UHPFRC on bending behaviors. In: Proceedings of the JSCE Conference Hokkaido branch No. 77, Paper report collection No. A-20, Japan, January 30 - February 5, 2021. (Virtual conference)

[49] Herbert EN, Li VC. Self-healing of Engineered Cementitious Composites in the Natural Environment. G.J. Parra-Montesinos, H.W. Reinhardt, and A.E. Naaman (Eds.): HPFRCC 6, p.155-162. RILEM 2012.

[50] Herbert EN, Li VC. Self-healing of microcracks in Engineered Cementitious Composites (ECC) under a natural environment. Materials, 6: 2831-2845, 2013.

[51] Zhang Z, Zhang Q. Self-healing ability of Engineered Cementitious Composites (ECC) under different exposure environments. Cons Build Mat, 156: 142-151, 2017.

[52] Li M, Li VC. Cracking and healing of Engineered Cementitious Composites under Chloride environment. ACI Mat J. 108(3), 2011.

[53] Kan LL, Shi HS. Investigation of self-healing behavior of Engineered Cementitious Composites (ECC) materials. Cons Build Mat, 29: 348-356, 2012.

[54] Kim S, Yoo DY, Kim MJ, Banthia N. Self-healing capability of ultra-high-performance fiber-reinforced concrete after exposure to cryogenic temperature. Cem Conc Comp, 104, 103335, 2019.

[55] Cuenca E, Serna P. Autogenous self-healing capacity of early-age Ultra-High-Performance Fiber-Reinforced Concrete. Sustainability, 13, 3061, 2021.

[56] Sakai R, Deng P, Matsumoto T. Evaluation of fiber dispersibility of UHPFRC by X-ray CT scan and image analysis. In: Proceedings of the JSCE Conference Hokkaido branch No. 78, Paper report collection No. A-16, Japan, January 29 - 30, 2022. (Virtual conference).